THE DUCTILE FRACTURE OF HSLA STEEL

by

Robert Jay Klassen

A thesis
presented to the University of Manitoba
in partial fulfillment of the
requirements for the degree of
Master of Science
in
Mechanical Engineering

Winnipeg, Manitoba

THE DUCTILE FRACTURE OF HSLA STEEL

BY

ROBERT JAY KLASSEN

A thesis submitted to the Faculty of Graduate Studies of
the University of Manitoba in partial fulfillment of the requirements
of the degree of

MASTER OF SCIENCE

ABSTRACT

The process of ductile fracture in High Strength Low Alloy Structural Steel was studied from a macroscopic as well as a microstructural point of view.

Large scale tensile and fracture toughness tests were performed on six compositional groups of HSLA steel. It was found that the fracture toughness, expressed in terms of J_{Ic} decreased with an increase in the size or volume fraction of inclusions. Also J_{Ic} was found to be related to the grain size, d, by a linear J_{Ic} versus $d^{-\frac{1}{2}}$ relationship.

From a microstructural aspect the fracture process was studied by analyzing the fracture surface topography, using scanning electron microscopy, and by analyzing the effects of plastic deformation using transmission electron microscopy. The role of inclusions as sites for premature void initiation was confirmed by the SEM analysis. The TEM study supported the relationship between fracture toughness and grain size by illustrating that plastic deformation in this ductile material occurs in two distinct stages which seem to be controlled by the influence of grain boundaries on the restraining of dislocation structure development.

This study resulted in a more complete understanding of the ductile fracture process by accounting for variations in the macroscopic fracture toughness in terms of the changes occurring in the material microstructure during plastic deformation at a microscopic level.

ACKNOWLEDGEMENTS

The author would like to thank Dr. M.N. Bassim for the supervision of this thesis topic and for his continuous support and helpful contributions during the course of the research. Also the helpful discussions and assistance of Dr. M.R. Bayoumi and Dr. H.G.F. Wilsdorf are gratefully acknowledged.

The Department of Materials Science, University of Virginia is acknowledged for allowing the author the use of their facilities for some of the research required in this study.

The financial support to the author by the Department of Mechanical Engineering, University of Manitoba as well as a NATO travel grant are also acknowledged.

CONTENTS

LIST OF TABLES

LIST OF FIGURES

Chapter I

INTRODUCTION

Attempts to describe the fracture process in metallic materials have, for the most part, been hindered by the complexity of the phenomena.

The most popular approach is to consider the material as a linear elastic continuum containing a finite crack (or flaw) and evaluate the stress distributions which comply to boundary conditions imposed by the flaw. The results of this linear elastic fracture mechanics approach is the development of a single parameter, K, characterizing the stress intensification caused by the particular flaw geometry in the material, as has been introduced by the Griffith analysis.

However, in most metallic materials the fracture process does not lend itself well to a single parameter description. The fact that most materials absorb significant energy through nonhomogeneous plastic deformation makes it impossible to consider the material as an elastic continuum.

In these materials, which include most commercial low carbon structural steels, the fracture process is referred to as a ductile fracture. The description of the ductile

fracture process is made much more complex by the fact that any factors which create inhomogeneities or regions of anisotropy within the material (such as grain boundaries, second phase precipitates, inclusions, etc.) will affect a materials' fracture toughness by influencing the process of plastic deformation of the matrix.

Macroscopic evaluations of the ductile fracture toughness has been described most successfully in terms of the amount of plasticity (crack tip blunting) occurring at a crack prior to crack growth (COD) or, more recently, in terms of the energy absorbed by plastic deformation prior to crack growth (J_{IC}).

The variations in COD and J_{IC} of particular ductile materials have been evaluated with respect to variations of material properties such as grain size and inclusion densities. However, a more fundamental description of ductile fracture relating the macroscopic toughness (J_{IC}) directly to the primary microstructural event, plastic deformation, has been lacking.

The objective of this thesis is therefore to conduct a two pronged investigation of the ductile fracture process occurring in structural steel. The first approach is to analyze the effects of material properties such as grain size, precipitation density, and inclusion distribution on the macroscopic fracture toughness, J_{IC} , of high strength low

alloy steel (HSLA). The second approach is to study the effect of grain boundaries, precipitates, and inclusions on the plastic deformation process of the material. The ultimate goal of this dual approach is to produce a quantitative description of the fracture process in terms of its most fundamental constituent, the plastic deformation of the material.

This study was conducted by testing the fracture toughness of six compositions of HSLA steel, each containing various grain sizes and inclusion densities. The effects of non metallic inclusions and grain size on J_{IC} are presented in the form of experimental curves. Scanning and transmission electron microscopy was used to analyze the resulting fractured surfaces as well as to study the changes in material microstructure with increased local strain and plastic deformation. In particular, the influence of grain boundaries and large inclusions on this deformation process was studied.

Combination of the results obtained regarding the effects of microstructural material properties on J_{IC} with the information obtained concerning the role of these same material properties on the deformation process results in a description of the large scale ductile fracture toughness in terms of the plastic deformation process occurring in the material.

Chapter II

REVIEW OF THE LITERATURE

The study of the deformation of ductile materials has proceeded in several directions. On one hand, the resistance of a material to ductile fracture has been recorded through macroscopic testing and the variations in these results have been related to variations in material properties through empirical as well as theoretical equations. On the other hand, the specific process of plastic deformation has been studied from a microstructural level using electron-optical techniques. The effects of microstructural features such as grain boundaries, small precipitates and inclusions on the deformation process on numerous types of materials have been investigated in the literature.

This chapter will discuss the recent work that has been done in both these areas of study. Several attempts to reach a more unified understanding of ductile fracture by combining the two areas of research will be reviewed. Firstly however, a review of the development of high strength low alloy (HSLA) structural steel will be given. Of primary interest are the methods (both by alloy additions and thermomechanical processing) used in the manufacture of HSLA steels to produce a structural steel with combined high ductility, toughness, and tensile strength.

2.1 HSLA STEELS

The purpose of developing high strength low alloy steels was the need for a structural steel which exhibited good ductile properties in conjunction with high tensile strength. In that respect HSLA steels are a good example of how steel manufacturing procedures have been developed to improve mechanical properties by directly controlling the materials' microstructure. In HSLA steels the desired microstructure, and corresponding mechanical properties, are obtained by a combination of alloy additions and controlled hot rolling. A brief review of the characteristic chemical composition and resulting mechanical properties of HSLA steels will be given. In particular, the role of alloy additions and thermomechanical treatment on improving material toughness and tensile strength will be discussed.

The largest category of HSLA steels are those containing a ferrite-pearlite microstructure although other HSLA steels may have ferrite-bainite, tempered martensite or bainite structures [1] depending upon specific alloy additions and rolling procedures.

A characteristic feature of HSLA steels is a low carbon content (less than 0.20%). The reason for maintaining a low carbon content is for improved weldability. Also the resulting decrease in pearlite content improves the fracture toughness. Manganese is used instead of carbon for solid

solution strengthening in HSLA steels. A definite advantage of strengthening by Mn additions is an improved fracture toughness [2]. As a result, most HSLA steels have a high Mn:C ratio with a Mn content greater than 1.2 wt.%.

The correlation between grain size and mechanical material properties (tensile and ductile-brittle transition temperatures) proposed by Hall and Petch [3,4] was very significant in the development of HSLA steels. Grain refinement obtained both by alloy additions and controlled rolling is essential for simultaneous improvements in tensile properties and fracture toughness in HSLA steels.

Small alloy additions of niobium, vanadium, and titanium have been used in HSLA steels to improve tensile properties by precipitation strengthening [5,6]. However in the as-rolled condition these precipitation hardened steels had a coarse grain size and low fracture toughness [1]. The problem of coarse grain size was overcome by controlled hot rolling with a low finishing temperature (less than 800°C) [7,8]. The combination of Nb, V, and Ti alloy additions with controlled hot rolling resulted in a very fine austenite grain size which transformed to a refined ferrite grain. The effects of solid solution hardening (from small amounts of C and large amounts of Mn), precipitation hardening combined with grain refinement (from alloy additions and controlled rolling) resulted in HSLA steel achieving tensile strengths in the range of 450-525 MPa. and good ductile

toughness (as indicated by a ductile-brittle transition temperature of -80°C) [1].

The size control of nonmetallic inclusions has been a recent development in HSLA steels and is essential for good formability and through thickness toughness. Alloy additions of zirconium, cerium, calcium, and titanium have been used to transform elongated sulfide inclusions, resulting during hot rolling, into smaller spherical inclusions whose presence does not affect the ductile toughness of the material so drastically. Additions of silicon and aluminum have also been added to HSLA steels as deoxidizing agents. By combining with free oxygen and nitrogen in the material, toughness, ductility, and tensile strengths are improved.

2.2 METHODS OF EVALUATING DUCTILE FRACTURE TOUGHNESS

Because of the complexity of the ductile fracture process, fracture toughness measurements have been mostly comparative rather than definitive. What follows is a brief description of three methods of ductile fracture toughness evaluation that have been frequently used to obtain a numerical parameter which characterizes the resistance of the material to ductile fracture directly from large scale fracture tests.

2.2.1 Notched Bar Impact Testing (Charpy and Izod)

Notched bar impact tests have been standardized for two classes of specimen geometries, namely the Charpy and the Izod tests [9]. Both are simply comparison tests where the energy absorbed during dynamic fracture is recorded. These dynamic tests have been primarily used to determine the ductile-brittle transition temperature for medium strength structural materials. The effects of microstructural changes, introduced by alloying or thermomechanical treatment, on the fracture toughness of a material can be described in terms of how they influence (shift) the ductile-brittle transition temperature. The notched impact tests are used frequently for quality control and material acceptance testing. The difficulty with such impact tests is that no correlation between stress levels applied during fracture and the critical stress levels leading to the initiation of stable crack growth can be obtained. As a result the energy required for crack initiation during quasi-static loading cannot be obtained from the test.

2.2.2 The Crack Opening Displacement (COD)

Cottrell [11] and Wells [12] focused attention on the amount of crack tip opening prior to crack extension as a parameter which might be treated as a characteristic of the crack tip region. Cottrell stated that a given value of COD must be accommodated by a specific size of plastic zone.

The Cottrell-Wells COD concept introduces a parameter which characterizes fracture with or without general yielding (a definite advantage in ductile materials). It is possible then to measure the critical COD (δcrit) for a small test piece which breaks after general yielding and use the same value to predict the failure stress of a large structure which breaks before general yielding. Figure 2.1 shows the variation in COD for various initial crack widths with crack extension in three-point bend test pieces [12]. It is obvious from Figure 2.1 that δmax, which is the parameter usually measured during COD tests, is reached after significant stable crack growth has occurred. It would seem more useful to determine the COD corresponding to crack initiation, δi (Figure 2.1). Since the instant of initial crack propagation would have to be precisely determined during the course of the test in order to establish δi, standardized tests only exist for determining δmax and not δi [13].

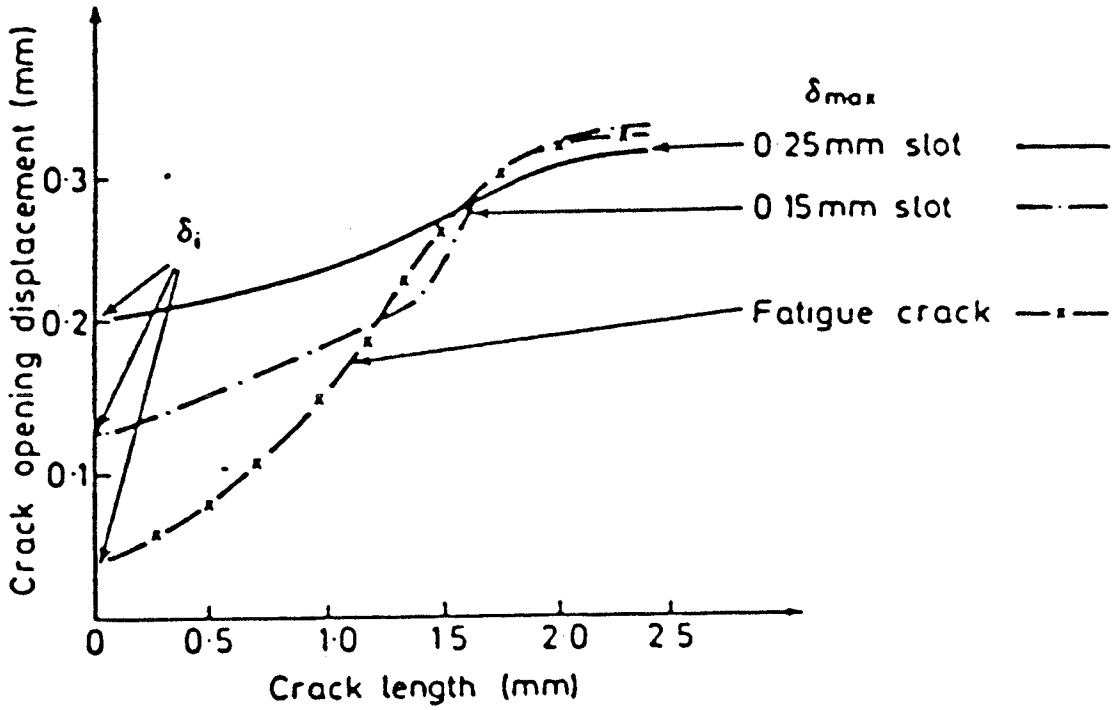

Figure 2.1: Variations in COD With Crack Growth for Several Crack Geometries [12].

2.2.3 The J-Integral

Rice [14] proposed that the crack tip deformation in elastic and elastic-plastic materials could be represented by a path independant mathematical line integral (the J-integral). It was shown by Rice that J is equivalent to the change in potential energy of the crack system when the notch is extended by an incremental amount. Rice proposed that J was equivalent to the energy balance

$$J=-\lim_{\Delta a\to 0}\frac{\Delta U}{B\Delta a} \qquad (2.1)$$

where B is the specimen thickness and ΔU is the change in potential energy of the cracked specimen corresponding to an incremental crack extension, Δa.

Several test methods have been suggested for evaluating J in ductile materials. The early work done by Begley and Landes [15] used a multiple specimen compliance technique where identical specimens with different initial crack lengths were fractured and the J value was calculated at maximum load. From these multiple specimens a J versus Crack Extension curve could be constructed. This test procedure had several disadvantages, notably that the preparation of identical specimens with various crack lengths was very difficult. Also, since the J-integral was calculated

at maximum load, it did not represent the energy absorbed by the material prior to crack initiation (J_{IC}).

The development of the Rice-Paris-Merkle J formula resulted in the following simplified expression for J, applicable to deeply notched bars in pure bending [16]

$$J = \frac{2A}{bB} \qquad (2.2)$$

where b is the remaining uncracked ligament length, and A is the area under the load versus load-line displacement curve. Landes and Begley proposed that the J value corresponding to initial crack extension (J_{IC}) could be found by presenting J values versus instantaneous crack growth on a J-resistance curve [17] as shown in Figure 2.2 . As Figure 2.2 indicates the fracture process begins at a sharp crack (for test purposes a fatigue crack is used). As the load is increased the crack blunts by crack tip deformation. The amount of crack tip blunting increases with increasing load and voids begin to nucleate and grow ahead of the crack. As the voids grow and coalesce, incremental crack extension begins. This sudden crack growth results in the end of the blunting process and the beginning of stable crack growth. At the initiation of stable crack growth the slope of the J-resistance curve changes (Figure 2.2). The blunting process has been represented by a linear blunting line, $J=2\sigma_f A$, where σ_f is

the average of the ultimate tensile and the yield stress. The point at which the test data intersects this blunting line represents J_{IC} [18], the energy absorbed by the material at the crack tip prior to the initiation of stable crack growth.

When conducting J integral tests it is required to know the amount of crack advance as the test proceeds. This can be done by multiple specimen testing, i.e. breaking identical specimens at different points of the test and measuring physical crack lengths. Single specimen techniques are also used to determine the J integral where crack extension is recorded by a partial unloading compliance technique. The slope of the unloading Load versus COD line gives an indication of the instantaneous crack length [18,19].

By definition , J_{IC} corresponds to the end of blunting (stretch zone growth) and the beginning of crack propagation. A standardized testing procedure to obtain J_{IC} values using stretch zone width instead of, or in conjunction with, physical crack length measurements has been adopted by the Japanese Society for Mechanical Engineers (JSME) [20].

The critical stretch zone width can be measured directly with scanning electron microscopy (SEM) of the fracture surface. Nguyen-Duy and Bayard have proposed an equation relating the critical stretch zone width to the crack opening displacement, as shown in Figure 2.3 [21].

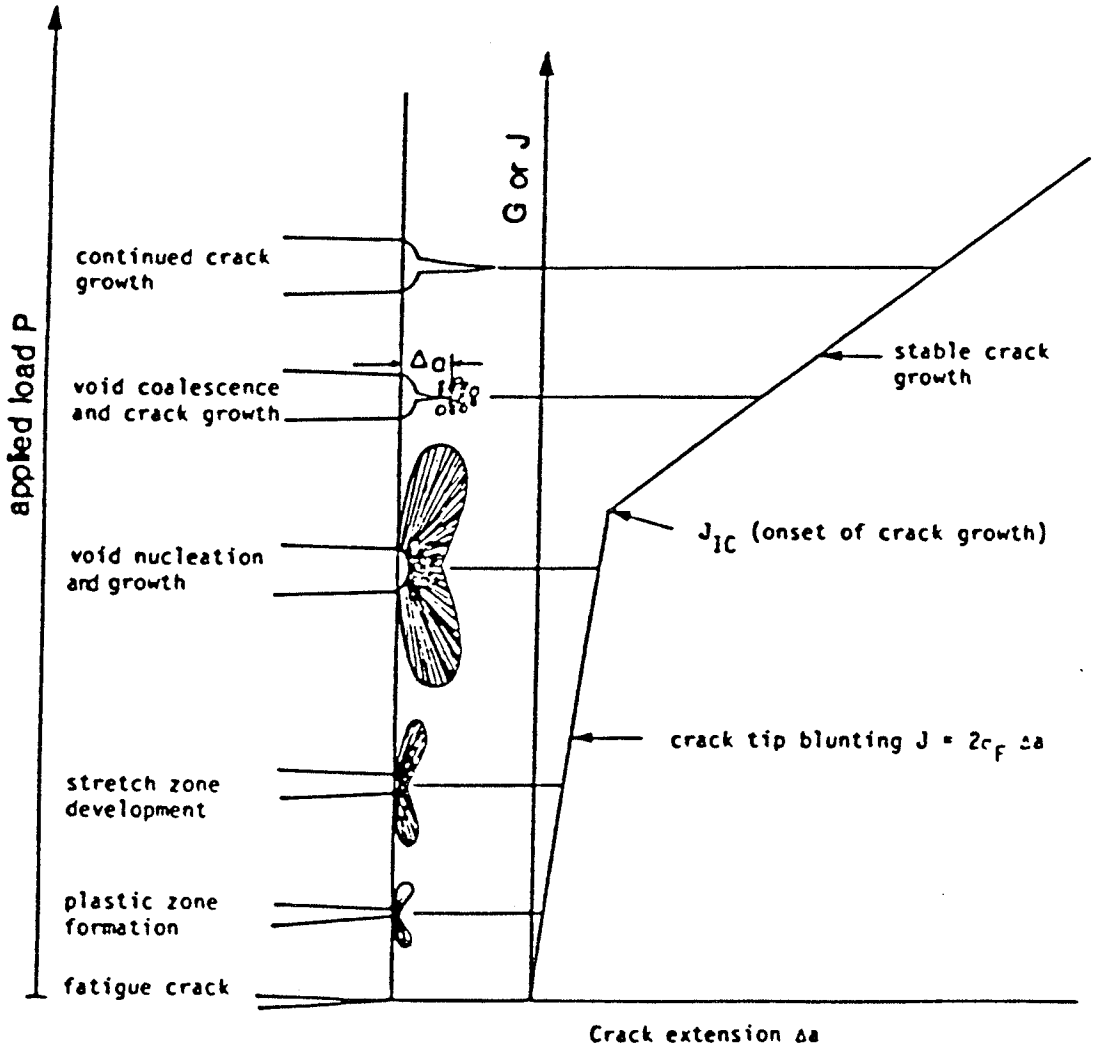

Figure 2.2: J Versus Δ A Resistance Curve [74].

$$(COD)_c = \frac{2d'}{\cos\lambda+\sin\lambda} \times \frac{1}{G} \qquad (2.3)$$

Where d' is the measured plane strain stretch zone width, λ is the incident beam angle, and G is the magnification. Under plane strain conditions, the J_{Ic} can be related to the critical crack tip opening displacement (COD)c by the following equation [22,23]

$$J_{1C} = m\sigma_f(COD)_c \qquad (2.4)$$

where m is a constraint factor due to plane strain loading (approx. = 2) and σ_f is the average between the yield and ultimate tensile stress. The result of equations 2.3 and 2.4 is that in ductile materials displaying recognizable stretch zones, J_{Ic} values can be directly calculated from SEM fractographs using the following expression.

$$J_{1C} = \frac{4\sigma_f d'}{\cos\lambda+\sin\lambda} \times \frac{1}{G} \qquad (2.5)$$

Amouzouvi and Bassim [24], and Bayoumi and Bassim [25] have calculated J_{Ic} values directly from the stretch zone width of fractured specimens using equation 2.5. The results of this single specimen method agree well with values obtained from the standardized J-resistance curve test method.

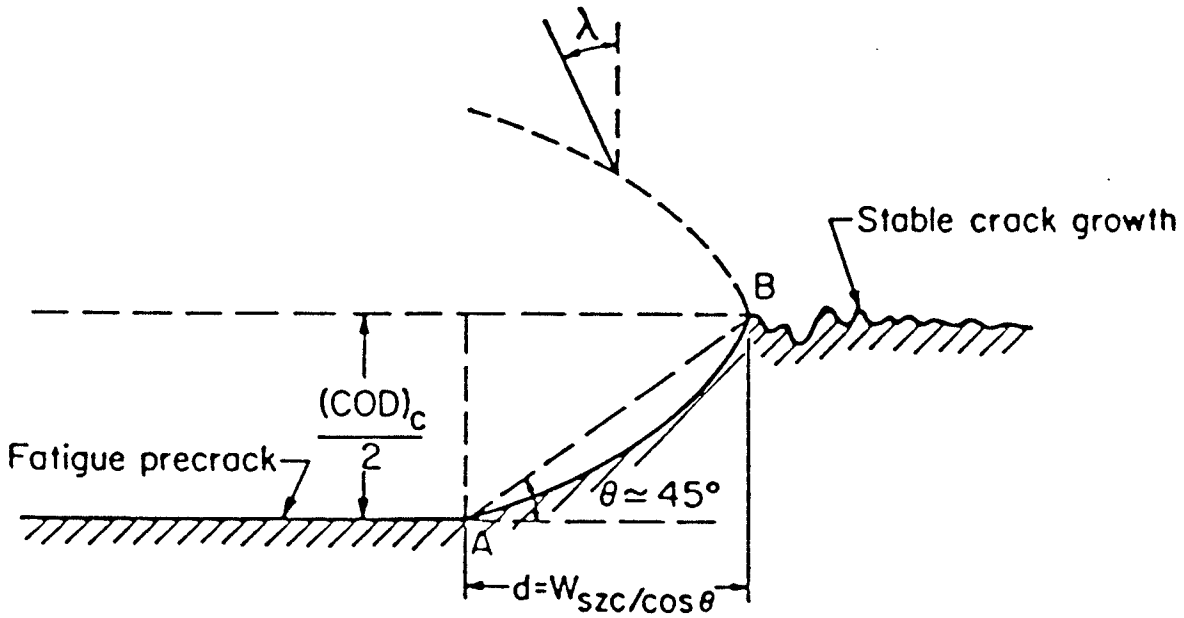

Figure 2.3: Illustration of the Stretch Zone on a Precracked Fracture Surface [21].

2.3 RELATIONSHIPS BETWEEN MICROSTRUCTURE AND DUCTILE FRACTURE

Considerable work has been done to explain the effects of material microstructures on ductile fracture toughness. The results of several studies evaluating the contributions of microstructural properties, such as grain size and second phase precipitates , to the macroscopic fracture parameters will be reviewed.

2.3.1 Effect of Grain Size

The beneficial contributions of grain refinement to the fracture toughness of ferritic steel has been reported in the literature [4]. This relationship is illustrated by the effect of grain size on the notched impact ductile brittle transition temperature, where decreasing the grain diameter from ASTM grain size 5 to ASTM grain size 10 can lower the 10 ft-lb Charpy V-notch transition temperature by about 130 F in ferritic mild steel [26]. The following Petch equation expresses variations in the ductile brittle transition temperature, T , (obtained from notched impact tests) with grain size, d, as :

$$\beta T_c = \ln\beta - \ln C - \ln d^{-1/2} \qquad (2.6)$$

where β and C are material constants.

Grain boundaries have also been considered to influence ductile fracture properties by acting as possible sites for void nucleation, especially at high temperatures where grain boundary sliding is observed [27,28]. A correlation between voids and grain boundary triple points in pure HCP titanium was found experimentally by Erickson [29]. Erickson found a direct correspondance between void spacing and grain boundary triple point spacing [29] over a limited range of grain sizes. It was suggested that large incompatibilities between available slip systems in adjacent grains could cause void initiation at grain boundary triple points as discussed by Chang and Grant [30]. Void nucleation at grain boundary triple points has not been substantiated experimentally for BCC materials, such as ferritic steel, probably because of the many more available slip systems in a BCC lattice which makes the effects of grain boundary misorientation less severe.

2.3.2 Effect of Second Phase Particles

2.3.2.1 Nonmetallic Inclusions

Considerable investigation has been done to evaluate the effect of these inclusions, mainly sulfides, on the ductile fracture toughness of steels. The effect of inclusion size and orientation (either elongated or globular) has been analyzed in terms of changes in the Charpy V Notch (CVN) upper shelf energy [31,32]. In general, the effect of nonmetallic

inclusions in low carbon steel is to decrease the amount of energy absorbed during fibrous fracture (CVN upper shelf energy) and, therefore, lower the fracture toughness. Spitzig [32] correlated the effect of sulfide density as well as orientation on fracture toughness by relating the CVN shelf energy to a single parameter P. P is defined as the total projected length of inclusion per unit area on a plane parallel to the fracture plane. It was found that CVN shelf energy decreased with an increase in the parameter P [32]. Similar findings are recorded by Willoughby et al on the effect of inclusion orientation on the critical COD of precracked bend specimens [33].

On a more theoretical level, the detrimental influence of inclusions on toughness has been attributed to the inclusions acting as sites for preferential void nucleation. Continuum mechanics models of the local stress distributions around inclusions and the critical stress and/or strain state resulting in void nucleation at the inclusions has been discussed extensively in the literature [34-37]. However, most of these theories consider void nucleation from a solid mechanics approach and, with the exception of the Goods and Brown model [36], do not account for the inhomogeneous plastic deformation occurring around the inclusions. The result is that correlations between macroscopic ductile fracture toughness parameters with inclusion spacing and orientation using a continuum mechanics approach have, as of

yet, been considered too complex to be modelled successfully. A detailed review of the major theories of void nucleation as well as the ductile fracture process in general, from a microstructural perspective, is presented by Wilsdorf [38].

Experimental expressions of macroscopic crack opening displacements as a function of interparticle spacings have been discussed by Knott [39] and Rice [40]. Both showed that the fibrous fracture resulted from a mechanism which involves the internal necking of the matrix material between nonmetallic inclusions. In particular, Rice and Johnson presented an expression representing the critical amount of COD (δ_i) in a precracked specimen in terms of mean interparticle spacing (χ_0) [40]. Rice suggested that for most structural metals :

$$\delta_i = 1 \text{ to } 2.7\ \chi_0 \qquad (2.7)$$

Equation 2.7 indicates that for a complete understanding of ductile fracture toughness, in terms of changes in the material microstructure, the role of inclusions will have to be studied not only in terms of their direct effect on macroscopic toughness parameters but also on their influence on the process of local matrix deformation. Equation 2.7 represents part of that correlation however the complex mecha-

nism occurring during the nonhomogeneous plastic material deformation must also be accounted for.

2.3.2.2 Small Precipitates

The effect of small precipitates on ductile fracture toughness is, in some ways, a more complex problem than that of large inclusions. These small precipitates often hinder high temperature grain growth or provide significant precipitation strengthening. Blind and Martin [41], as well as Bassim et al. [42] have reported increases in ductile fracture toughness (J_{IC}) with increases in precipitate content for Al-Mg-Si alloys and low alloy steels containing Nb additions respectively. Although the reasons for this increased fracture toughness has not been completely explained for these cases, it is apparent, for the particular case of HSLA steels, that the presence of niobium, titanium, and to a lesser extent vanadium carbides and nitrides results in significant grain refinement as well as precipitation strengthening [43-46]. The beneficial influence of grain refinement on fracture toughness, as discussed in section 2.3.1, combined with the fact that small precipitates have stronger particle-matrix interfaces than do large inclusions could explain the improved fracture toughness.

2.4 PLASTIC DEFORMATION PRIOR TO FRACTURE

The results of experimental studies of the plastic deformation process in single and polycrystalline material will be reviewed in this section. Section 2.4.3 will discuss several proposed theories which relate the macroscopic process of crack tip blunting, a characteristic feature of ductile fracture, to the process of plastic deformation by dislocation movement. The contention in this section is that a materials' ability to deform plastically prior to fracture will be the true indication of its ductile fracture toughness.

2.4.1 Single Crystals

Transmission electron microscopy of thinned single crystals has indicated that plastic deformation of a material free of precipitates or grain boundaries is still a nonhomogeneous process. Plastic deformation has been observed to occur by the accumulation of dislocations into dislocation structures or cells [47]. Dislocation cells have been observed extensively in FCC metals such as aluminum [48] and copper [49]. In body centered cubic materials, dislocation cells have been observed in deformed iron by Keh and Weissman and by Carrington et al [50,51]. Dislocation cells are not characteristic only of tensile deformation but have been observed resulting during cyclic fatigue [52] and creep [53] as well. A review of the dislocation structures present in

metallic crystals during work hardening has been given by Nabarro, Basinski, and Holt [54]. These dislocation structures have a very high dislocation density in the cell walls which surround the inner region containing a much lower dislocation density.

The stresses and energy of dislocation cells has been investigated extensively by Bassim [55] using numerical techniques. The results of the investigation was that a repeatable cell pattern, the 'checkerboard' pattern, with alternating senses of rotation between cells was the most effective in reducing long range stresses and could therefore be expected to occur during deformation [56].

The accumulation of dislocations into uniform dislocation cells represents the lowest energy configuration for the dislocations. Therefore a nonhomogeneous distribution of dislocations during straining could theoretically be expected.

Kuhlmann-Wilsdorf accounted for the three distinct stages (I , II, and III) of work hardening in deformed crystals in a 'unified theory' of work hardening [57]. In this theory the branching and inter connecting of dislocation cells results in smaller dislocation cell diameters and is the reason attributed to the increasing hardness during stages I and II of work hardening. The parabolic shape of the stress-strain curve during stage III is attributed to the

dislocation cells reaching a minimum size and no longer decreasing with applied strain.

The fact that dislocation cells are found in many different materials (metallic and nonmetallic) and in various straining modes indicates the important role that the process of dislocation accumulation into low energy structures has on plastic deformation. Very little work, however, has been done relating to the role of these structures in ductile fracture. One notable exception is the work by Gardner et al [58] who observed crack initiation at dislocation cell walls during in-situ straining of high purity single crystals of iron using high voltage electron microscopy.

2.4.2 Polycrystals

The plastic deformation process in polycrystalline materials has been studied experimentally (most notably with TEM) and discussed theoretically.

In terms of experimental observations, plastic deformation was observed to occur by the development of dislocation cell structures in a method similar to that discussed in section 2.3.1. Specifically, Langford and Cohen have observed the development of dislocation networks in drawn iron wire [59]. The micrographs resulting from that investigation were analyzed qualitatively by Kuhlmann-Wilsdorf [60] and were found to conform to the model of the 'unified theo-

ry of work hardening' [57]. Griffiths and Riley [61] studied the dislocation arrangements in deformed polycrystalline 3 percent silicon-iron and also found that dislocations arranged into cells which decreased in diameter when strain increased.

The role of grain boundaries is one of restraining plastic deformation. In general because of the misorientation of the grains, plastic deformation cannot spread easily from one grain to the next. This concept was used by Petch [4] to relate the dependance of yield stress on grain size. Petch described the yield stress of a polycrystalline material as being composed of two components the yield stress of a constrained single crystal, σ_i , and the strengthening effects of the grain boundaries. The strength of a grain boundary can be described in terms of the number of dislocations which pile up against it as shown in Figure 2.4 . The concentrated shear stress, τ_L , at some point (r, Θ) from the grain boundary due to the dislocation pile up can be expressed as

$$\tau_L = (\tau - \tau_i)\left(\frac{L}{r}\right)^{1/2} F(\theta) \qquad (2.8)$$

where τ is the applied shear stress and L is the dislocation slip band length (Figure 2.4). Since by definition the yield stress, τ_y , is the applied stress required to produce

slip across the macroscopic gage length (i.e. dislocation movement across the grain boundaries) it can be assumed that yielding will occur when the concentrated shear stress, τ_L, reaches a critical stress, τ^*, at some distance, r^*, from the grain boundary such that a dislocation source, S, is formed in the new grain. Therefore equation 2.8 becomes:

$$\tau^* = (\tau_y - \tau_i)\left(\frac{L}{r}\right)^{1/2} F(\theta) \qquad (2.9)$$

or in terms of the yield shear stress:

$$\tau_y = \tau_i + \tau^* (r^*)^{1/2} L^{-1/2} \qquad (2.10)$$

where $\tau^*(r^*)^{1/2}$ is a material constant, K'_y, characteristic of the particular grain boundary strength. Since the dislocation slip line length, L, is approximately one-half the grain size, 2d

$$\tau_y = \tau_i + K'_y d^{-1/2} \qquad (2.11a)$$

or in terms of the tensile yield stress

$$\sigma_y = \sigma_i + K_y d^{-1/2} \qquad (2.11b)$$

where $K_y = 2K'_y = 2\tau^*(r)^{1/2}$. Equation 2.11 is known as the Petch equation [62] and is a quantitative illustration of the effect that grain boundaries have on the plastic deformation of a material.

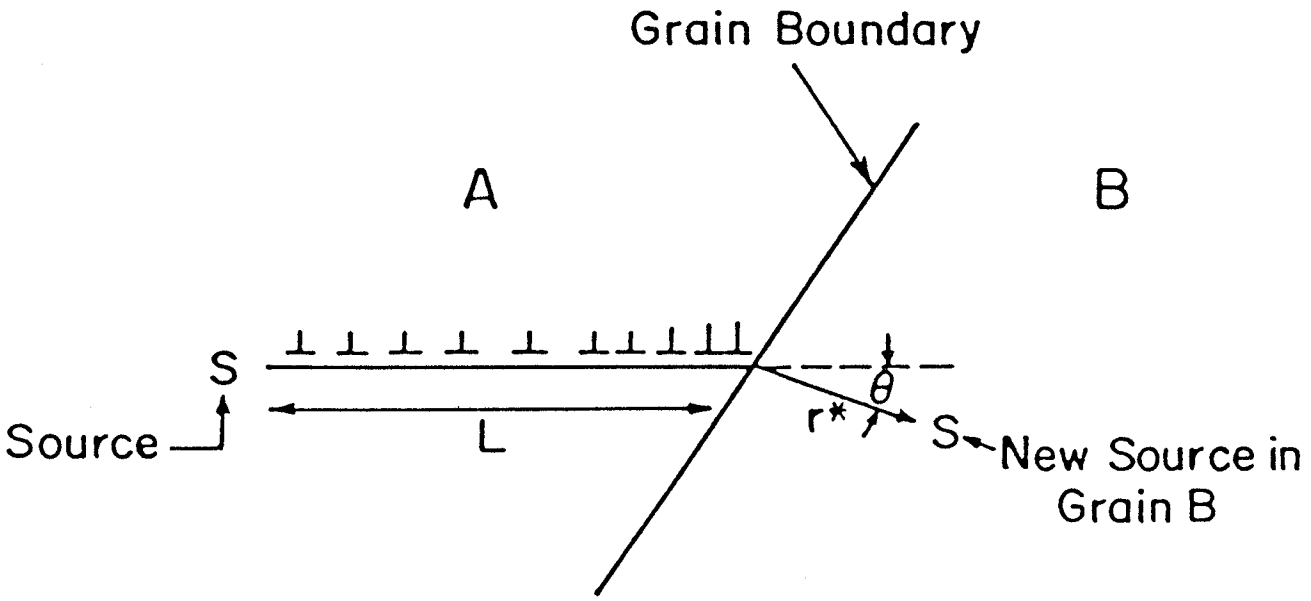

Figure 2.4: The Effect of Grain Boundaries on the Deformation of Polycrystals

2.4.3 Plastic Deformation During Crack Tip Blunting

Crack tip blunting is a process synonymous with ductile fracture. The amount of energy that a material is able to absorb through plastic deformation is characterized by the amount of crack tip blunting that occurs prior to crack growth. This is the basis for the correlation between the macroscopic fracture toughness parameter, J_{IC}, with the critical crack opening displacement, (COD)c, given in equation 2.4 and discussed in section 2.2.3. As a result, theories describing the process of plastic deformation at a crack tip prior to fracture have the potential for relating macroscopic fracture toughness to the process of plastic deformation.

Friedel [63], Tetelman [64], and Tetelman and McEvily [65] have analyzed crack tip blunting in its most theoretical form as occurring by the emission of dislocations from the crack tip. This widens the crack tip by an atomistic step equivalent to the Burgers vector for each dislocation emitted. Rice and Thomson [66] proposed a similar theory on crack tip blunting where blunting occurred by the emission of dislocations from the crack tip along slip lines. Weertman [67] proposed a model of crack tip blunting where dislocation pairs are created on slip planes in the material and dislocations of one sign are attracted to the crack tip and while dislocations of the opposite sign are repelled. Blunting will occur when the energy of the resulting dislo-

cation pile up exceeds the energy required to create a new crack surface.

The presence of mobile dislocations, or active dislocation sources, within the material will greatly increase the amount of energy absorbed during plastic deformation compared to the emission of dislocations from the crack tip. Because of this observation Tetelman[64] and Tetelman and McEvily [65] concluded that the density of mobile dislocation sources is the most important parameter which determines the ductility of the material.

An early theory of crack tip blunting suggested by Friedel [63] described blunting in terms of the movement of edge dislocations, whose Burgers vectors were perpendicular to the fracture plane, toward the crack tip. This produces plastic relaxation of the stresses near the crack tip and results in crack tip blunting.

Amouzouvi and Bassim [68] presented a model of crack tip blunting in polycrystalline material subject to plane strain where blunting occurred by the movement of a high density of mobile dislocations along slip lines toward the crack tip. This model was able to explain the increase in fracture toughness with 2% prior straining in steel in terms of the resulting increase in mobile dislocation density.

The work of Amouzouvi and Bassim [68] represents the first attempt at a correlation between macroscopic fracture

toughness, J_{IC} , and the microscopic deformation process, expressed in terms of the mobile dislocation density. The model in Reference [68] of course oversimplifies the process of plastic deformation at a crack tip in a polycrystalline material to some extent. The observation that dislocations arrange preferentially in low energy dislocation cell structures at relatively low local strains, as discussed in sections 2.4.1 and 2.4.2, would indicate that crack tip blunting is more complex a phenomena in reality than the movement of individual dislocations along defined slip planes towards, or away from, a crack tip. Experimental evidence would suggest that the stages of development of these dislocation cell structures, including their interactions with grain boundaries and particles, during straining should be evaluated to yield a better understanding of ductile fracture in dual phase, polycrystalline material.

Chapter III

EXPERIMENTAL PROCEDURES

3.1 MATERIALS

Six compositions of HSLA steel were used in this study.[1] The precise chemical compositions were supplied by the producer and are indicated in Table 3.1 . The compositions of the six metal groups are virtually the same except that metal groups 2-6 contain various amounts of V, Ti, and Nb microalloy additions either alone or in combination with each other. Metal 1 contained no V, Ti, or Nb additions and was used as a base metal reference.

All the metal groups received the same hot rolling treatment. Seventy five kilogram ingots of each metal group were held at 1220°C for two hours then reduced from 127 mm to 11.4 mm thickness by 15 successive straight hot rolling passes. The final rolling pass was completed at 800°C after which the steel was air cooled to room temperature. The final transverse width of the steel plate was 16.0 cm.

---

[1] These steels were produced according to specifications by the Physical Metallurgy Research Laboratories of CANMET in Ottawa.

The characteristic microstructure and inclusion distribution of this steel with respect to the rolling direction are illustrated by the etched and unetched micrographs shown in Figure 3.1 and 3.2 respectively.

TABLE 3.1

Steel Composition,†† wt. %

Steel	C	Si	Mn	P	S	Al	Nb	V	Ti
1	.12	.21	1.27	.01	.01	.02	-	-	-
2	.13	.15	1.15	.01	.01	.04	-	.09	-
3	.12	.21	1.12	.01	.01	.02	-	-	.08
4	.11	.21	1.30	.01	.01	.05	-	.07	.07
5	.10	.24	1.17	.01	.01	.04	.04	.04	.05
6	.12	.14	1.15	.01	.01	.02	.10	-	-

††The Nitrogen and Oxygen content in all steel groups is less than 0.006% and 100 ppm respectively.

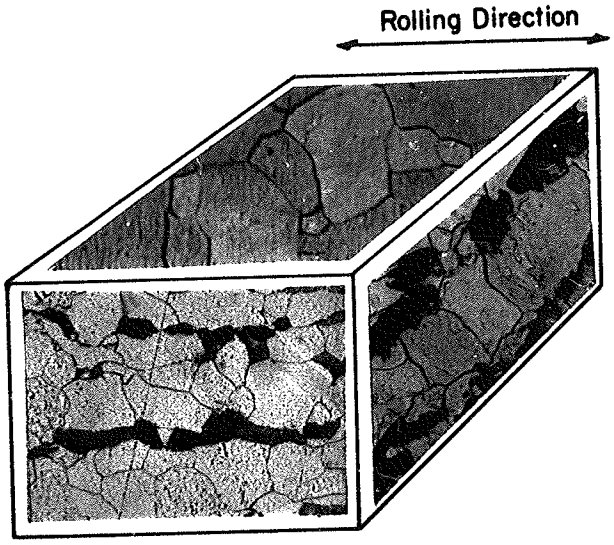

Figure 3.1: Microstructure of the HSLA Steel in Longitudinal, Transverse and Through-thickness Directions With Respect to the Rolling Direction

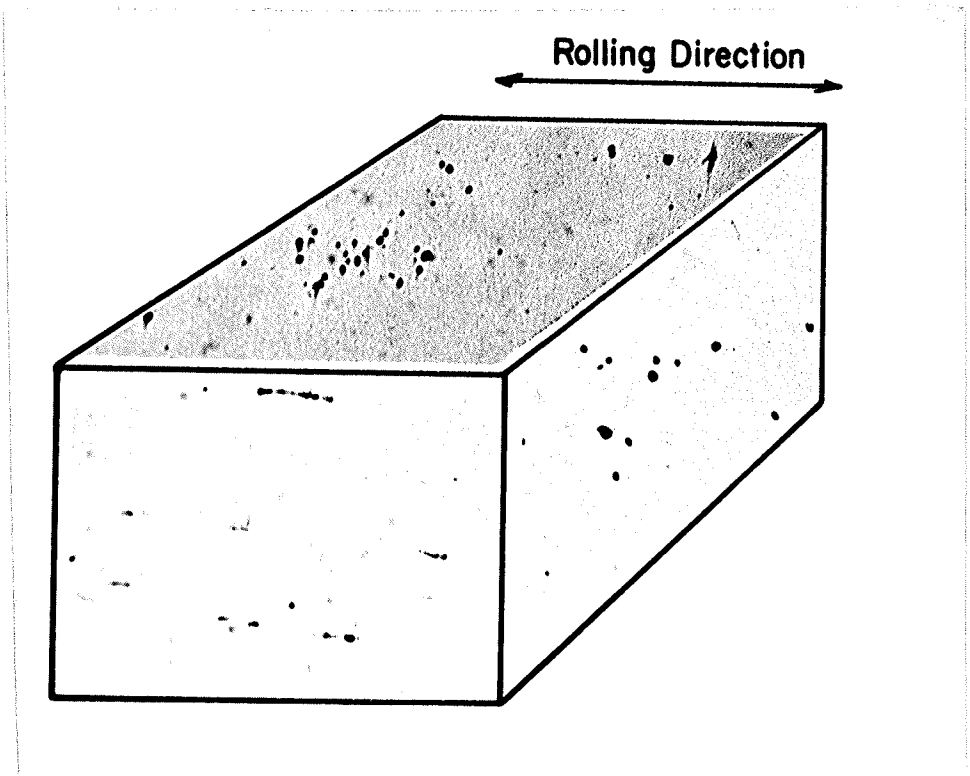

Figure 3.2: Inclusion Distribution of the HSLA Steel in Longitudinal, Transverse, and Through-thickness Directions With Respect to the Rolling Direction

3.2 SPECIMENS PREPARATION

Four types of specimens were prepared for evaluation in this study. Tensile and precracked three point bending specimens were constructed for mechanical testing. Thin foil specimens as well as mounted fracture surfaces were prepared for transmission and scanning electron microscopy.

3.2.1 Tensile Specimens

Tensile specimens were prepared from each of the metal groups. The specimens were prepared from the as received plate such that the gage lengths were in the transverse direction with respect to the rolling direction (Figure 3.3). These round tensile specimens were machined to the dimensions and tolerances required by the ASTM standard E8-82 [69]. These dimensions are illustrated in Figure 3.4

3.2.2 Precracked Fracture Specimens

Notched three point bend specimens were prepared from each of the six metal groups for fracture toughness testing. These specimens were cut from the steel plates in the longitudinal-transverse (L-T) orientation with respect to the rolling direction as shown in Figure 3.3 . The specimen dimensions were in accordance with the ASTM standard for J_{IC} determination (ASTM E813-81) [18]. These dimensions are illustrated in Figure 3.5.The specimens were fatigue pre-

cracked using an Instron servo-hydraulic testing unit according to ASTM E813-81 procedure. The fatigue precracking as well as the actual fracture tests were performed at room temperature.

3.2.3 SEM Specimens

The fracture surface regions were cut from the tensile and three point bending specimens, after mechanical testing, in order to conduct the SEM analysis. In the case of the fractured tensile specimens, the fracture surface was cut 1 mm from the surface with a BEUHLER Isomet slow speed diamond saw. These fracture surfaces were then attached to an aluminum holder with silver conducting paint. For the fractured three point bend specimens, the fracture surface was cut with a high speed abrasive cut off saw. The fracture surface, including the fatigue precrack surface and the stretch zone region, was then attached to an aluminum holder with silver conducting paint.

Samples of the bulk material of the six metal groups were mounted in bakelite and polished. These unetched polished samples were used for x-ray analysis in the scanning electron microscope.

3.2.4 TEM Specimens

Thin foils were prepared for transmission electron microscopy from strained as well as unstrained material in each of the six metal groups. The unstrained foils were cut with a slow speed diamond saw from the as received steel plate. The strained foils were cut from the strained gage length region of fractured tensile specimens (section 3.3.1) by using a slow speed diamond saw The local cross sectional diameter, $\emptyset_i$, as well as distance, X_i, from the fracture surface were recorded for each strained foil. One strained foil was cut from the strained tensile specimens from each of the six metal groups.

$\emptyset_i$, X_i , and the corresponding local percentage reduction in area are shown in Table 3.2 Five additional foils were cut from a fractured tensile specimen gage length of metal 6 to study the deformation occurring with increased local strain in more detail. The $\emptyset_i$, X_i and local reductions in area for these five foils are shown in Table 3.3

Each TEM foil was approximately 0.30 to 0.38 mm in thickness after being cut on the diamond saw. The foils were mechanically polished to a thickness of 0.13 mm. Following mechanical polishing, disks of 3 mm in diameter were stamped out of the foils. These disks were further thinned and polished electrolytically using a STREURS electro-jet polishing unit. The electrolyte used was 10% perchloric acid in meth-

anol. During polishing the electrolyte was maintained at -50°C, an applied voltage of 14.0 V was used which resulted in a cell current of 80 mA. A photo sensitive diode was used to detect when a hole had been created in the foils. After thinning the foils were placed directly into the electron microscope column to avoid unnecessary contamination in the atmosphere.

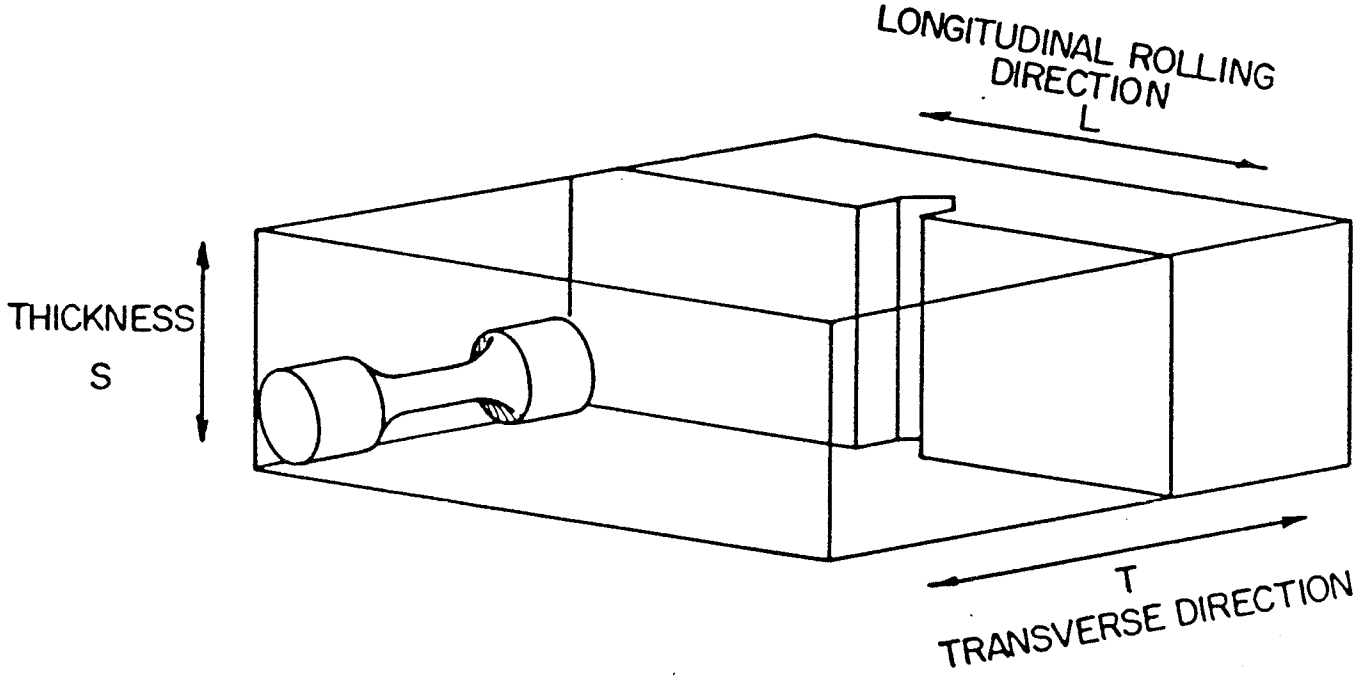

Figure 3.3: Location of Tensile and Three Point Bend Specimens With Respect to the Rolling Direction

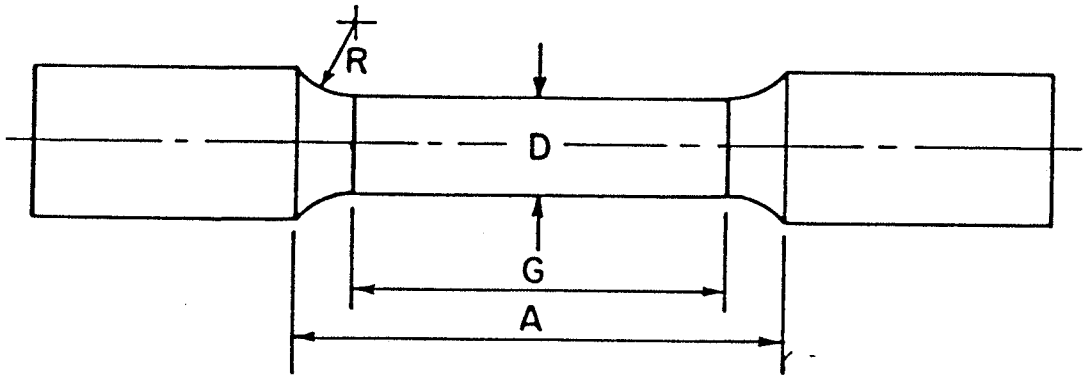

G = 25.0 ±0.10 mm
D = 6.25 ±0.12 mm
R = 5 mm
A = 32 mm

Figure 3.4: Tensile Specimen Dimensions

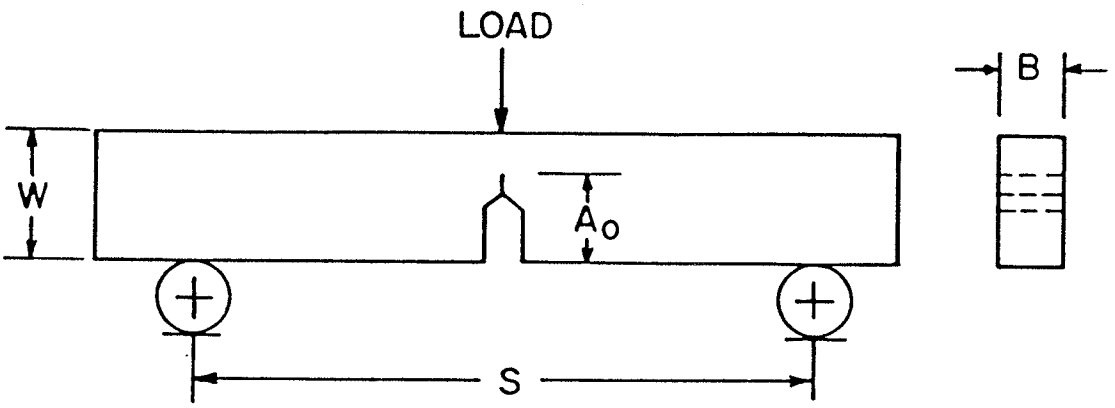

W = 17.1 mm
A_o = 9.69 mm - 10.927 mm
B = 8.50 mm
S = 83.6 mm

Figure 3.5: Three Point Bend Specimen Dimensions

TABLE 3.2

Location and Local Strain of TEM Foils
Cut from the HSLA Steel

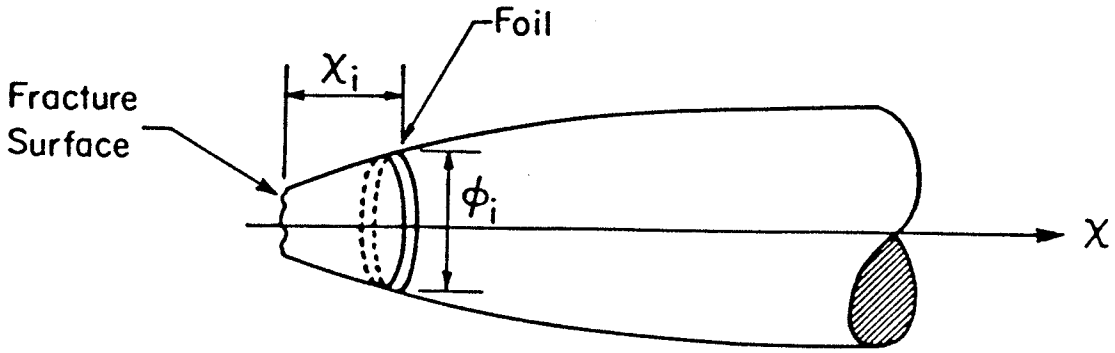

Metal Group	Distance from Fracture Surface X_i (mm)	Local Diameter ϕ_i (mm)	Local Reduction in Area (%)
1	2.9	4.9	39.0
2	3.0	5.2	31.8
3	2.9	5.0	35.0
4	2.8	4.8	42.0
5	2.6	4.6	47.0
6	2.8	5.0	37.0

TABLE 3.3

Location and Local Strain of TEM Foils
Cut from Metal 6

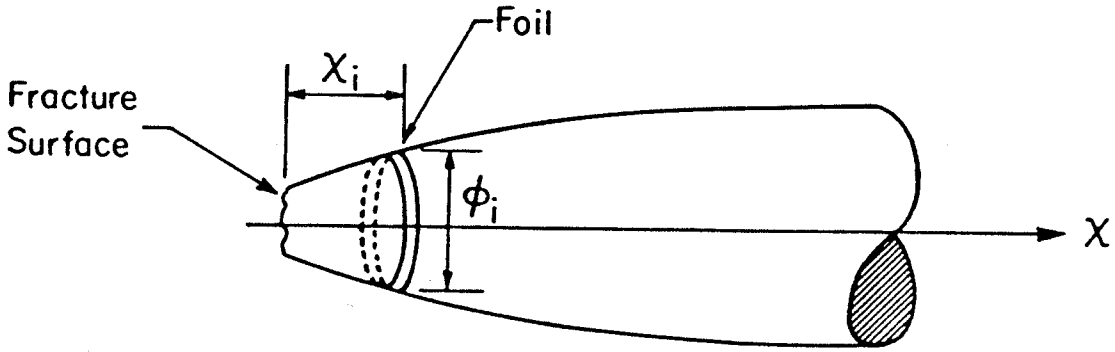

Foil Number	Distance from Fracture Surface X_i (mm)	Local Diameter ϕ_i (mm)	Local Reduction in Area (%)
1	2.58	4.1	48.3
2	3.68	4.9	26.1
3	4.01	5.2	16.7
4	4.46	5.3	13.5
5	4.82	5.4	10.2

3.3 MECHANICAL TESTING

3.3.1 Tensile Testing

The tensile tests were performed on an INSTRON screw type testing machine according to ASTM E8-82 specifications [69]. All the tensile testing was conducted at room temperature using a cross head speed of 0.25mm/min. The values of ultimate tensile strength, yield strength, fracture strain, and the strain hardening exponent were obtained for all the metal groups from the resulting stress-strain curves. The values of percent elongation and reduction in area at fracture were obtained by measuring the gage lengths and cross sectional areas of the specimens before and after testing. After tensile testing, TEM foils were prepared from the strained gage length regions of the tensile specimens as described in section 3.2.4.

3.3.2 Fracture Toughness testing

A single specimen technique was used to calculate the fracture toughness, J_{IC}. The precracked specimens were loaded at a quasi-static loading rate (0.25 mm/min) on an INSTRON screw type testing machine until noticable stable crack growth occurred and maximum load had been reached on a load-stroke plot. The specimens were then broken in half and the fracture halves were observed with SEM. The average plane strain stretch zone width (SZW) was measured from the SEM fractographs. Figure 3.6 shows the physical crack tip

region referred to as the stretch zone. Values of J_{IC} were calculated directly using equation 2.5.

$$J_{1C} = \frac{4\sigma_f d'}{\cos\lambda + \sin\lambda} \times \frac{1}{G} \qquad (2.5)$$

In these micrographs the incident beam tilt angle, λ, was 30° and the magnification, G, was between 100-250x. This method of determining J_{IC} from the average stretch zone widths produced consistent values of J_{IC} between specimens within the same metal groups. J_{IC} values were also calculated for two specimens in each metal group using the single specimen J_{IC} resistance curve technique with partial unloading compliance measurements to determine the incremental crack growth [70]. These values showed considerable scatter which was attributed to inaccuracy in the compliance determination. As a result, even though these J_{IC} values showed the same trends from one metal group to another as did the J_{IC} values calculated from critical stretch zone widths, the latter values were considered more reliable and are presented for discussion in this study.

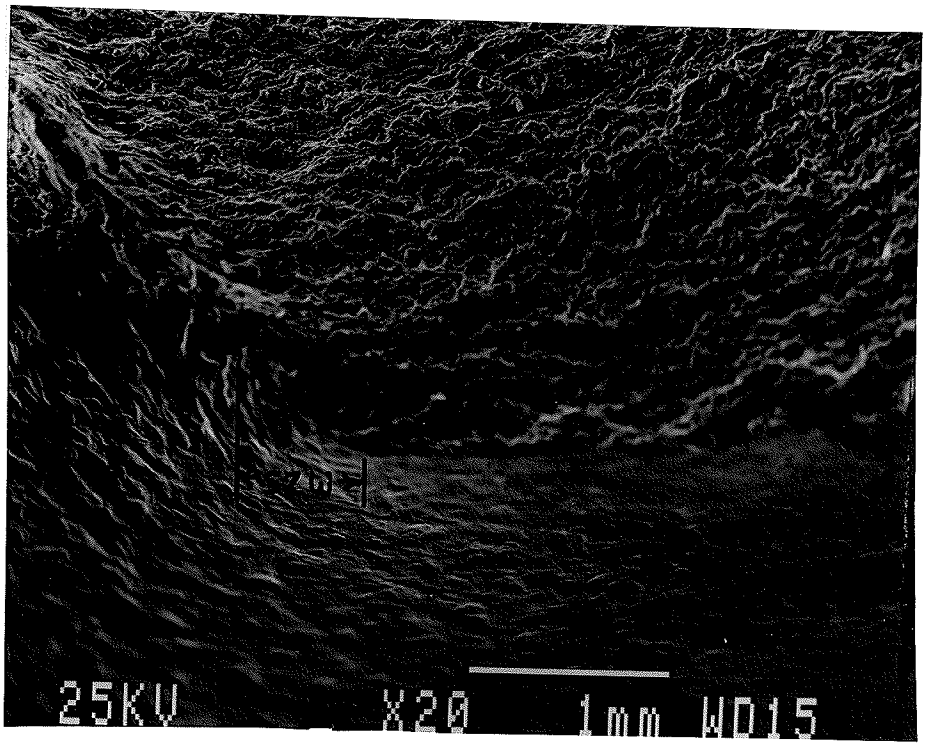

Figure 3.6: Fracture Surface of a three Point Bend Specimen Illustrating the Stretch Zone Region

3.4 MICROSTRUCTURAL ANALYSIS

3.4.1 Optical Microscopy

Optical microscopy was performed on samples of all the metal groups to characterize the individual microstructures. Specifically the size and distribution of inclusions as well as the grain size were analyzed.

A LEITZ automated image analysis system was used to obtain a statistically accurate description of the inclusion size and distribution. A computer program was used to calculate the mean inclusion diameter as well as volume fraction using a line intercept method. This was done by measuring all inclusions which intercepted a fifty line grid. Fifty separate regions of a polished and unetched bulk specimen from each metal group were analyzed by this line intercept method.

A similar line intercept program was used to measure the mean grain diameter from etched bulk specimens of each metal group. again a fifty line grid was used to analyze the grain size at fifty separate regions of each etched specimen.

3.4.2 Scanning Electron Microscopy

A JEOL JSM-840 scanning electron microscope was used to analyze topographical features of the fracture surfaces from the tensile and three point bend specimens. A statistical

distribution of void (or dimple) sizes was obtained by manually measuring the void diameters, using a line intercept method, on numerous micrographs from the fracture surfaces of each specimen. This manual line intercept method was used to get a statistical representation of the size distribution of voids on both the tensile and the three point fracture surfaces for each metal group.

The critical plane strain stretch zone width (d') was also measured from the fractographs of the three point bend specimens. The stretch zone was measured in at least six locations in the plane strain region of the fracture surface. The average value of these measurements was taken to be d'.

3.4.3 X-Ray Analysis

Energy dispersive x-ray analysis was performed in the SEM using an EDAX system. The x-ray analysis was done on polished, unetched specimens. A semi-quantitative analysis of the chemical composition of the inclusions as well as the surrounding matrix material for all the metal groups was obtained by analyzing the respective characteristic x-ray energy spectra using a Tracor Northern Computerized Analysis System.

3.4.4 Transmission Electron Microscopy

The transmission electron microscopy of the strained and unstrained foils was performed on a PHILIPS EM300G microscope at the University of Manitoba as well as on a PHILIPS EM400 TEM/STEM microscope at the University of Virginia.

The distribution and density of small percipitates as well as the naturally occurring dislocation distributions was studied by the electron microscopy of the unstrained foils.

The microscopy of the strained foils was directed towards analyzing the process, or extent, of plastic deformation occurring in the foils as a result of tensile straining. In particular the size and development of dislocation structures with strain was analyzed qualitatively and quantitatively in terms of direct measurements from micrographs. The mean dislocation structure size was measured manually from micrographs using a line intercept method described earlier by Knossen and Kritzinger [71] and illustrated schematically in Figure 3.7.

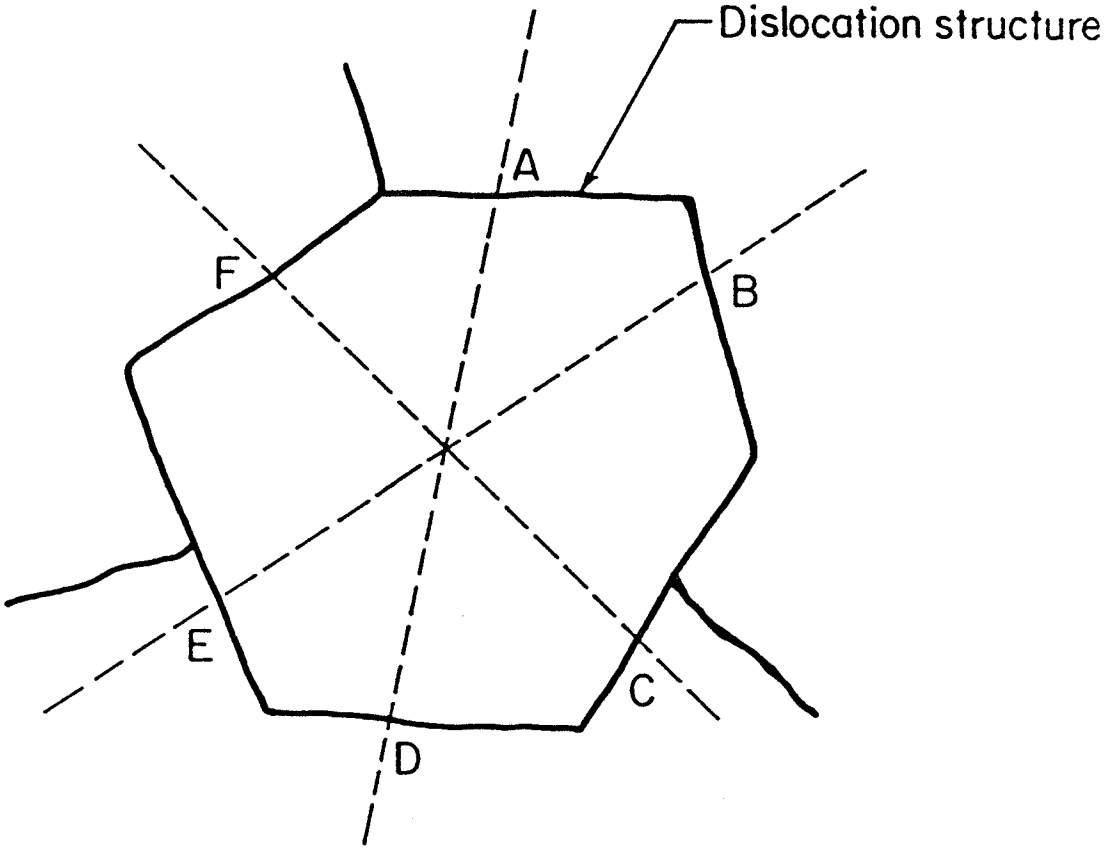

Figure 3.7: Line Intercept Method Used to Measure the Mean Dislocation Structure Diameter

Chapter IV

EXPERIMENTAL RESULTS

4.1 METALLOGRAPHIC EXAMINATION

The optical metallography performed on both etched and unetched samples from each metal group was used to categorize the material microstructure as well as to evaluate variations in the grain size and inclusion distribution.

4.1.1 Grain Size and Microstructure

Figure 4.1(a to f) shows the etched microstructures of the six metal groups taken from the bulk sections located in the transverse orientation with respect to the rolling direction. As is indicated by this series of micrographs, a similar ferrite-pearlite microstructure exists for all the metal groups. Also it is worth noting, concerning the microstructure, that the pearlite is directionally elongated, reflecting the influence of the controlled rolling where as the ferrite grains are virtually equiaxed.

The results of the grain size analysis are shown in Figure 4.2. Figure 4.2 indicates that metal groups 3 to 6 had a significant improvement in grain refinement over metal groups 1 and 2. In particular metal 6, with a grain size of

3.47μm, represented a 45% decrease in grain size compared to the base metal (metal 1) which had 6.27μm grains.

4.1.2 Inclusion Size and Distribution

Optical micrographs of the unetched samples displaying the size and distribution of nonmetallic inclusions are shown in Figures 4.3(a to f). These micrographs indicate that the inclusions are distributed in directional strings probably resulting from the controlled rolling. The individual inclusions are not elongated however but are primarily spherical in shape for all the metal groups. The results of the computerized image analysis on these inclusion populations are presented in Figures 4.4 and 4.5. Figure 4.4 shows that the mean inclusion diameter varied from 5.33μm to 3.87μm across the six metal groups. The inclusion diameter was largest in metals 1 and 2 while metals 3 to 6 displayed a decrease in mean inclusion size. Figure 4.5 indicates that the volume fraction of the material occupied by the inclusions ranged from 1.77% to 0.10% depending on the metal group. The variation in volume fraction of inclusions among the metal groups reinforces the trend displayed in Figure 4.4. Metals 1 and 2 had higher inclusion volume fractions then did metals 3 to 6.

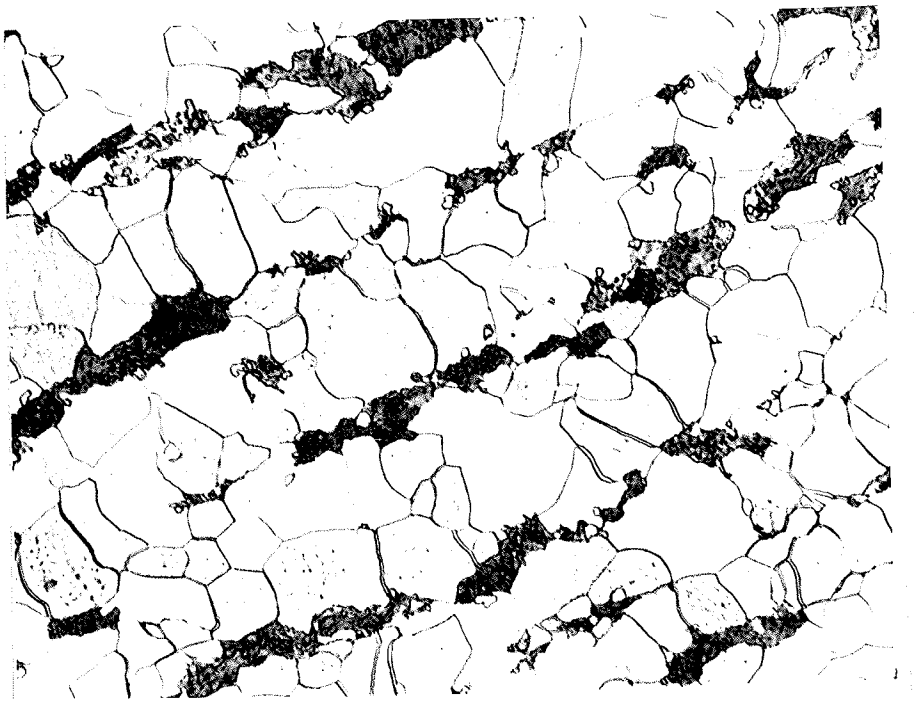

Figure 4.1(a): Etched Microstructure of Metal 1, 1000X

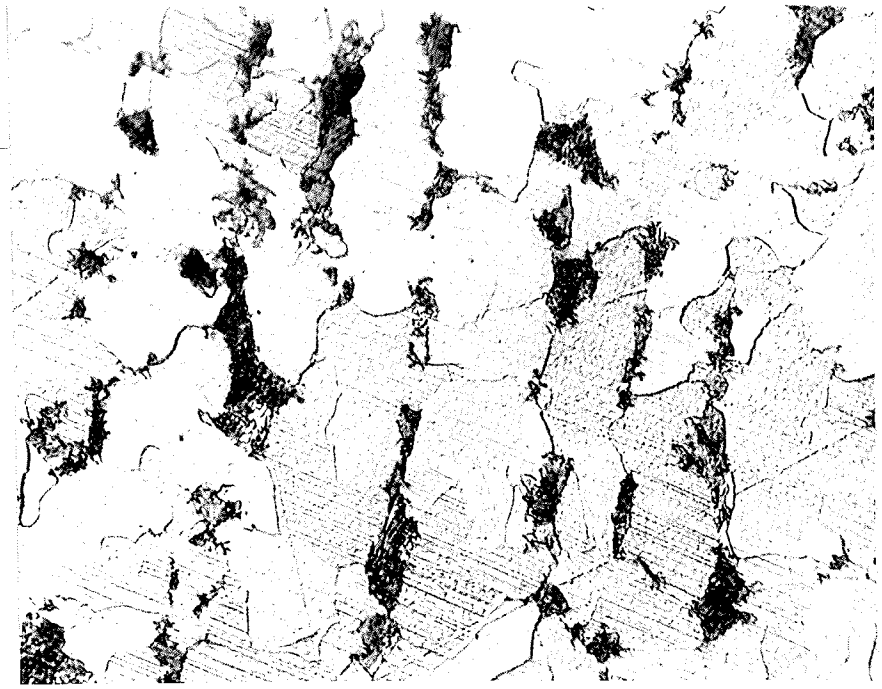

Figure 4.1(b): Etched Microstructure of Metal 2, 1000X

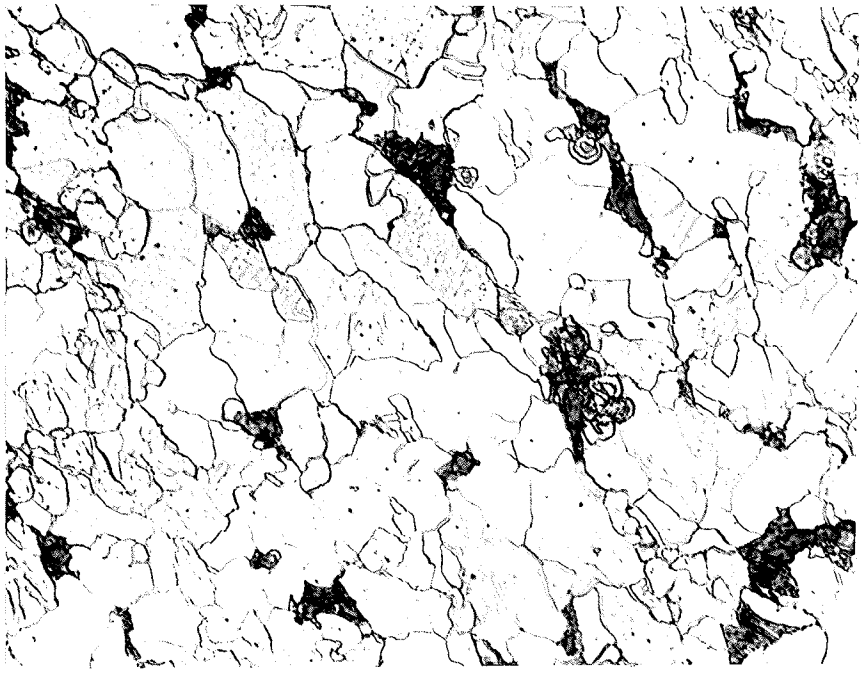

Figure 4.1(c): Etched Microstructure of Metal 3, 1000X

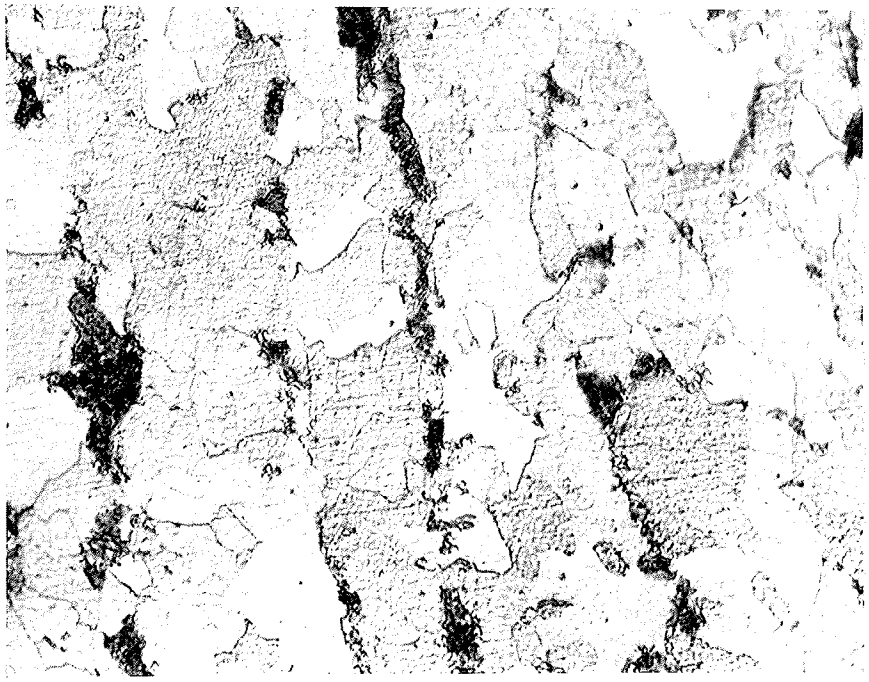

Figure 4.1(d): Etched Microstructure of Metal 4, 1000X

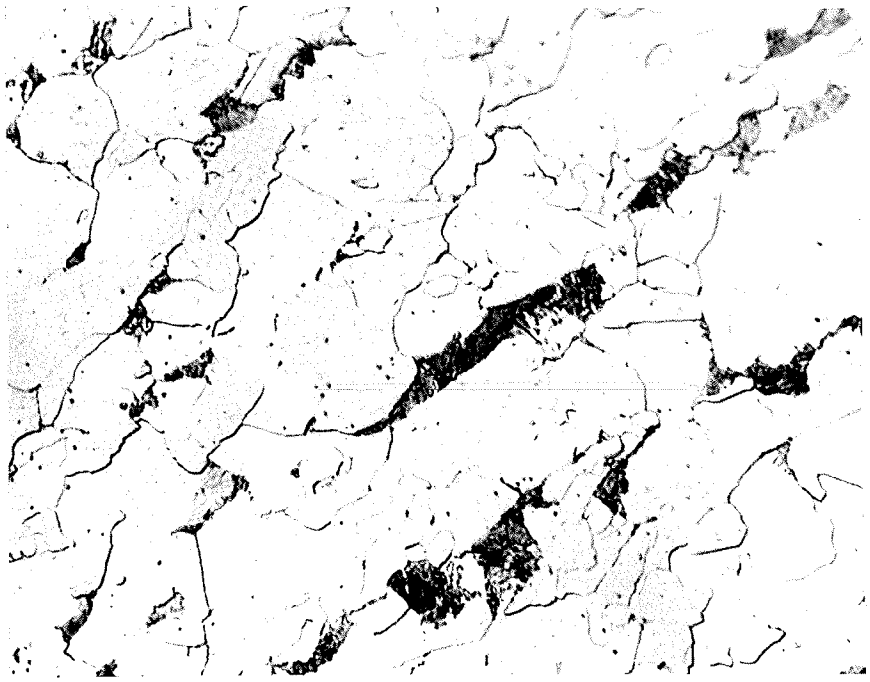

Figure 4.1(e): Etched Microstructure of Metal 5, 1000X

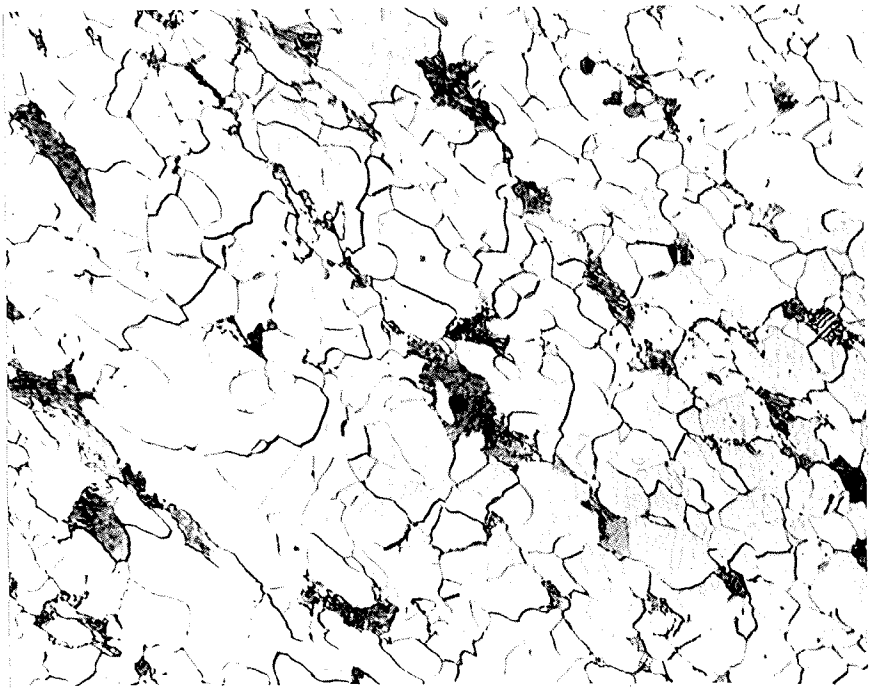

Figure 4.1(f): Etched Microstructure of Metal 6, 1000x

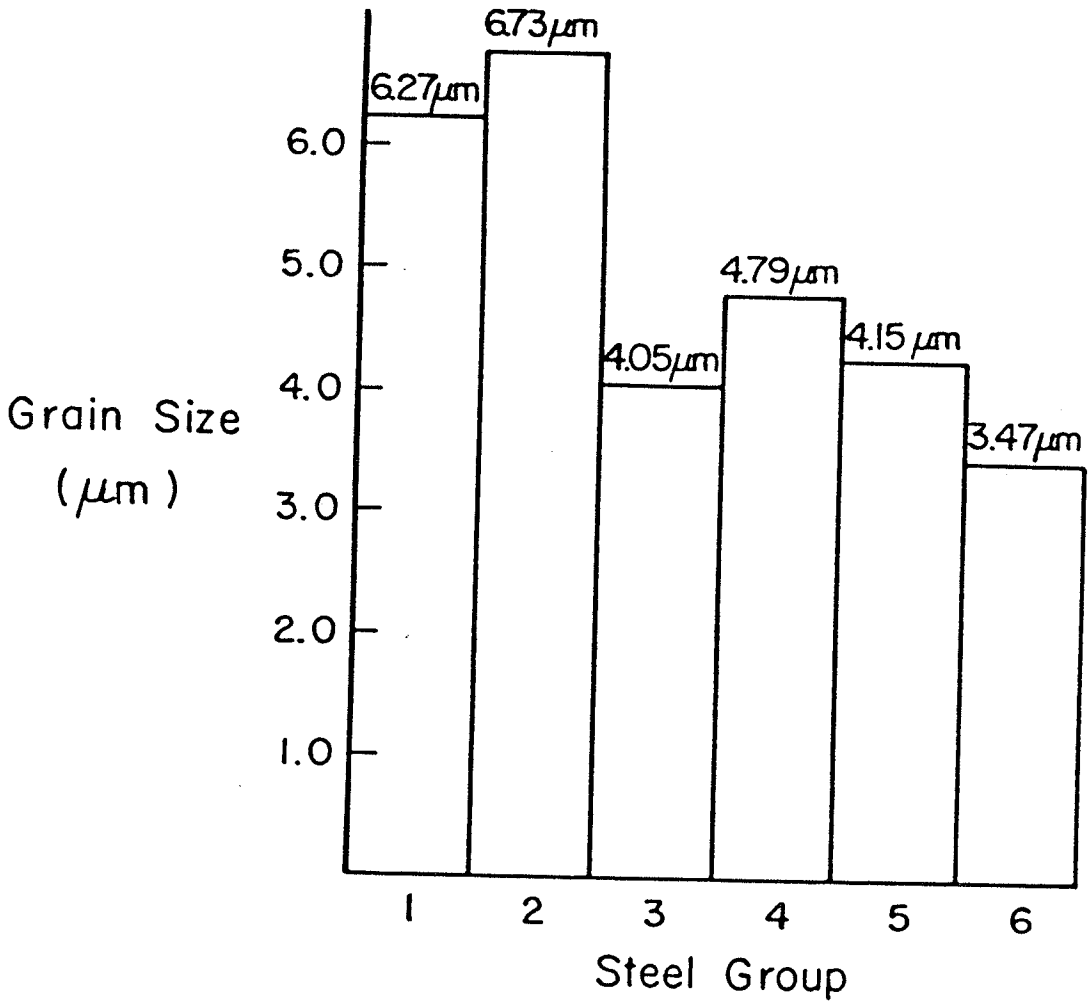

Figure 4.2: Variations in Grain Size Among the Metal Groups

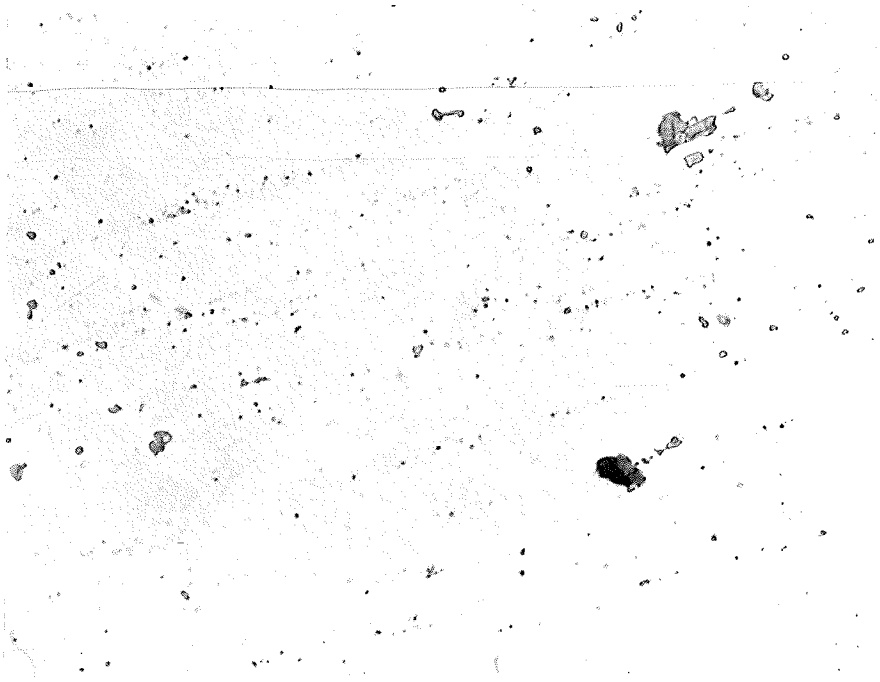

Figure 4.3(a): Inclusion Distribution in Metal 1, 1000X

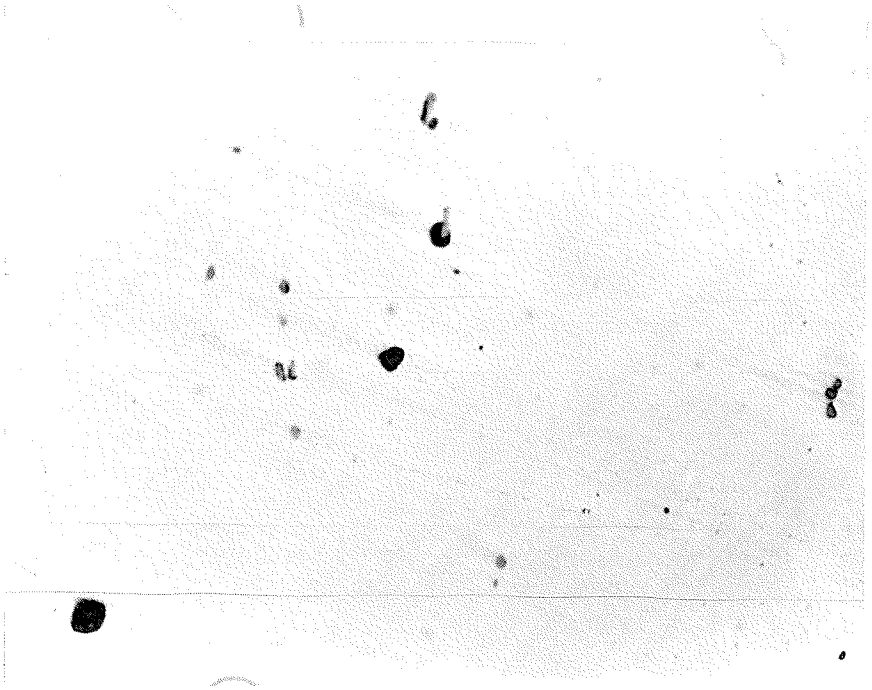

Figure 4.3(b): Inclusion Distribution in Metal 2, 1000X

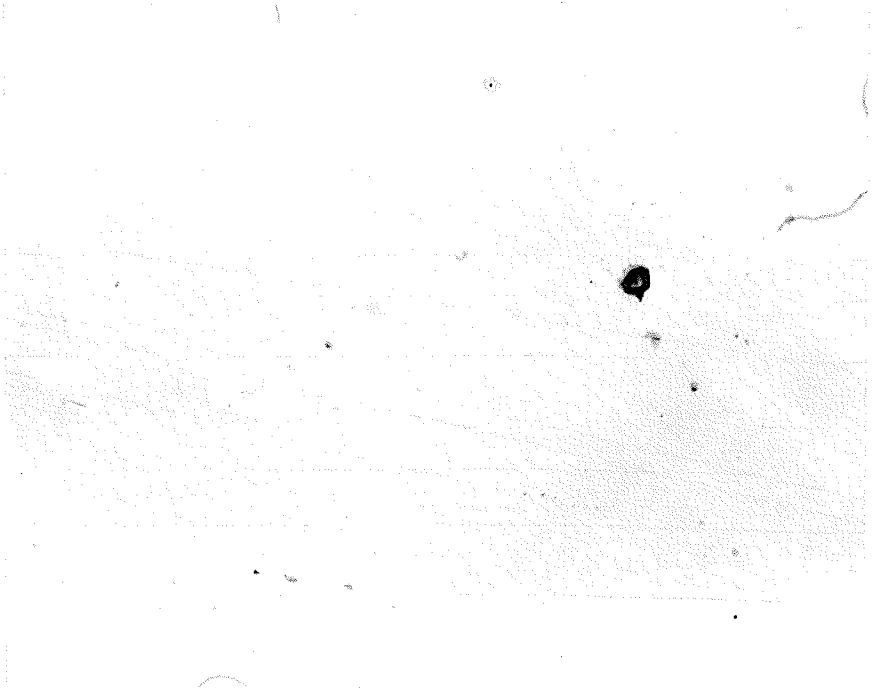

Figure 4.3(c): Inclusion Distribution in Metal 3, 1000X

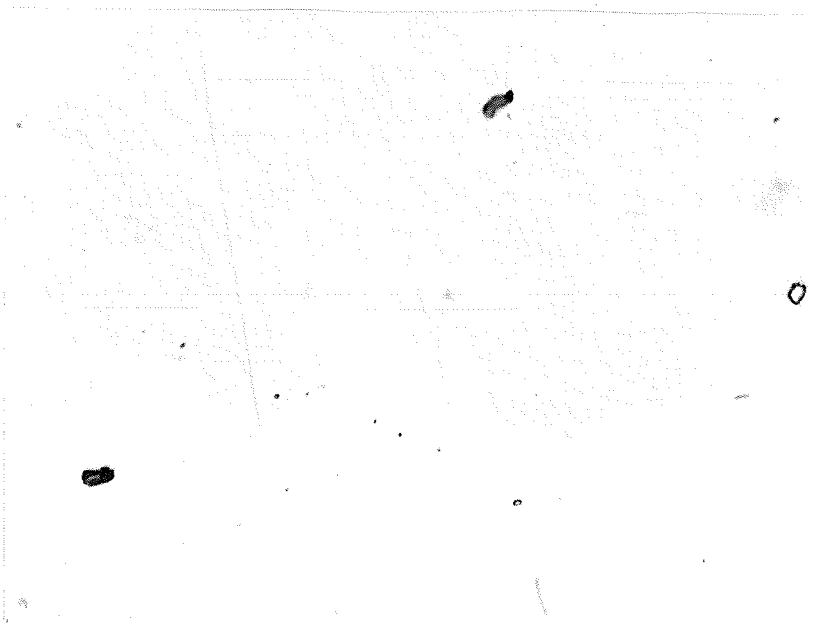

Figure 4.3(d): Inclusion Distribution in Metal 4, 1000X

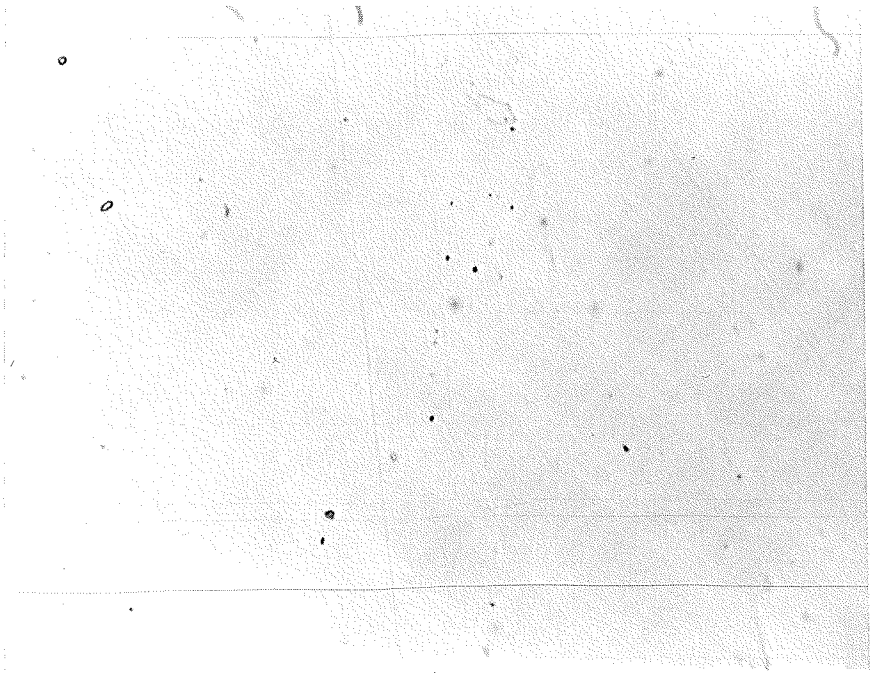

Figure 4.3(e): Inclusion Distribution in Metal 5, 1000X

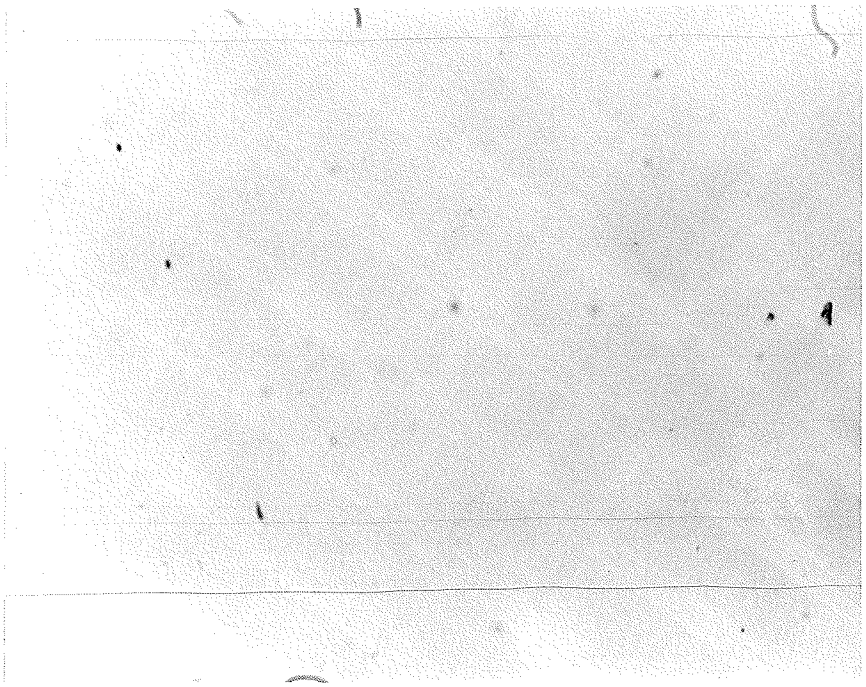

Figure 4.3(f): Inclusion Distribution in Metal 6, 1000X

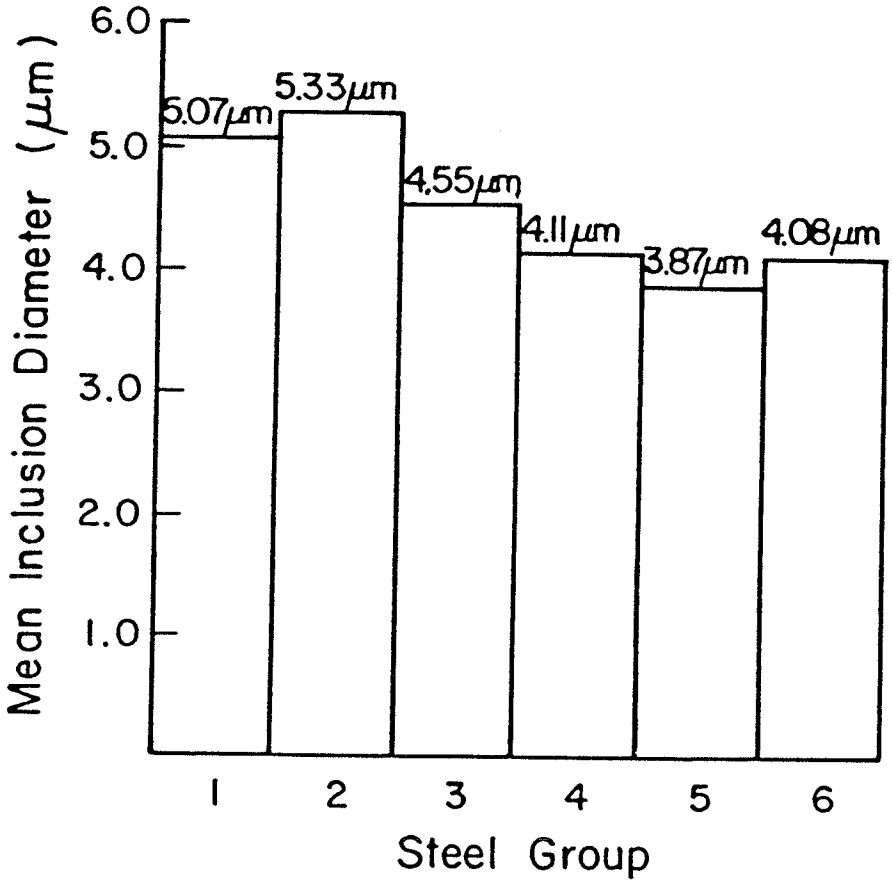

Figure 4.4: Variations in the Mean Inclusion Diameter Among the Metal Groups

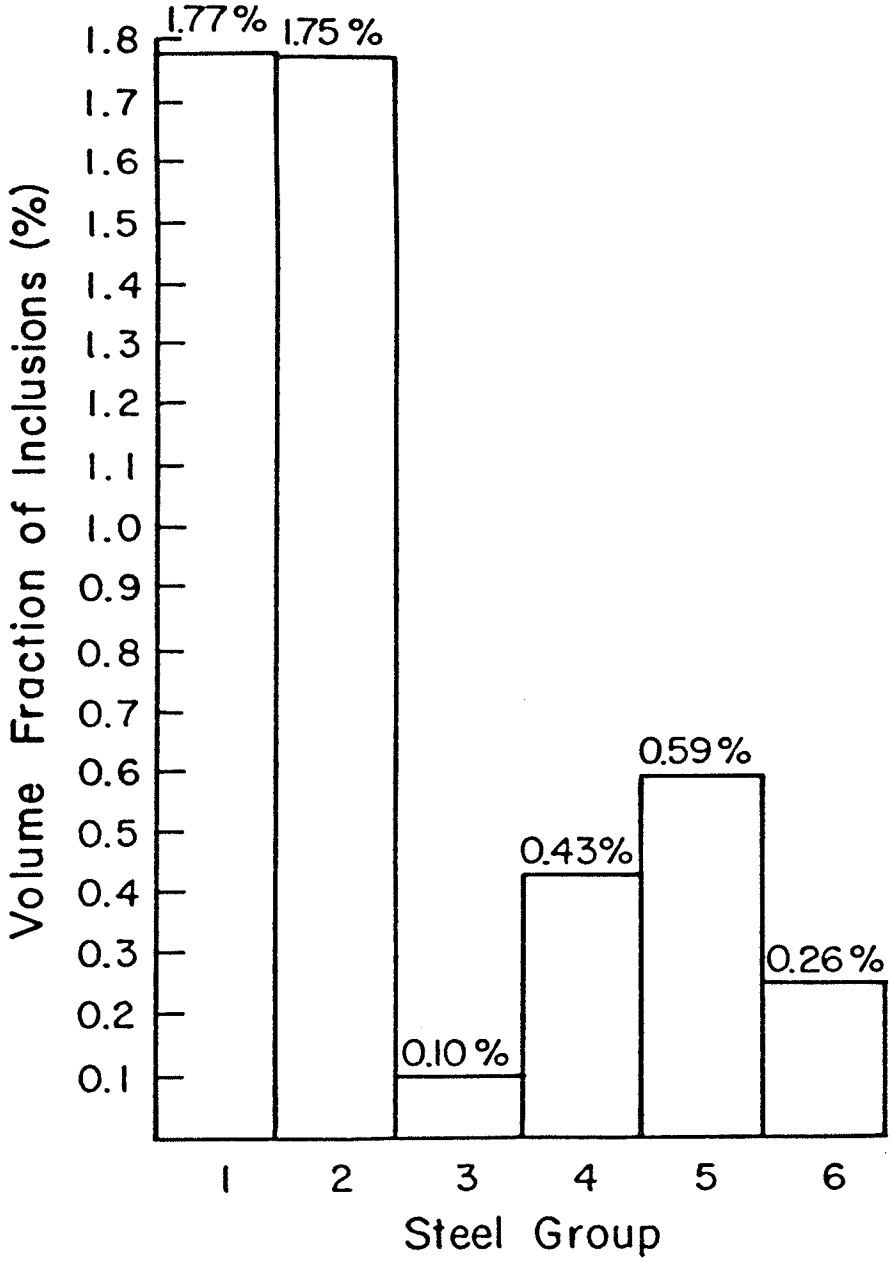

Figure 4.5: Variations in the Inclusion Volume Fraction Among the Metal Groups

4.2 TENSILE TEST RESULTS

The results obtained from the tensile testing of the six metal groups are presented in Table 4.1 . The ultimate tensile strength is shown to range from 467.3 MPa for metal 1 to 547.4 MPa for metal 4. Aside from metal 1, which contained a significantly lower σ_{uts}, the other metal groups had similar ultimate tensile strengths, as shown in Table 4.1 The yield stress, σ_y, also given in Table 4.1 ranges from 351.0 MPa for metal 1 to 467.1 MPa for metal 5. The strain hardening exponent, n, varies from a maximum of 0.318 for metal 1 to 0.253 for metal 4. Table 4.1 indicates that metals 3 to 6 have very similar values of n while metals 1 and 2 have higher values. The percentage elongation to fracture for the tensile specimens is also given in Table 4.1 With elongation values ranging from 31.5% for metal 6 to 37.1% for metal 2, it is obvious that the elongation to fracture was similar for all the metal groups. Table 4.1 indicates that the fracture strain, ϵ_f, ranges from 44.0% for metal 1 to 32.4% for metal 2. Although metal 1 had the highest fracture strain, Table 4.1 indicates that all the metal groups displayed much the same strain to fracture. Finally the percentage reduction in cross sectional area ,RA, is also given in Table 4.1 Metal 1 is shown to have the lowest RA (78.9%) while metals 2 to 6 had nearly identical RA values ranging from 84.4% to 86.8%.

Figure 4.6 indicates the variation in flow stress (σ flow), defined as the average of the yield stress and the ultimate tensile strength, among the different metal groups tested. Figure 4.6 indicates that metal groups 2 to 6 have significantly improved flow stresses than does the base metal with metal 5 having the highest flow stress (505.1 MPa).

TABLE 4.1

Tensile Test Results

Steel	Ultimate Tensile Stress, σ_{UTS} (Mpa.)	Yield Stress, σ_y (Mpa.)	Strain Hardening Exponent, n	Elongation (%)	Fracture Strain, ϵ_f (%)	RA (%)
1	467.3	351.0	0.318	36.1	44.0	78.9
2	495.4	394.0	0.277	37.1	38.0	86.1
3	528.3	456.5	0.258	34.4	39.5	86.8
4	547.4	439.2	0.253	31.9	32.4	86.0
5	543.2	467.1	0.265	33.2	35.0	84.9
6	508.8	408.7	0.267	31.5	32.5	84.4

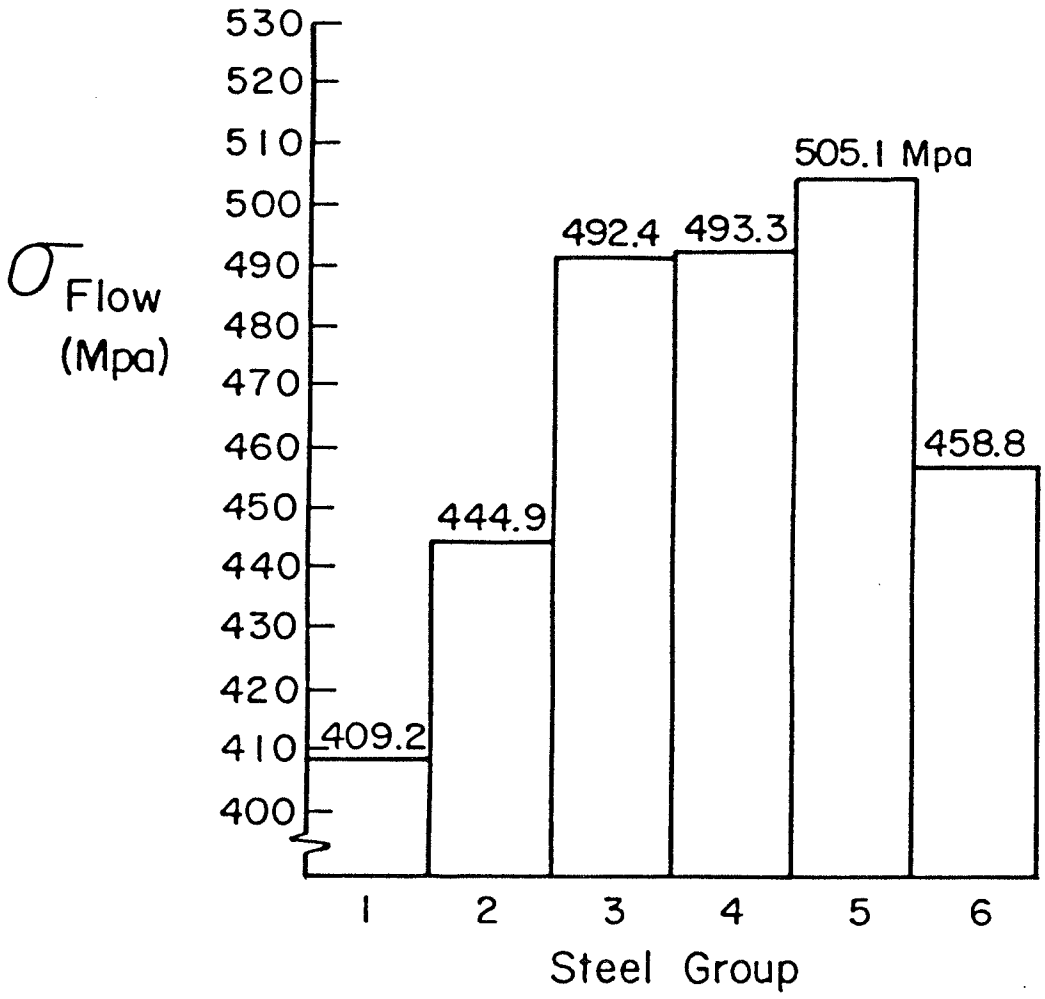

Figure 4.6: Variations in Flow Stress, σ_{flow}, Among the Metal Groups.

4.3 FRACTURE TEST RESULTS

SEM analysis of the precracked three point bend specimens, which were subsequently fractured under quasi-static conditions for determination of J_{IC} , are shown in Figure 4.7(a to f). From these micrographs the stretch zones, created during crack tip blunting, are visible. The average plane strain stretch zone width, measured from Figure 4.7(a to f) , are shown for each metal group in Figure 4.8. Figure 4.8 indicates that the average stretch zone width ranges from 69.3μm in metal 1 to 110.8μm in metal 3. It can also be seen that metals 1 and 2 have significantly smaller stretch zone widths than do metals 3 to 6.

The critical J integral (J_{IC}) was calculated by equation 2.5. The flow stress data from Figure 4.6 and the average stretch zone widths from Figure 4.8 were used in the determination of J_{IC} values for the metal groups. Figure 4.9 shows the calculated critical J integeral for each metal group. In Figure 4.9 , metal groups 1 and 2 had the lowest calculated J_{IC}values (83.0 KJ/M^{2}and 92.8 KJ/M^{2}respectively) while metals 3 to 6 had significantly improved fracture toughness as a combined result of large stretch zone widths and high flow stresses. Specifically metals 3 and 6 had the highest J_{IC} values of 159.7 KJ/M^{2}and 132.1 KJ/M^{2}respectively.

Figure 4.7(a): Stretch Zone Region (Metal 1)

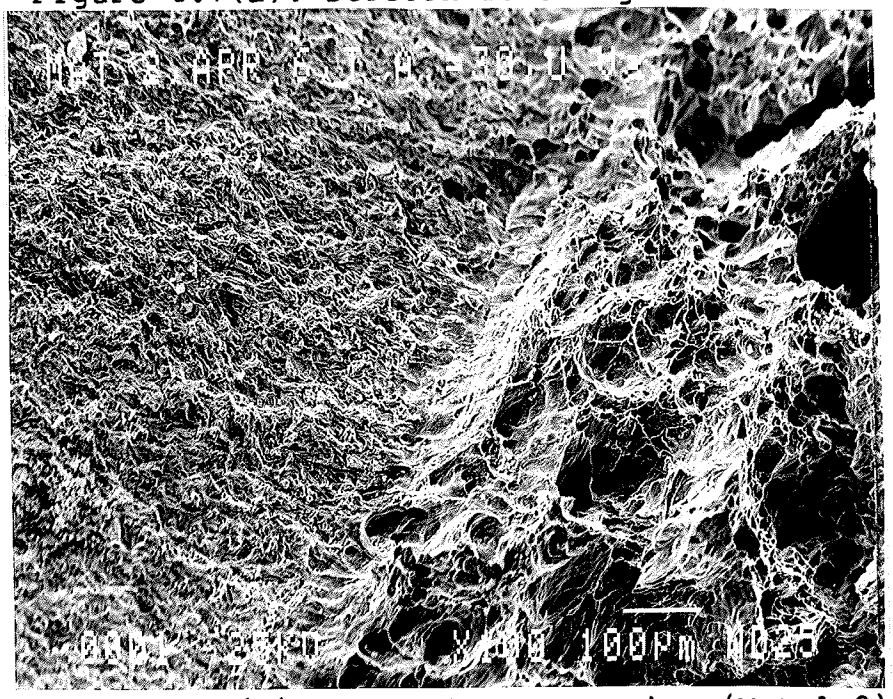

Figure 4.7(b): Stretch Zone Region (Metal 2)

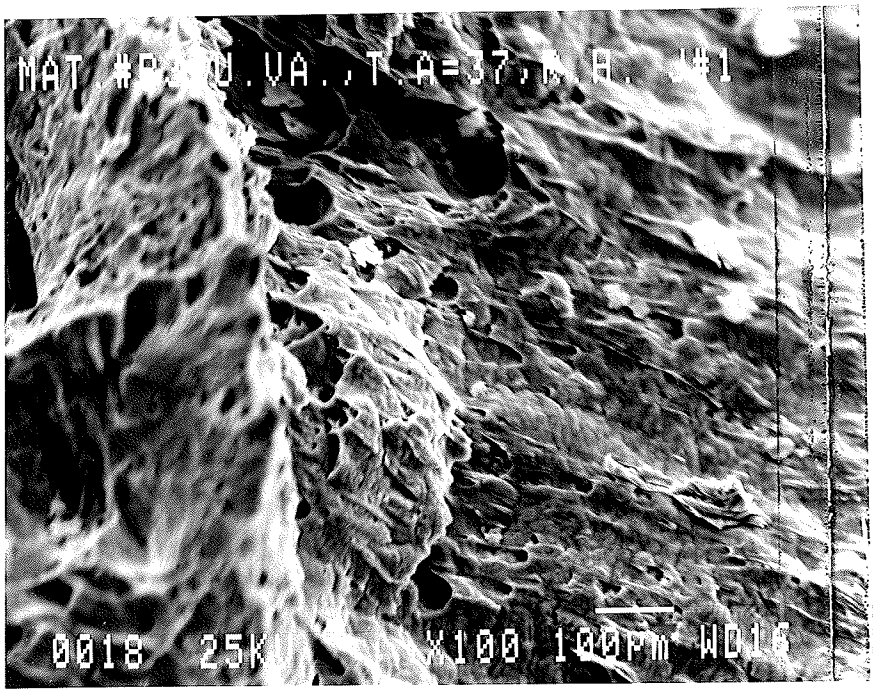

Figure 4.7(c): Stretch Zone Region (Metal 3)

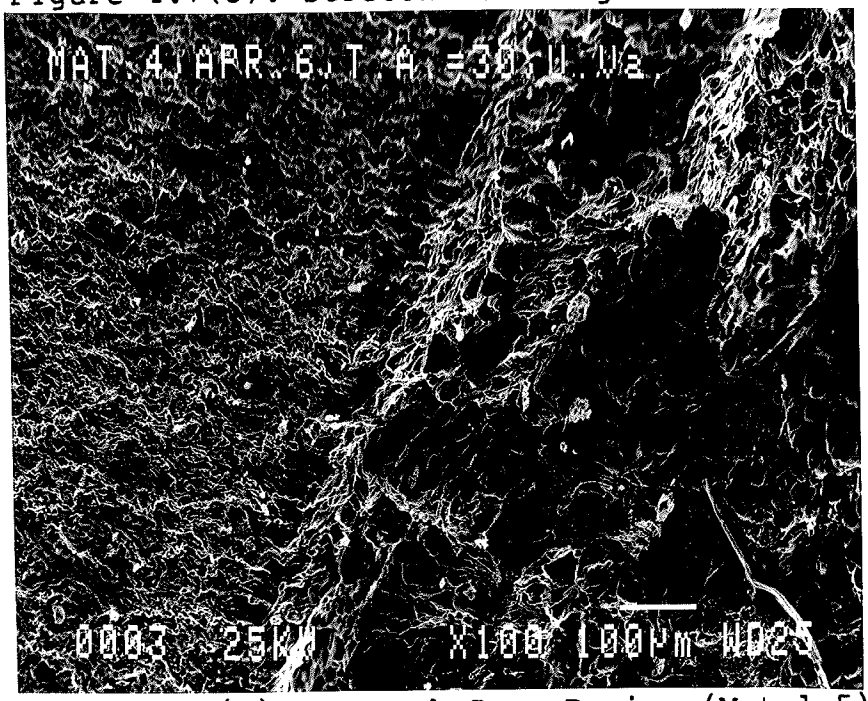

Figure 4.7(d): Stretch Zone Region (Metal 5)

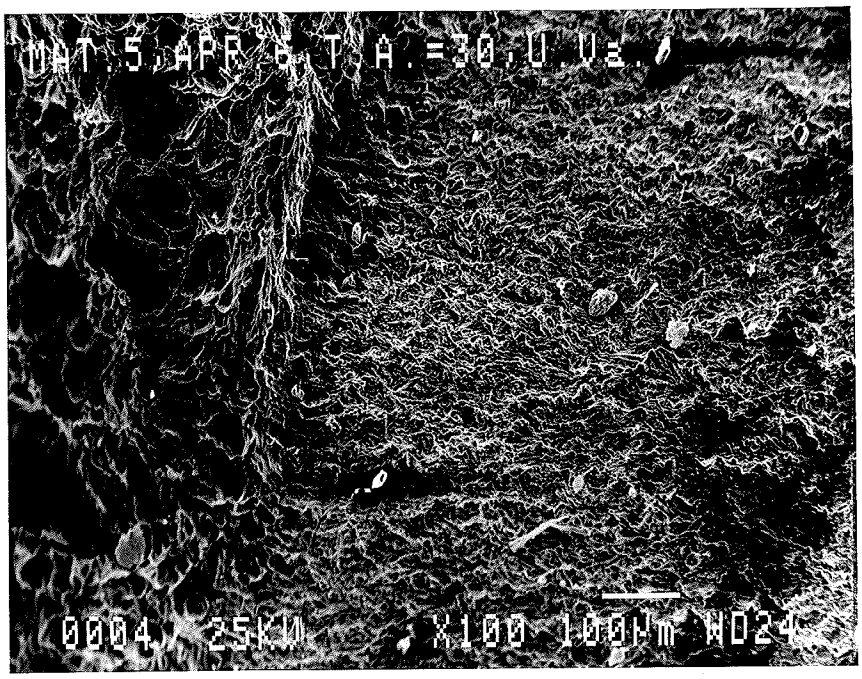

Figure 4.7(f): Stretch Zone Region (Metal 5)

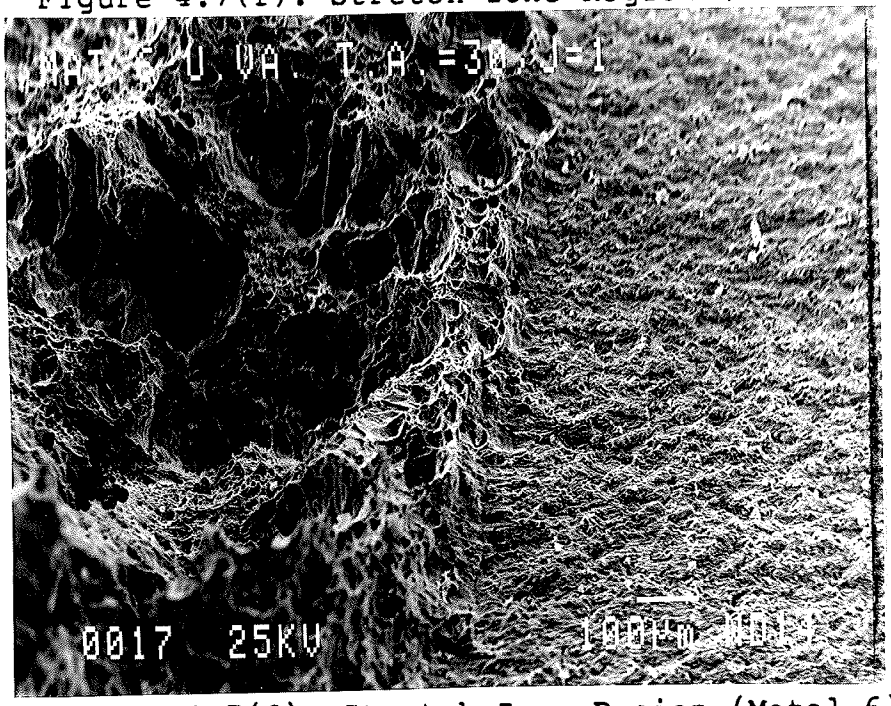

Figure 4.7(f): Stretch Zone Region (Metal 6)

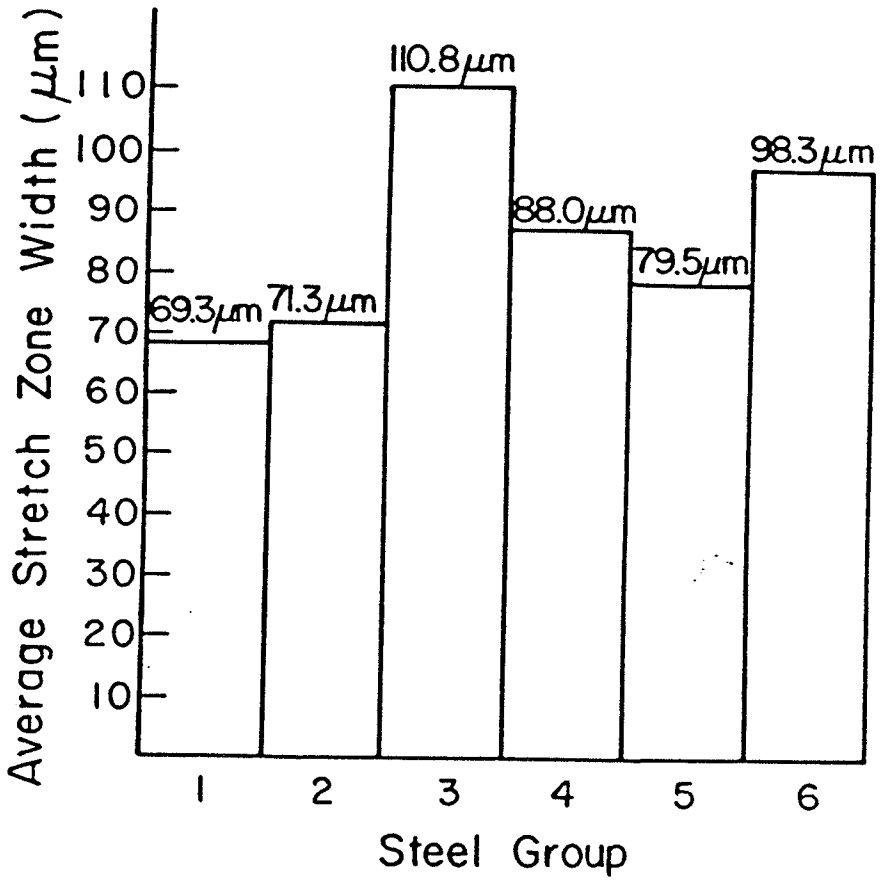

Figure 4.8: Variations in Stretch Zone Width Among the Metal Groups

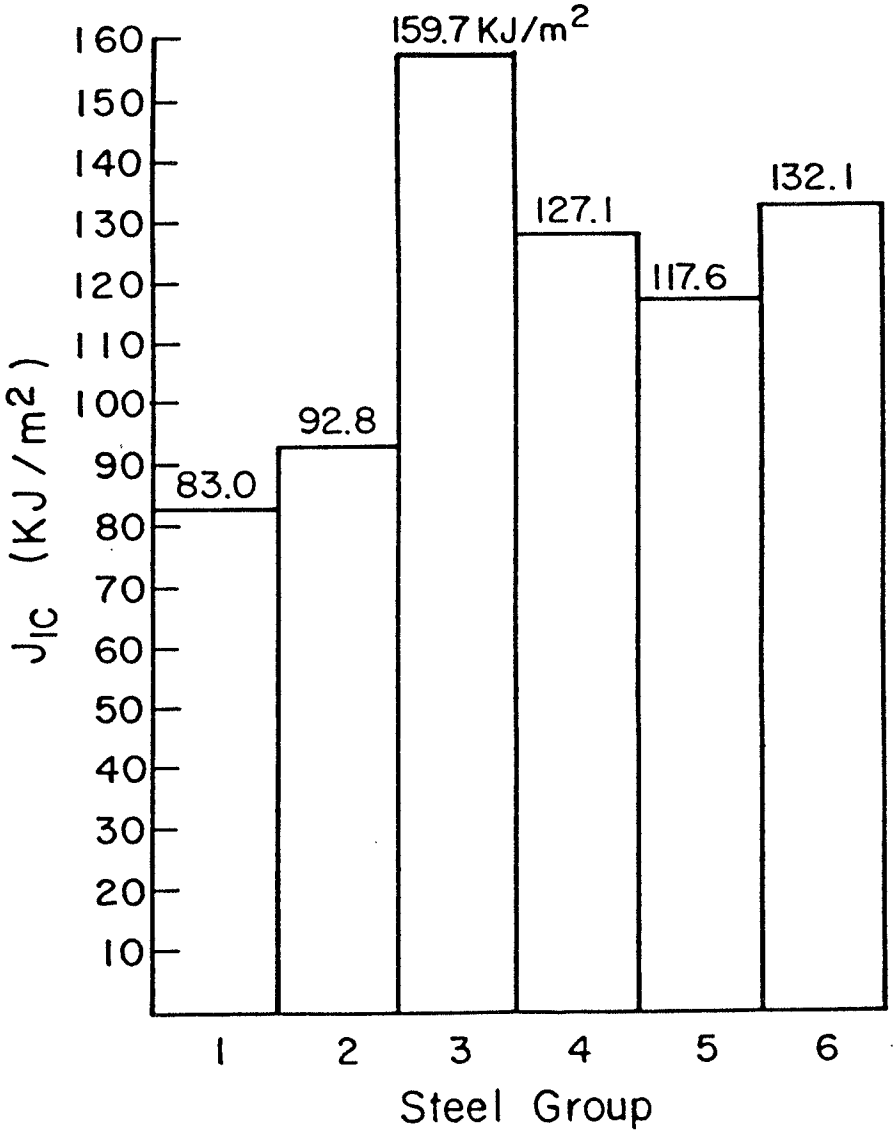

Figure 4.9: Variations in J_{IC} Among the Metal Groups

4.4 CORRELATIONS BETWEEN MICROSTRUCTURE AND FRACTURE TOUGHNESS

Some trends resulting from the correlation of microstructural material properties with macroscopic fracture toughness are shown in Figures 4.10 to 4.12. Figure 4.10 shows J_{Ic} as a function of grain size. This graph indicates that higher values of J_{Ic} correspond to metal groups with smaller grain size. This general trend relating increased fracture toughness to grain refinement was substantiated in the literature [72,73]. Figure 4.11 shows a tendency toward a higher fracture toughness with smaller mean inclusion diameters. Likewise, when plotting J_{Ic} versus inclusion volume fraction, Figure 4.12 , there is an obvious trend to higher fracture toughness with a lower inclusion volume fraction.

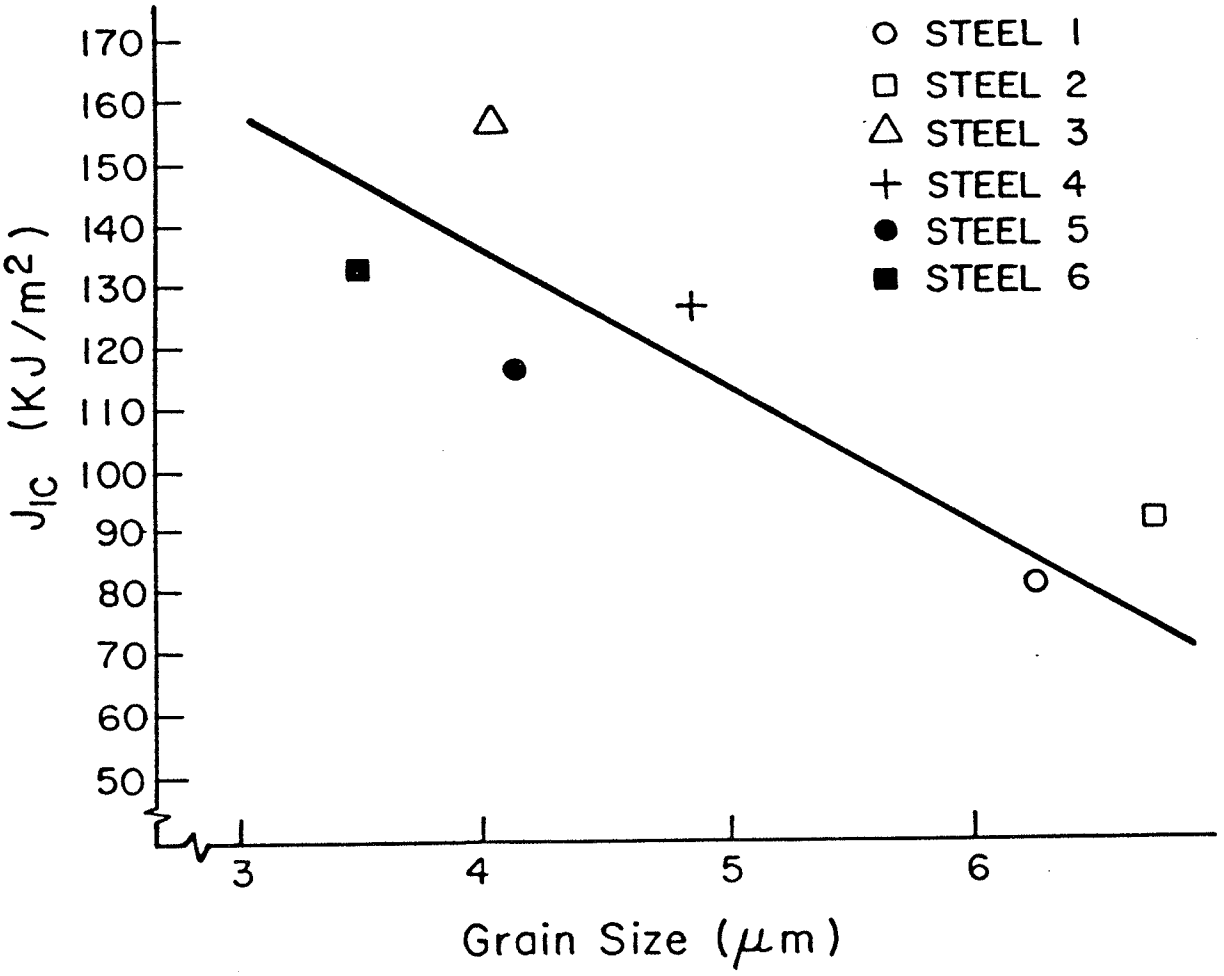

Figure 4.10: Variations in J_{IC} With Grain Size

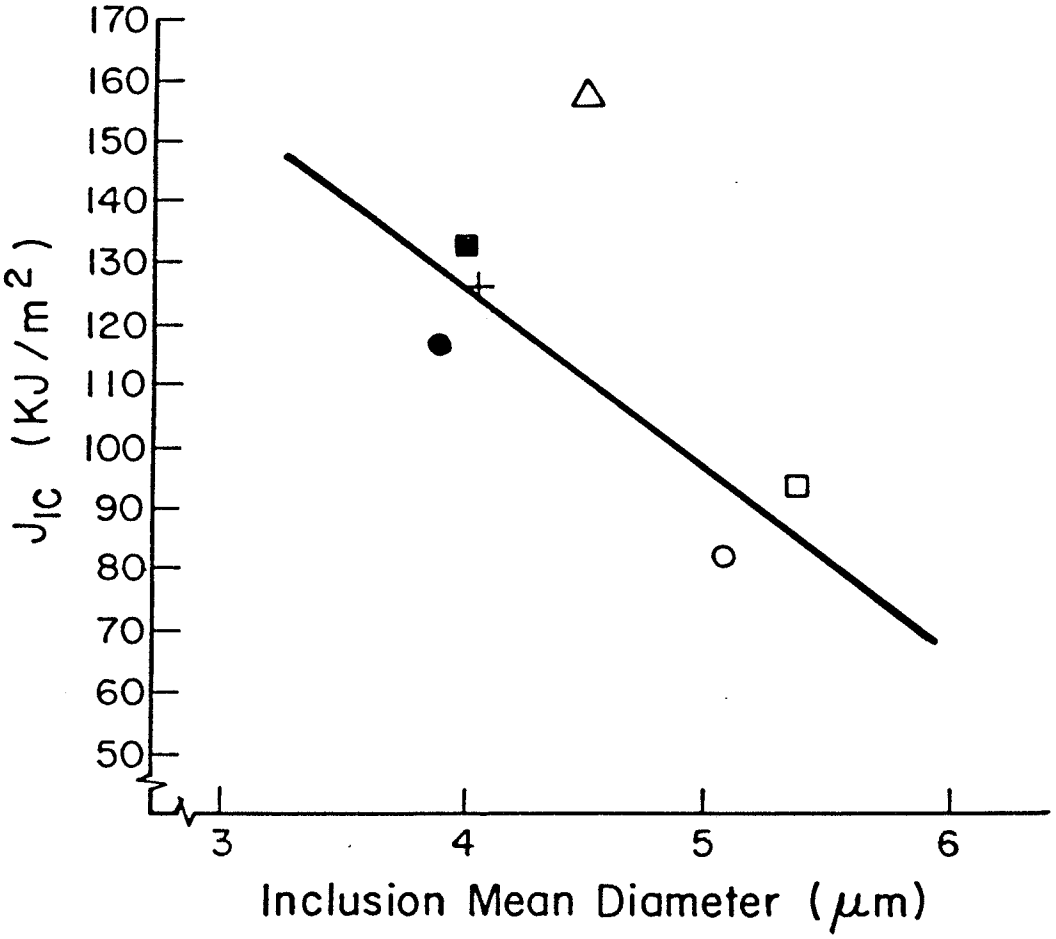

Figure 4.11: Variations in J_{IC} With Mean Inclusion Diameter

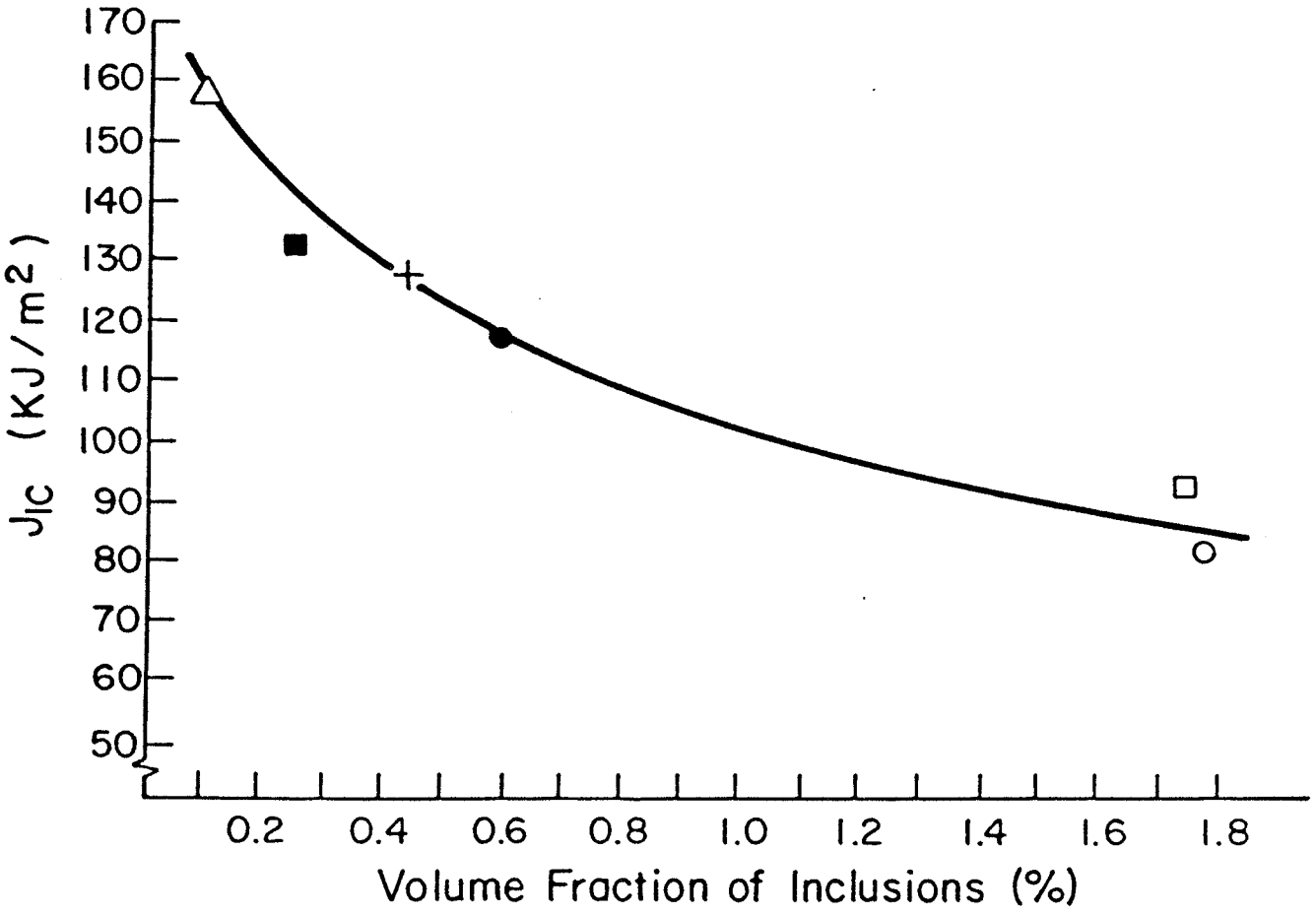

Figure 4.12: Variations in J_{IC} With Inclusion Volume Fraction

4.5 SCANNING ELECTRON MICROSCOPY RESULTS

4.5.1 Tensile Fracture Surfaces

SEM micrographs of characteristic tensile fracture surfaces for each metal group are shown in Figures 4.13(a to f). These figures indicate that a uniform distribution of voids was present for for all the metal groups. The shape of the voids are primarily circular and of uniform size. A statistical analysis of the size distribution of voids, or dimples, on the tensile fracture surfaces of each metal group is shown in Figures 4.14(a to f).

4.5.2 Precracked Three Point Fracture Surfaces

The SEM micrographs of fractured three point bend specimens displayed, in contrast to the tensile fracture surfaces, a much more irregular topography, as shown in Figure 4.15(a to f). The large and elongated dimples displayed on these fracture surfaces differ markedly from the small and more circular dimples shown in Figure 4.13(a to f). A statistical analysis of the size and distribution of voids on the precracked three point bend fracture surfaces of each metal group are shown in Figure 4.16(a to f). The results shown on these graphs indicate a statistical peak corresponding to a void size of approximately 15μm for all the metal groups. Thus, precracked (triaxial) fracture surfaces seem to have voids which are larger by a factor of ten than tensile (uniaxial) fracture surfaces from the same metal group.

Figures 4.17 and 4.18 show the location of nonmetallic inclusions within dimples for both tensile and three point fracture surfaces, which would indicate that void nucleation at inclusions takes place during ductile fracture in these particular steels.

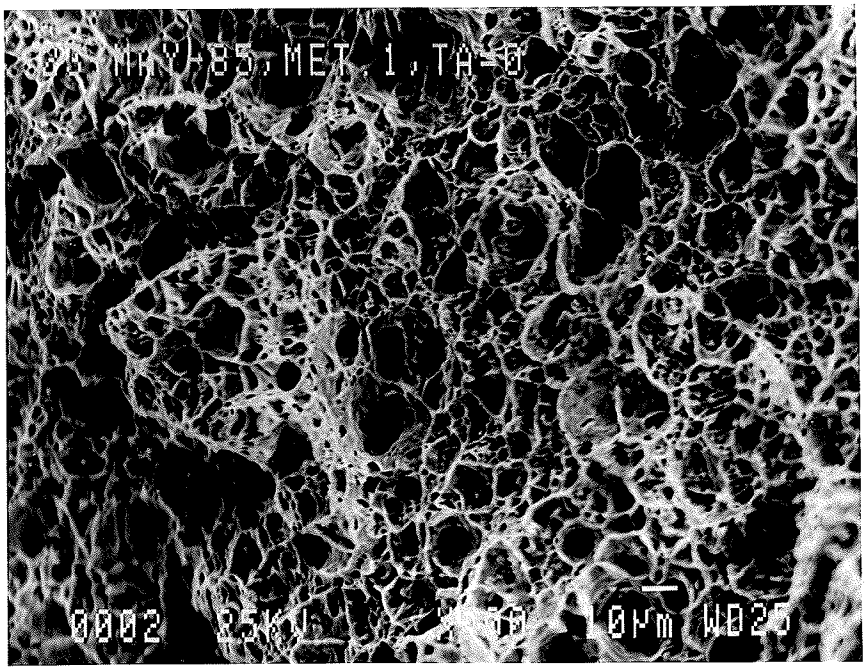

Figure 4.13(a): Tensile Fracture Surface of Metal 1

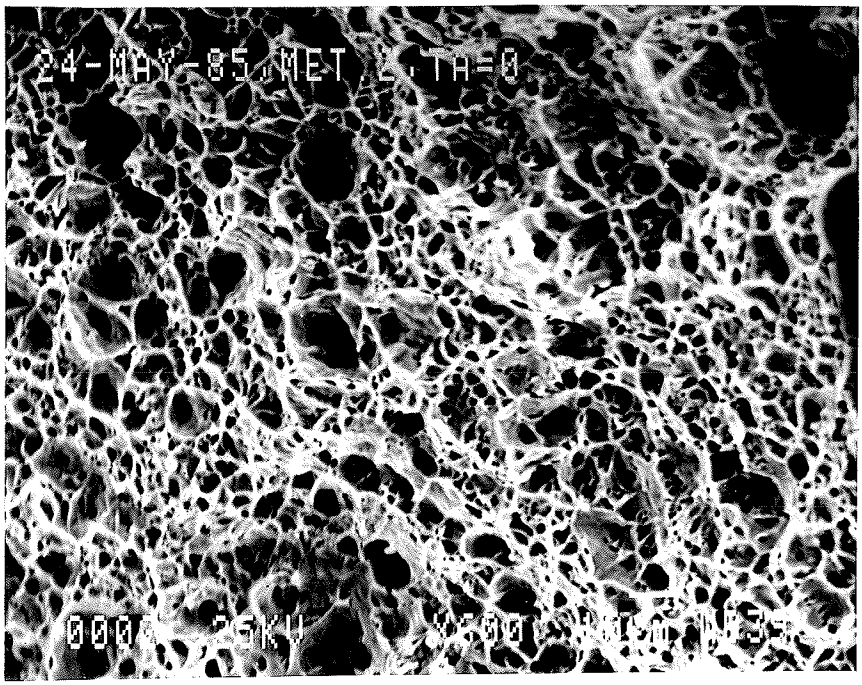

Figure 4.13(b): Tensile Fracture Surface of Metal 2

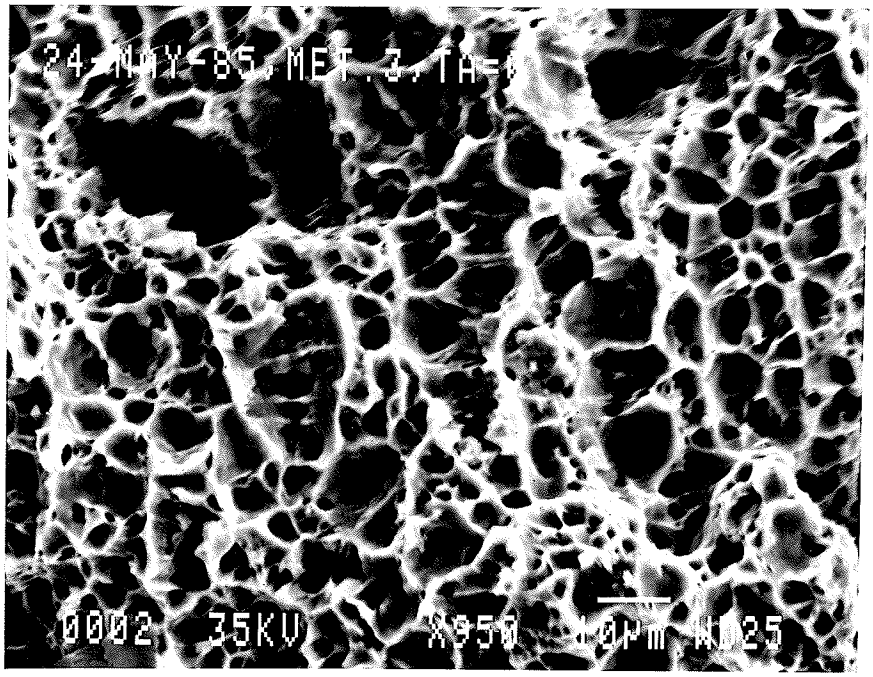

Figure 4.13(c): Tensile Fracture Surface of Metal 3

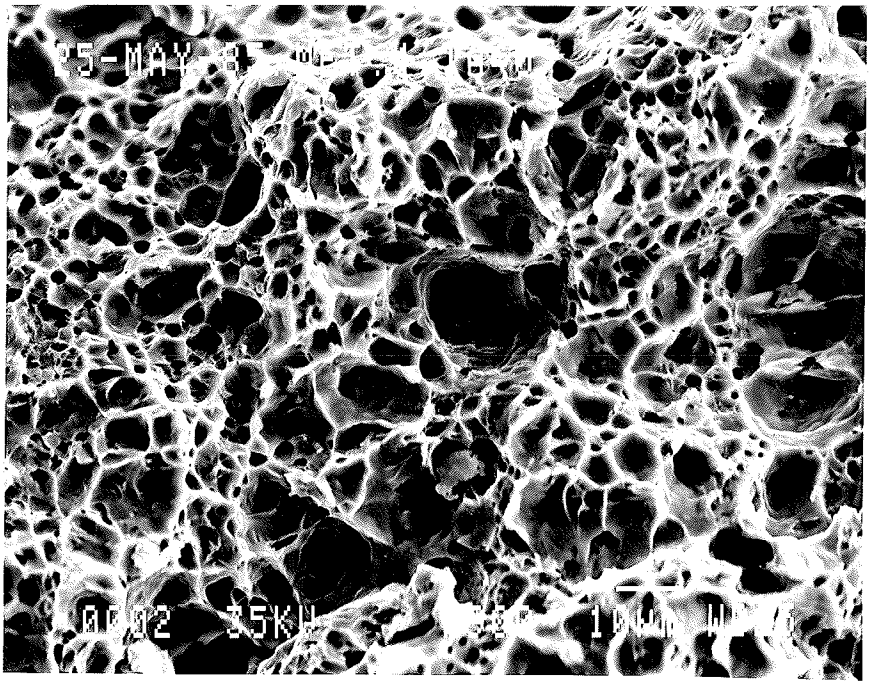

Figure 4.13(d): Tensile Fracture Surface of Metal 4

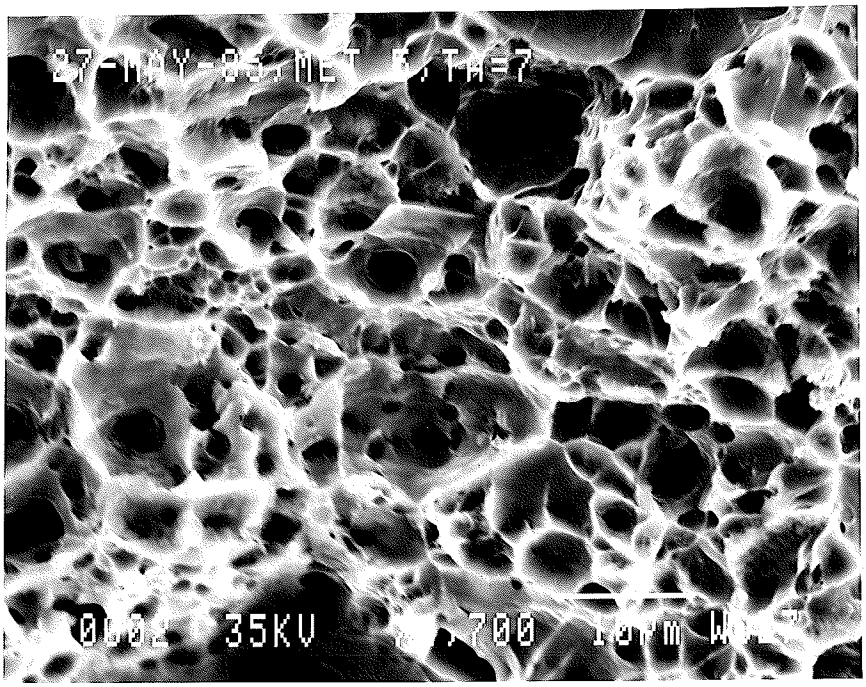

Figure 4.13(e): Tensile Fracture Surface of Metal 5

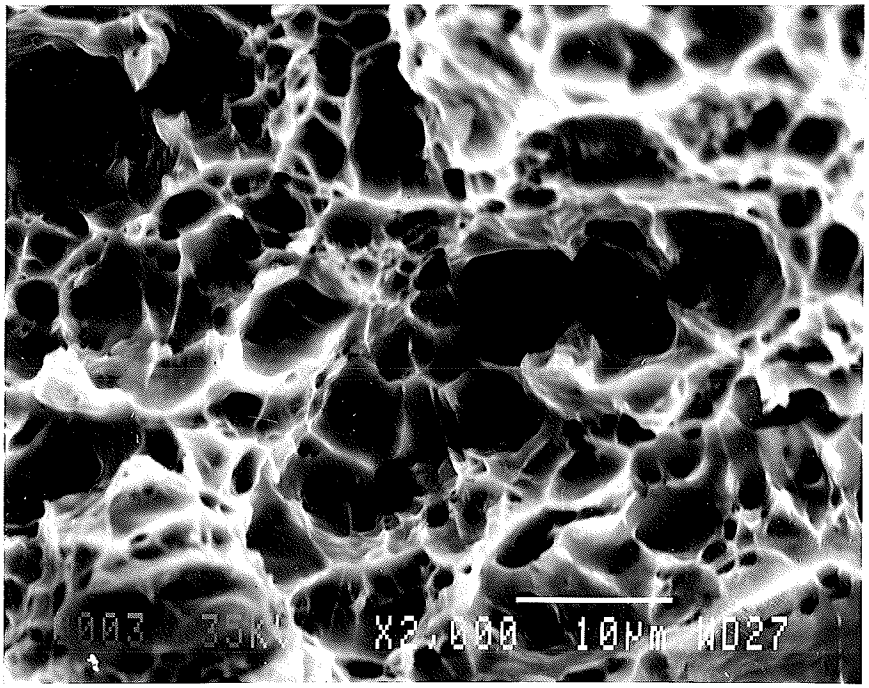

Figure 4.13(f): Tensile Fracture Surface of Metal 6

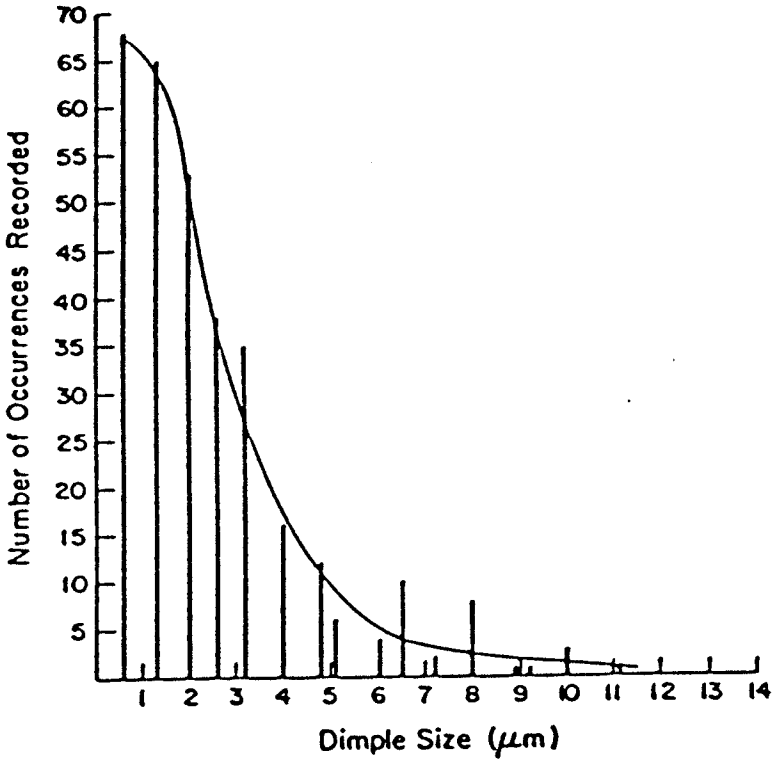

Figure 4.14(a): Void Size Distribution on Tensile Fracture Surfaces of Metal 1

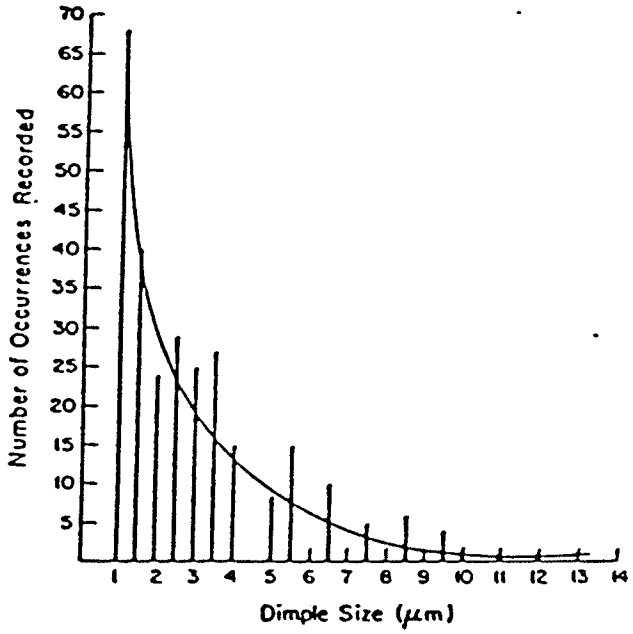

Figure 4.14(b): Void Size Distribution on Tensile Fracture Surfaces of Metal 2

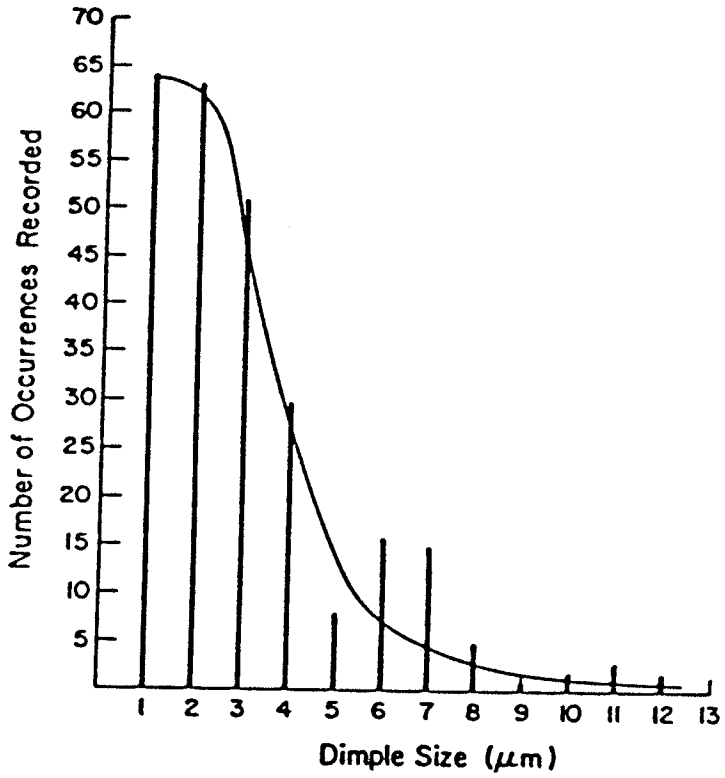

Figure 4.14(c): Void Size Distribution on Tensile Fracture Surfaces of Metal 3

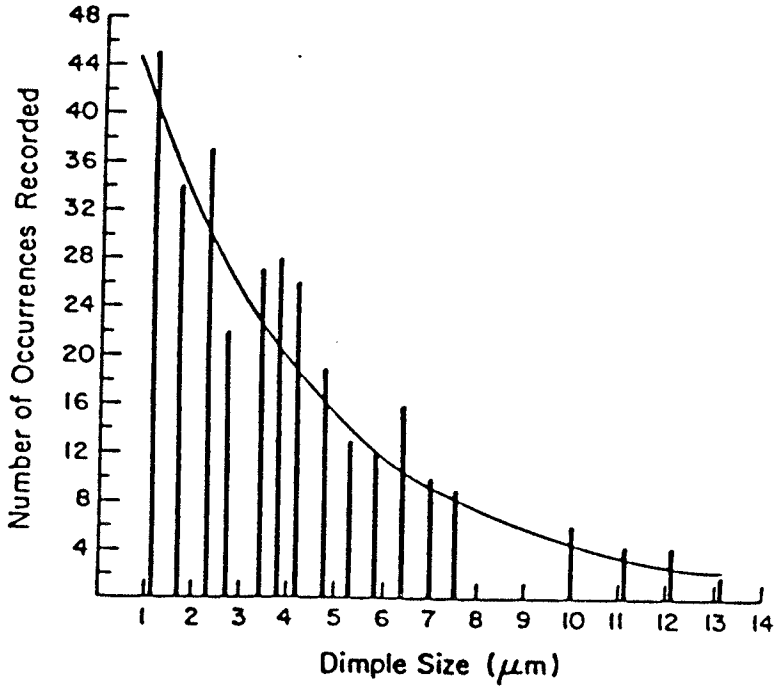

Figure 4.14(d): Void Size Distribution on Tensile Fracture Surfaces of Metal 4

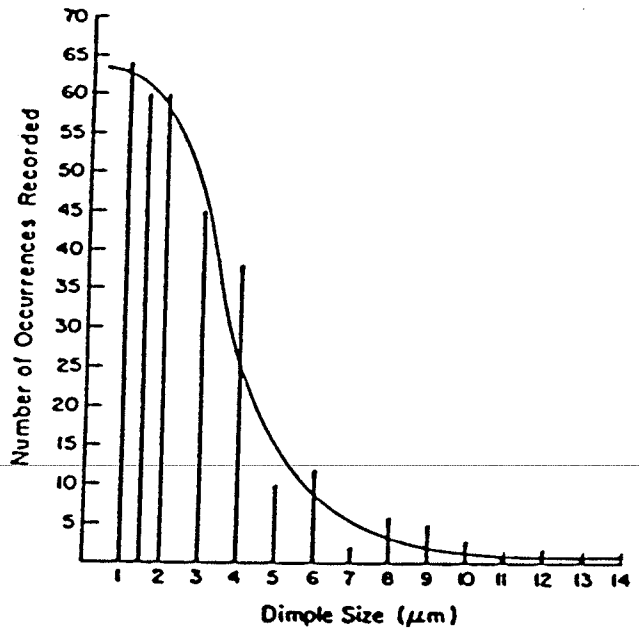

Figure 4.14(e): Void Size Distribution on Tensile Fracture Surfaces of Metal 5

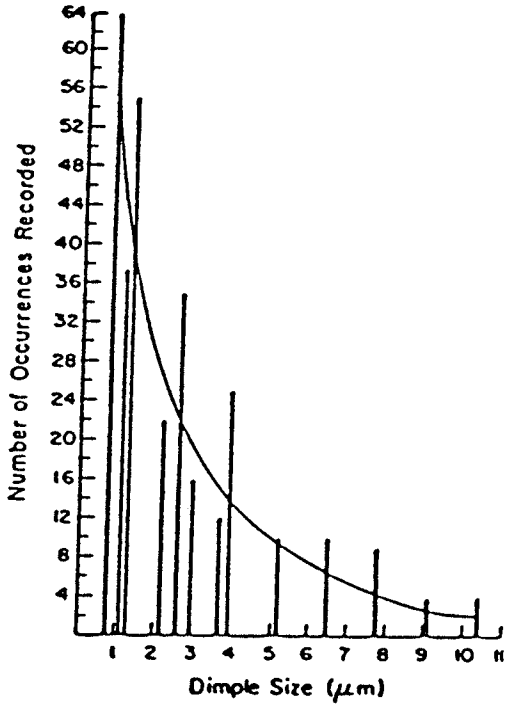

Figure 4.14(f): Void Size Distribution on Tensile Fracture Surfaces of Metal 6

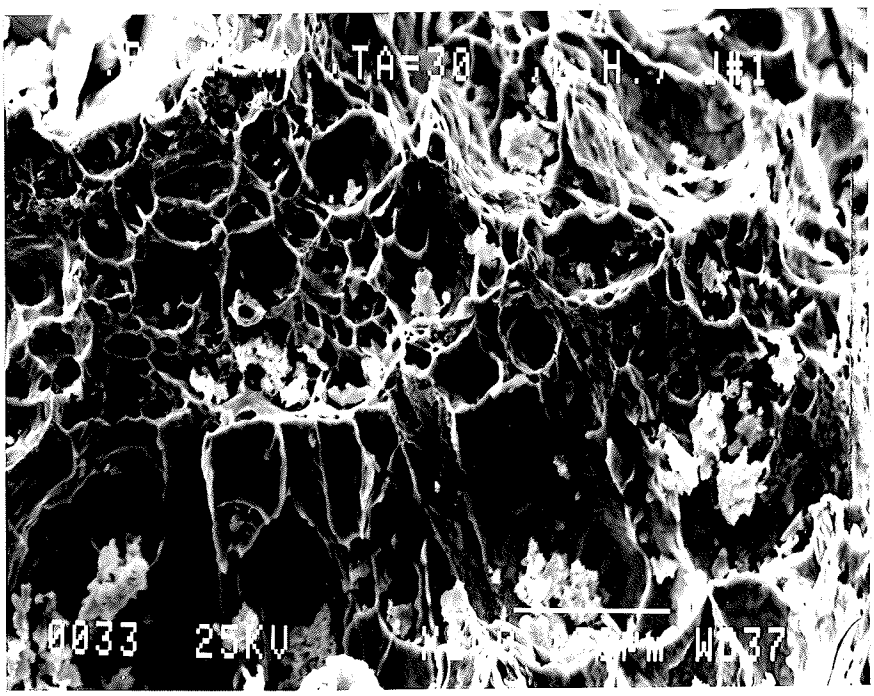

Figure 4.15(a): Fracture Surface of Three Point Specimen (Metal 1)

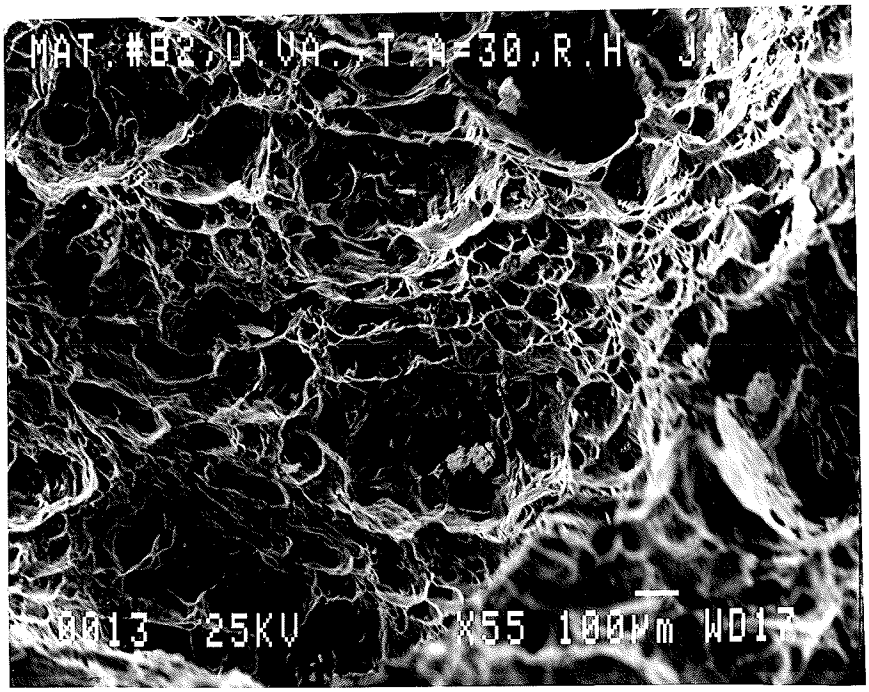

Figure 4.15(b): Fracture Surface of Three Point Specimen (Metal 2)

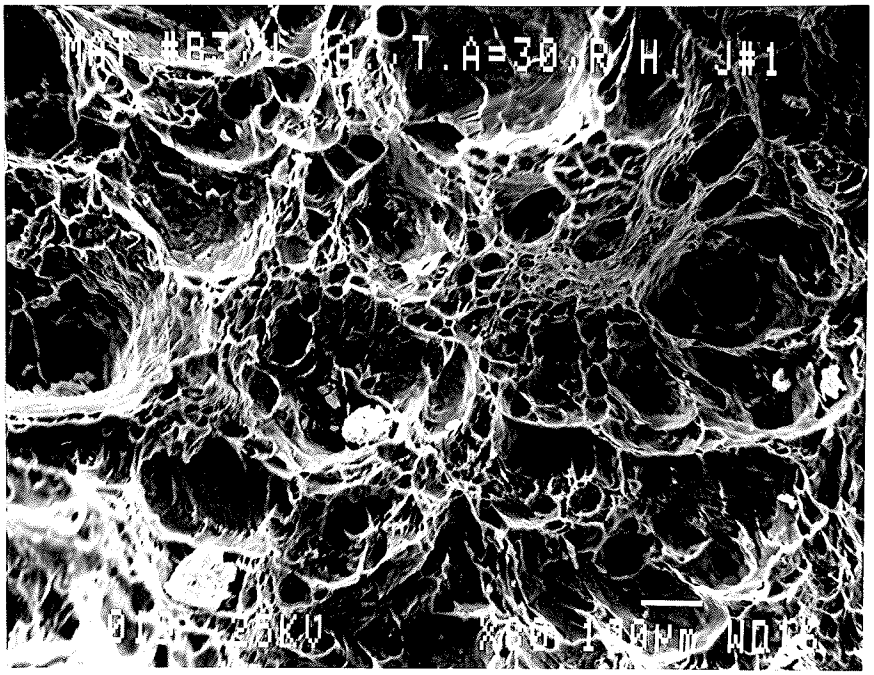

Figure 4.15(c): Fracture Surface of Three Point Specimen (Metal 3)

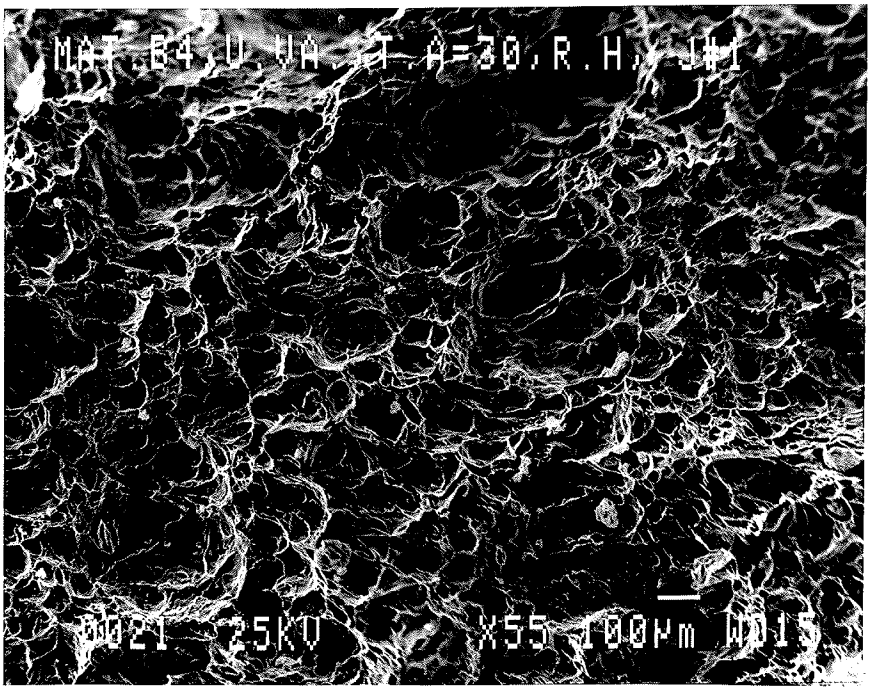

Figure 4.15(d): Fracture Surface of Three Point Specimen (Metal 4)

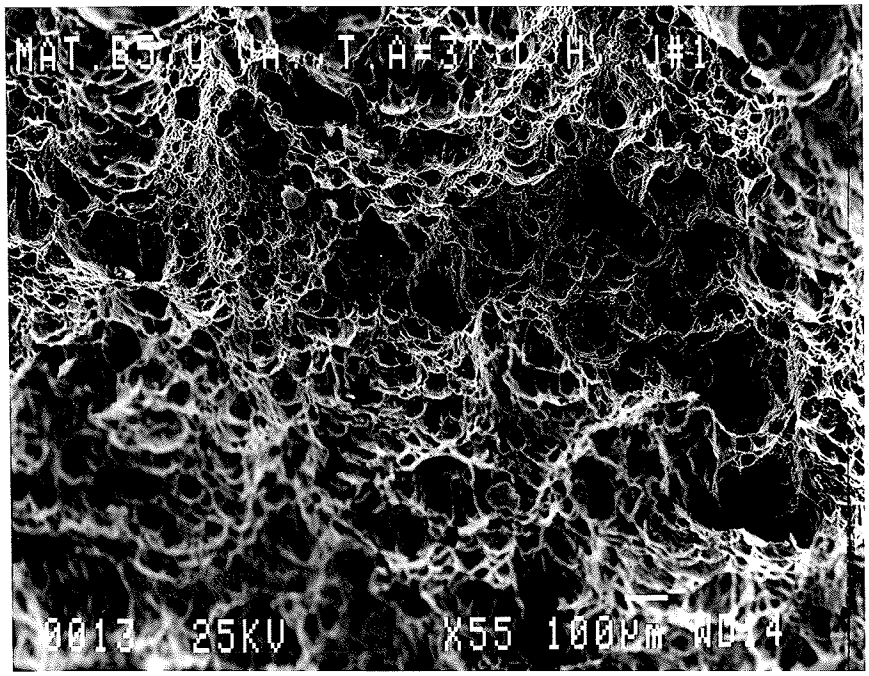

Figure 4.15(e): Fracture Surface of Three Point Specimen (Metal 5)

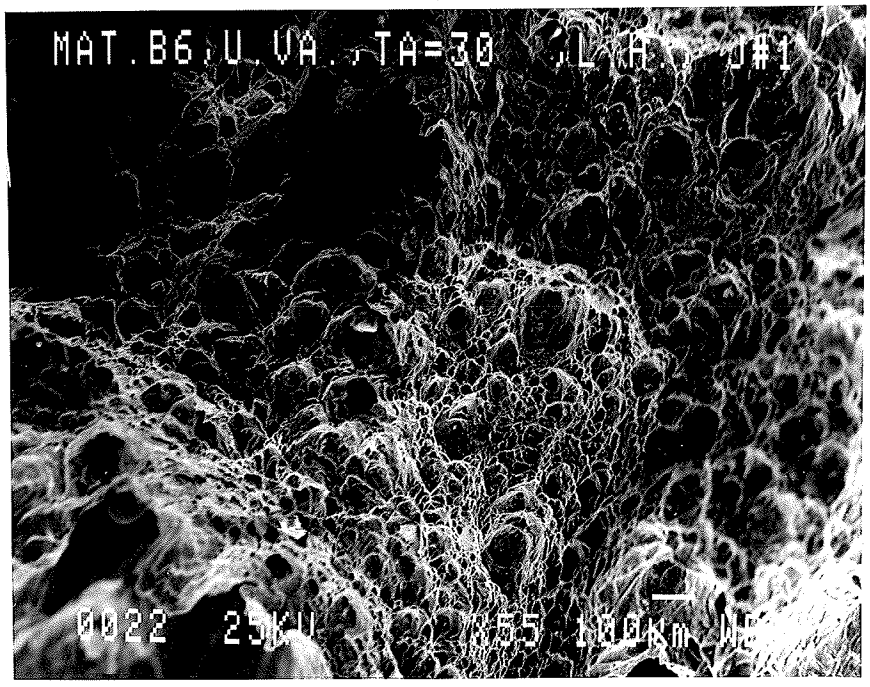

Figure 4.15(f): Fracture Surface of Three Point Specimen (Metal 6)

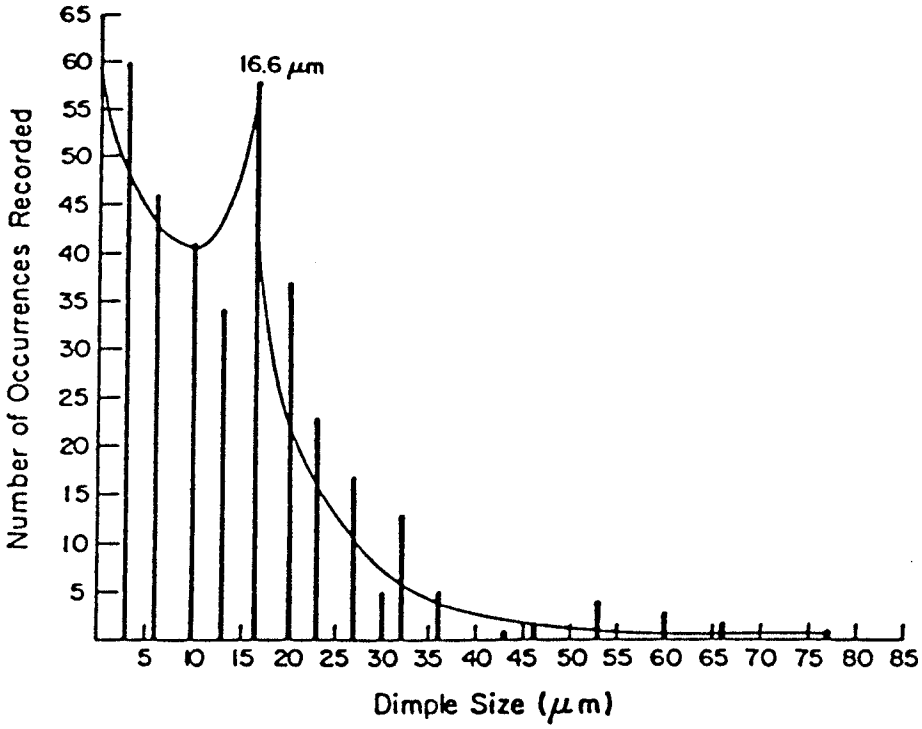

Figure 4.16(a): Void Distribution on Three Point Specimen Fracture Surface (Metal 1)

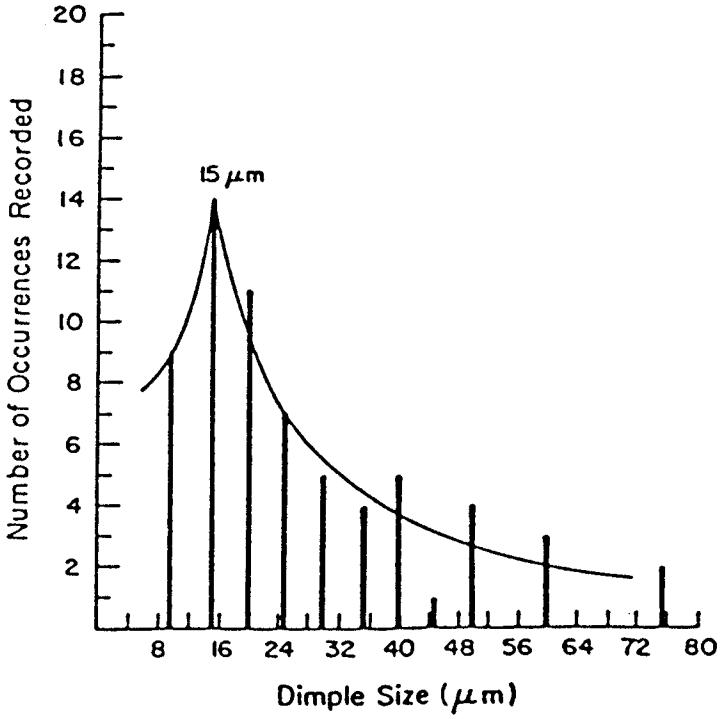

Figure 4.16(b): Void Distribution on Three Point Specimen Fracture Surface (Metal 2)

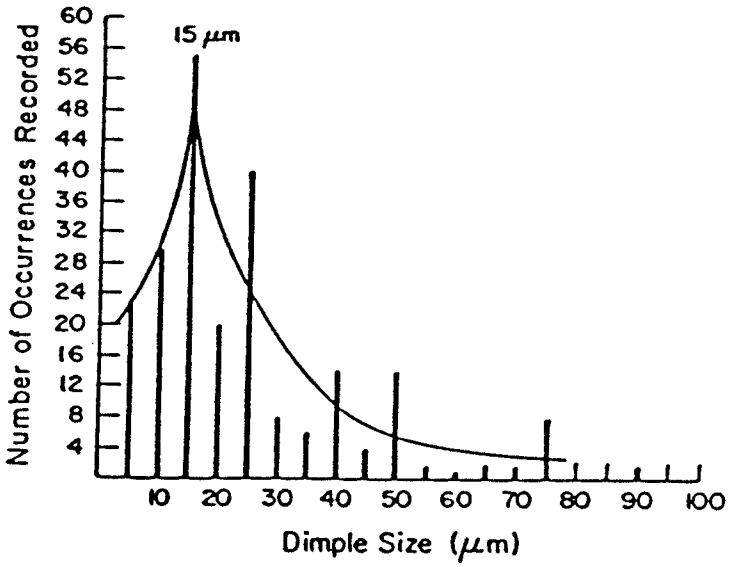

Figure 4.16c: Void Distribution on Three Point Specimen Fracture Surface (Metal 3)

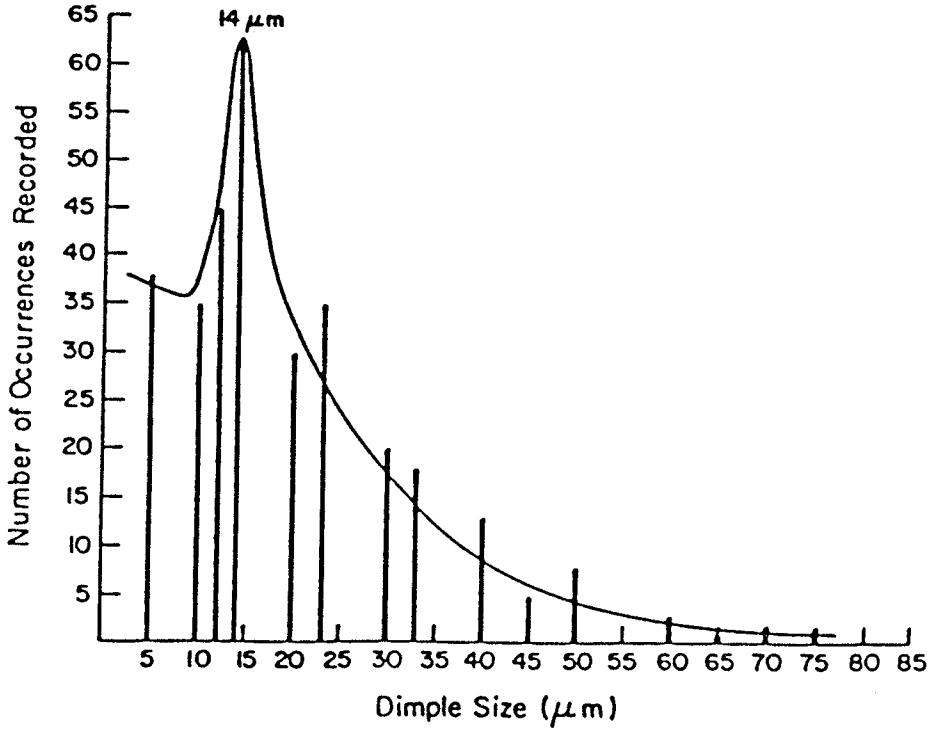

Figure 4.16d: Void Distribution on Three Point Specimen Fracture Surface (Metal 4)

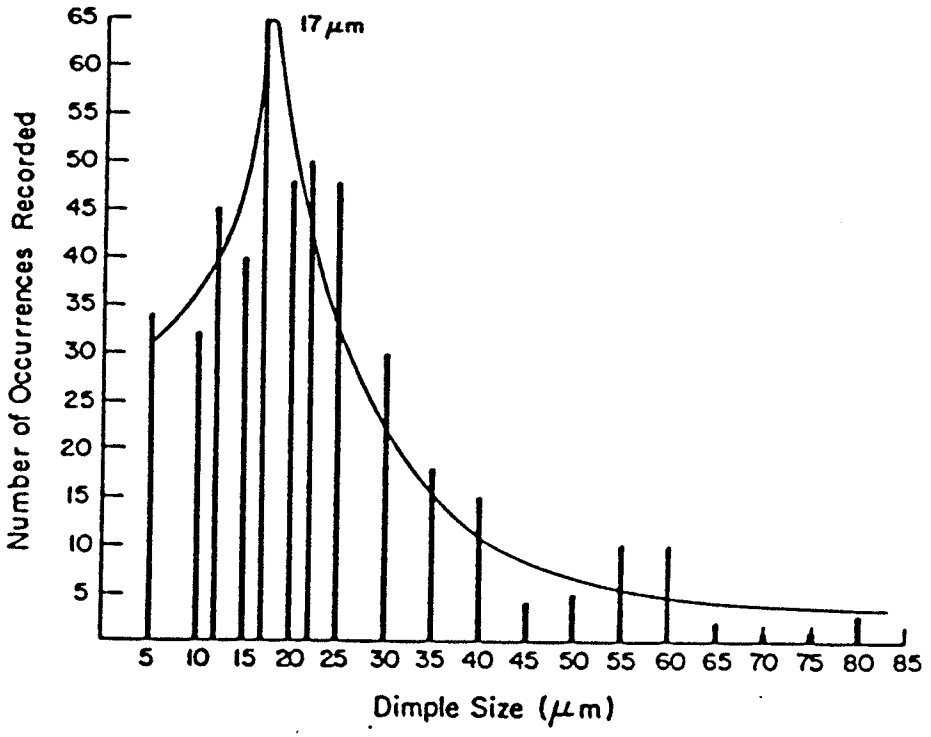

Figure 4.16e: Void Distribution on Three Point Specimen Fracture Surface (Metal 5)

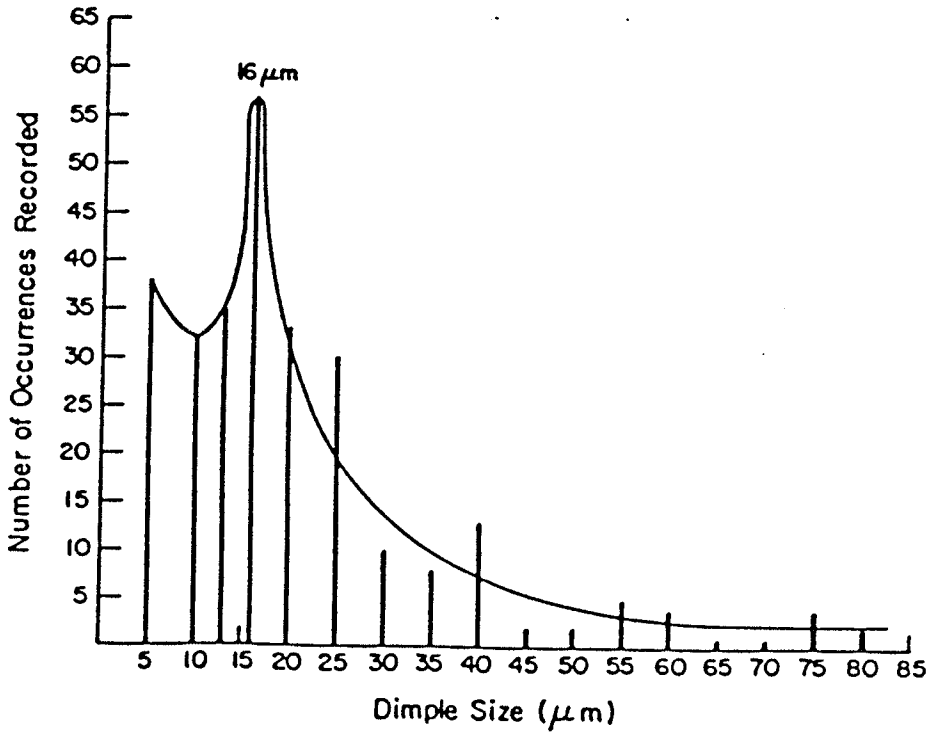

Figure 4.16f: Void Distribution on Three Point Specimen Fracture Surface (Metal 6)

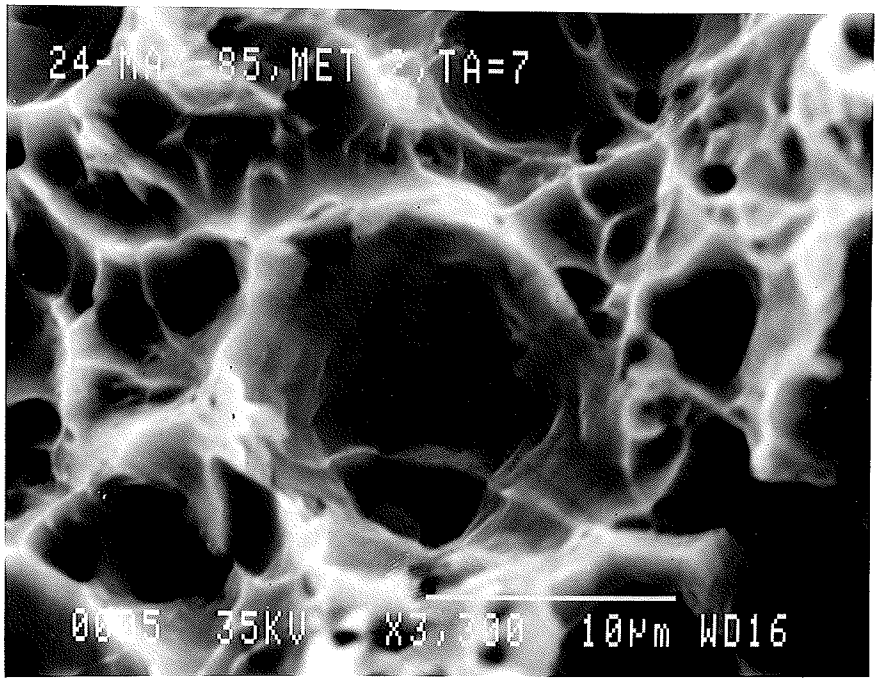

Figure 4.17: Location of Inclusions Within Voids on a Tensile Fracture Surface

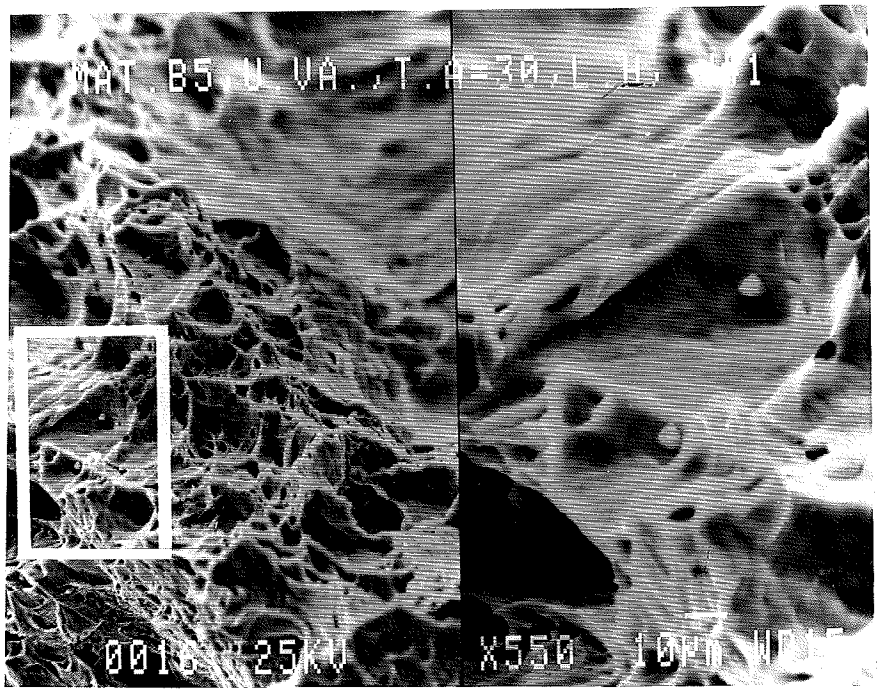

Figure 4.18: Location of Inclusions Within Voids on a Three Point Fracture Surface

4.6 X-RAY ANALYSIS OF THE HSLA STEELS

The results of a semi-quantitative energy dispersive x-ray analysis on the HSLA steel indicated that the matrix material for all the metal groups displayed a similar x-ray energy spectra. Figure 4.19(a)shows the x-ray energy profile for metal 1 matrix material as an illustration. The matrix material in the other metal groups displayed identical x-ray profiles as Figure 4.19(a). From this figure it is obvious that the microstructure is composed predominantly of iron with a concentration of manganese and silicon also being detected. This is in agreement with Table 3.1

In metal groups 1,2,4,5, and 6 the inclusions displayed x-ray energy profiles which were similar to each other. The x-ray energy spectrum of an inclusion in metal 1 is shown in Figure 4.19(b) as an illustration. It can be seen that the inclusion contains a high concentration of aluminum, sulfur, and manganese. This would suggest that the inclusions in these HSLA steels are primarily aluminum oxides or manganese sulfides. The x-ray energy profile for the inclusions in metal 3 was slightly different than for the other metal groups. Figure 4.19(c) shows the x-ray energy spectrum associated with the inclusions in metal 3. This figure indicates that the inclusions in metal 3 contain a noticable concentration of titanium which would suggest that additions of Ti directly influence the composition of inclusions in the material. It should be noted that even though each of

the six metal groups contained varying amounts of V, Ti, and Nb additions in various combinations, traces of V and Nb did not register during the x-ray analysis of the matrix material or of the inclusions in any of the metal groups.

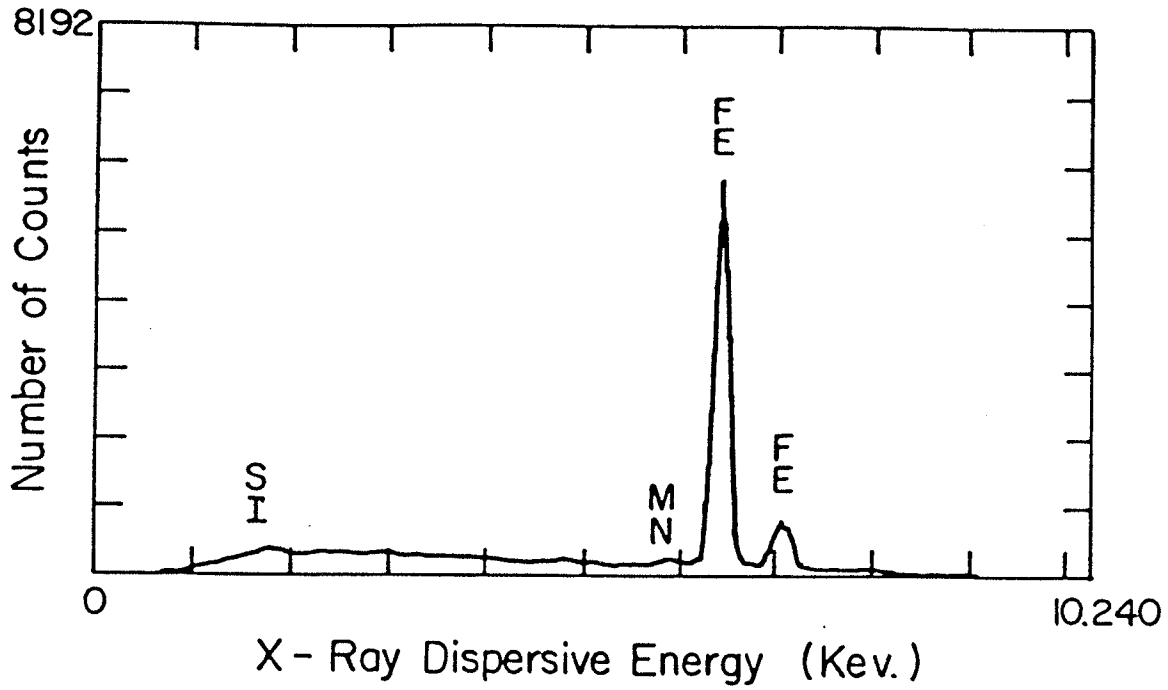

Figure 4.19(a): Energy Dispersive X-Ray Profile of Matrix Material in Metal 1

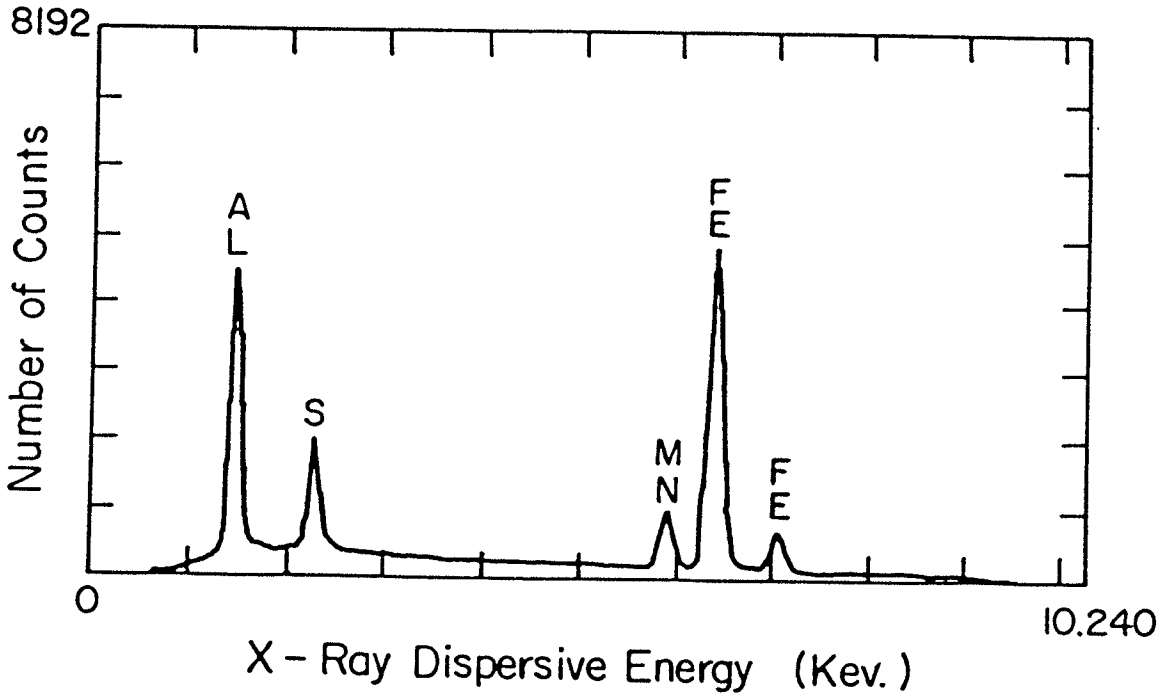

Figure 4.19(b): Energy Dispersive X-Ray Profile of an Inclusion in Metal 1

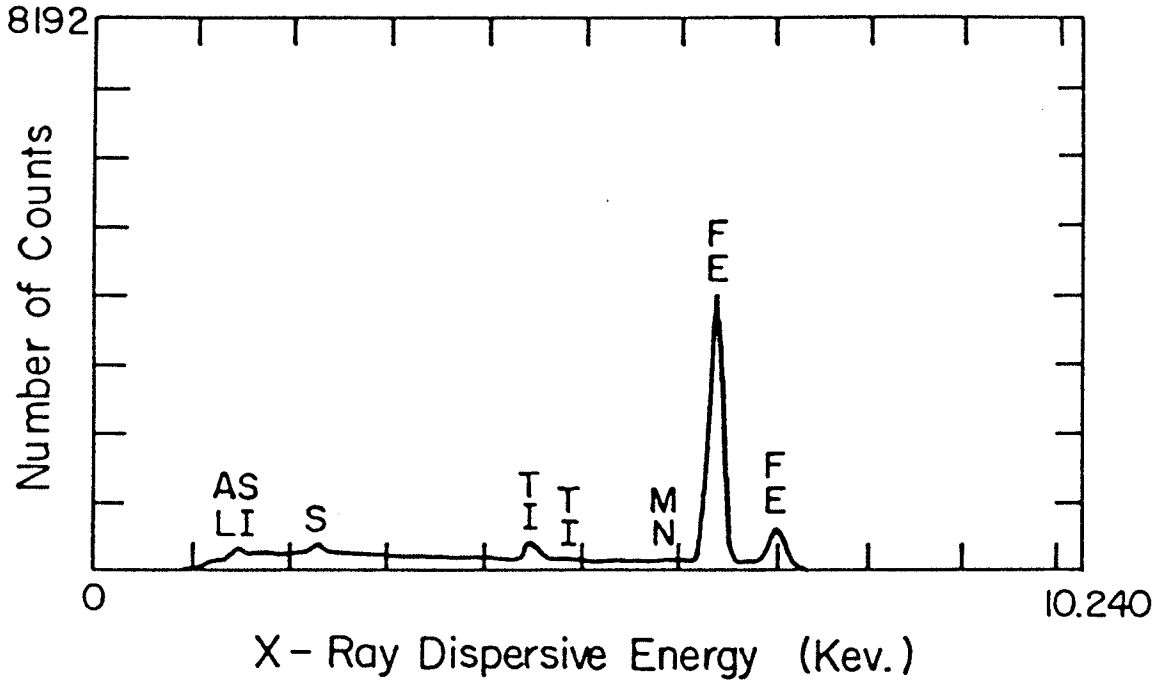

Figure 4.19(c): Energy Dispersive X-Ray Profile of an Inclusion in Metal 3

4.7 TRANSMISSION ELECTRON MICROSCOPY RESULTS

The results of the transmission electron microscopy on unstrained foils (cut from the as received steel plate) and strained foils (cut from the gage length of tensile specimens) from each metal group are presented to characterize the microstructural changes associated with the plastic deformation process of this HSLA steel.

Figure 4.20(a to f) illustrates the microstructure of the undeformed ferrite matrix for each metal group. It should be noted in these micrographs that there is a lack of dislocations within the grains and at the grain boundaries. These micrographs show distributions of precipitates through out the matrix as indicated most clearly in Figures 4.20(a and f).

Foils cut from various locations along the gage length of a tensile specimen of metal 6, as illustrated in Table 3.3 , were used to observe the development of dislocation structures during plastic deformation. Table 3.3 indicates that these foils were strained over a range of strains corresponding to reductions in area of 48.3% (foil 1) to reductions in area of 10.2% (foil 5). The growth and development of dislocation structures with increased strain for these five foils is shown in Figure 4.21(a to e). The increased dislocation density with increased strain is clearly shown in these micrographs. Significant microstructural features

characteristic of the deformation process are highlighted with arrows in Figures 4.21(a and e). The appearance of individual dislocations throughout the material microstructure at low local strains is illustrated by an arrow in Figure 4.21(a). The occurrence of dislocation structures extending across grain boundaries in highly strained material is indicated by an arrow in Figure 4.21(b). Table 4.2 shows the average dislocation structure size, obtained from Figure 4.21(a to e) using a line intercept method.

The microstructure of plastically deformed matrix material taken from foils near the tensile fracture surfaces for each metal group (Table 3.2) are shown in Figure 4.22(a to f). these micrographs indicate that all the metal groups displayed similar microstructural changes during plastic straining. These changes consisted primarily of the development of dislocation structures within the ferrite matrix and, in some cases, along grain boundaries, as illustrated in Figure 4.22(a to f) as well as Figure 4.21(a to e). The average dislocation structure size, measured from numerous micrographs from each metal group, are shown in Table 4.3 along with the corresponding local percentage reduction in area.

The variation in dislocation network spacing with increased strain (reduction in area) for metal 6 is shown in Figure 4.23. Figure 4.23 is a graphical representation of the data points found in Table 4.2. In this figure it is

obvious that the dislocation structure spacing decreases sharply with increased reduction in area until approximately 20% local reduction in area is achieved. Straining greater than RA=20% does not lead to a further decrease in dislocation structure size in this material. Data points from Table 4.3 representing dislocation structure spacings and corresponding reductions in areas from all the metal groups are presented along with data points from Table 4.2 in Figure 4.24. The fact that the data points from Table 4.3 fall on the same curve in Figure 4.24 as do the data points from Table 4.2 would indicate that a similar process of deformation and work hardening occurs in all the metal groups during straining.

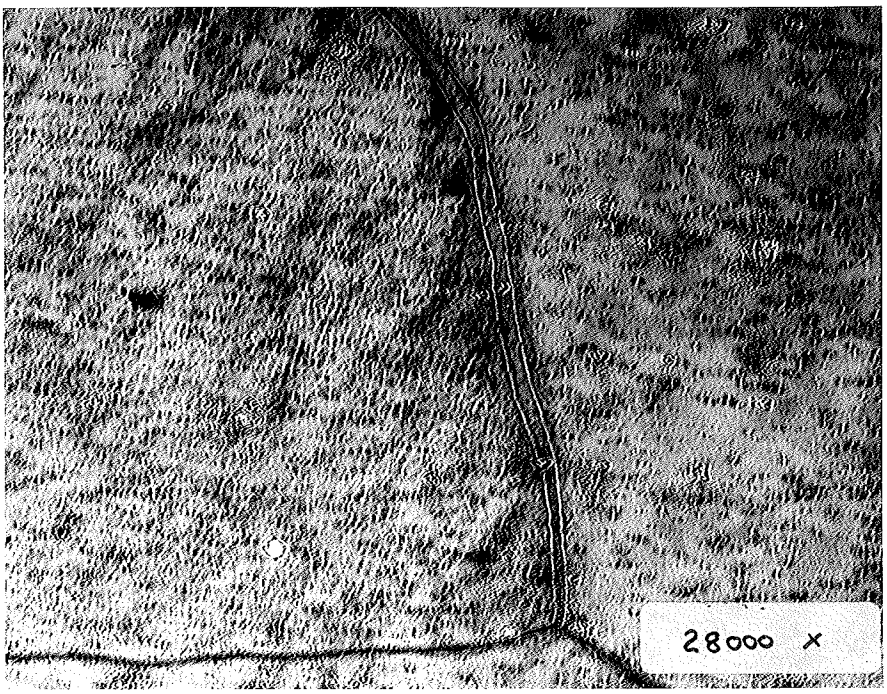

Figure 4.20(a): Unstrained Microstructure in Metal 1

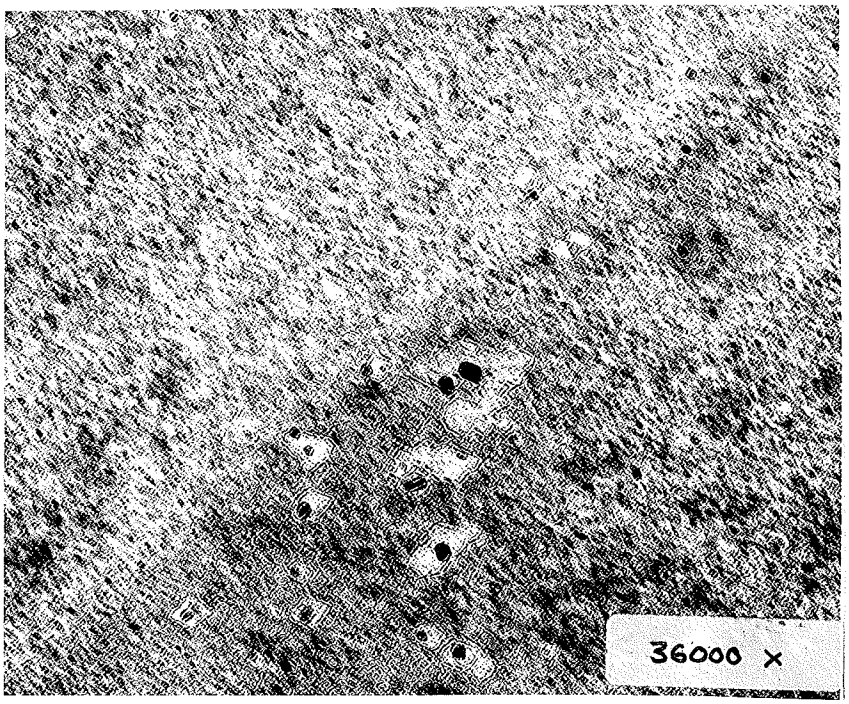

Figure 4.20(b): Unstrained Microstructure in Metal 2

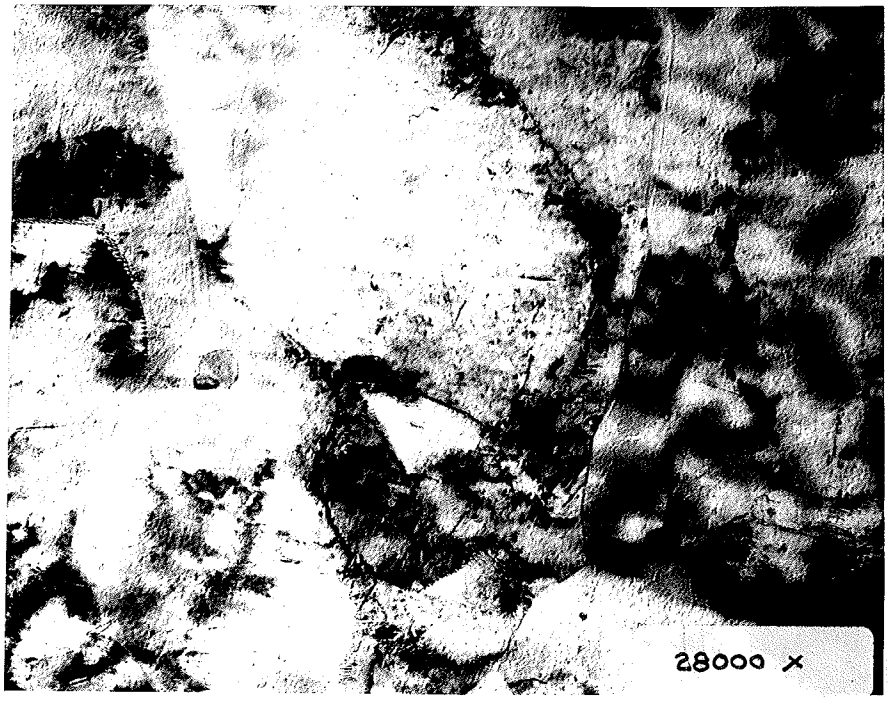

Figure 4.20(c): Unstrained Microstructure in Metal 3

Figure 4.20(d): Unstrained Microstructure in Metal 4

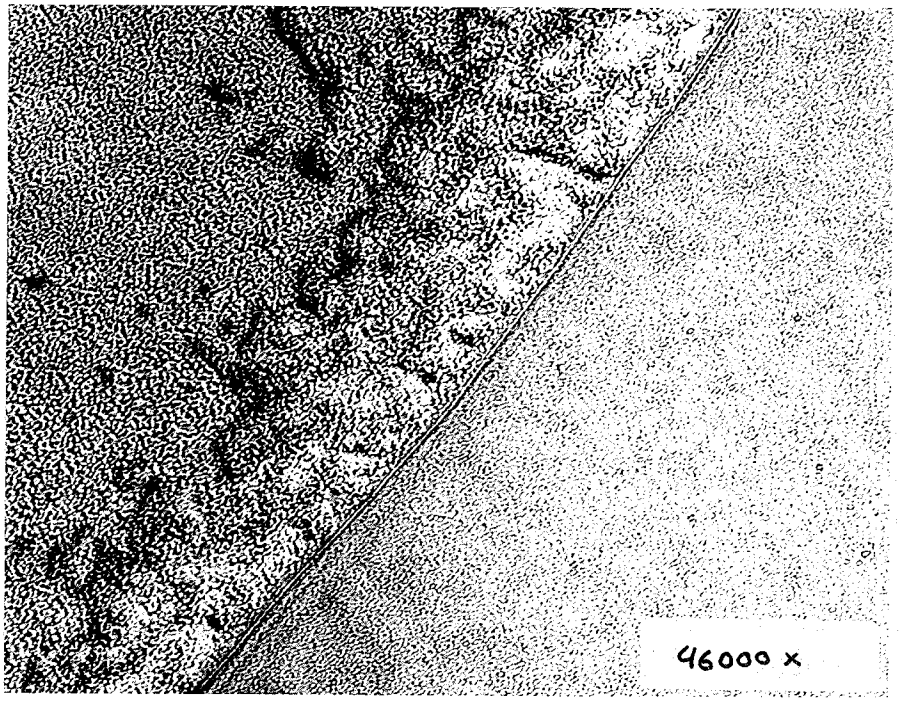

Figure 4.20(e): Unstrained Microstructure in Metal 5

Figure 4.20(f): Unstrained Microstructure in Metal 6

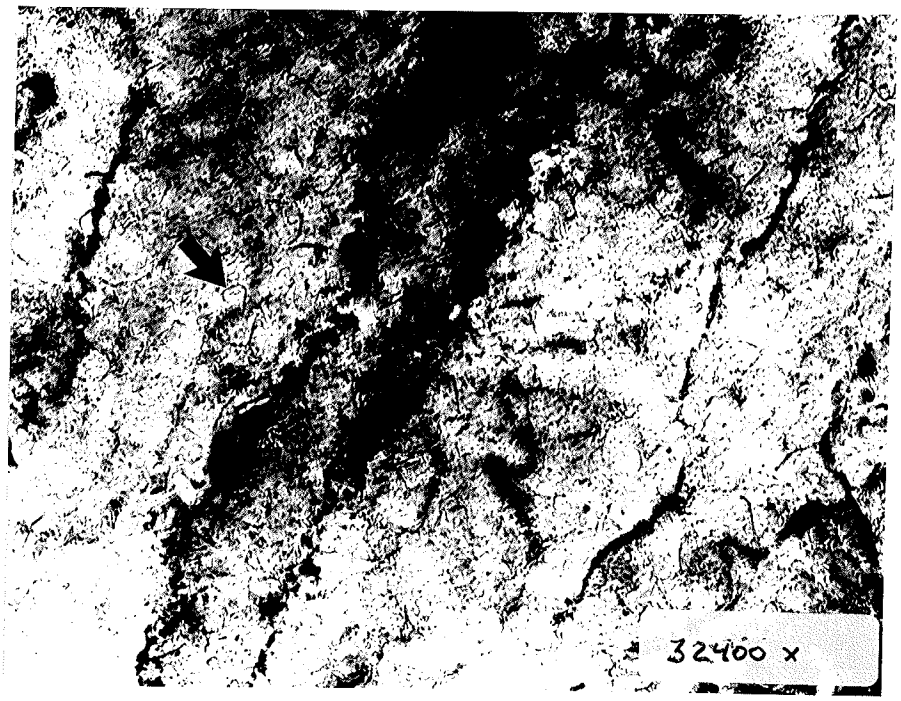

Figure 4.21(a): Dislocation Structures Resulting From a 10.2% Reduction in Area (Metal 6)

Figure 4.21(b): Dislocation Structures Resulting From a 13.5% Reduction in Area (Metal 6)

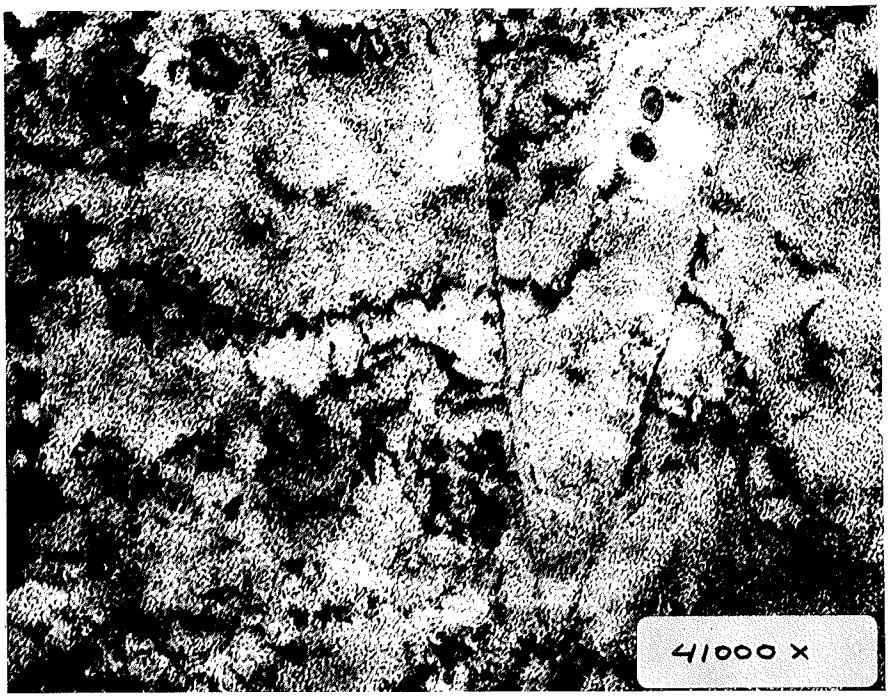

Figure 4.21(c): Dislocation Structures Resulting From a 16.7% Reduction in Area (Metal 6)

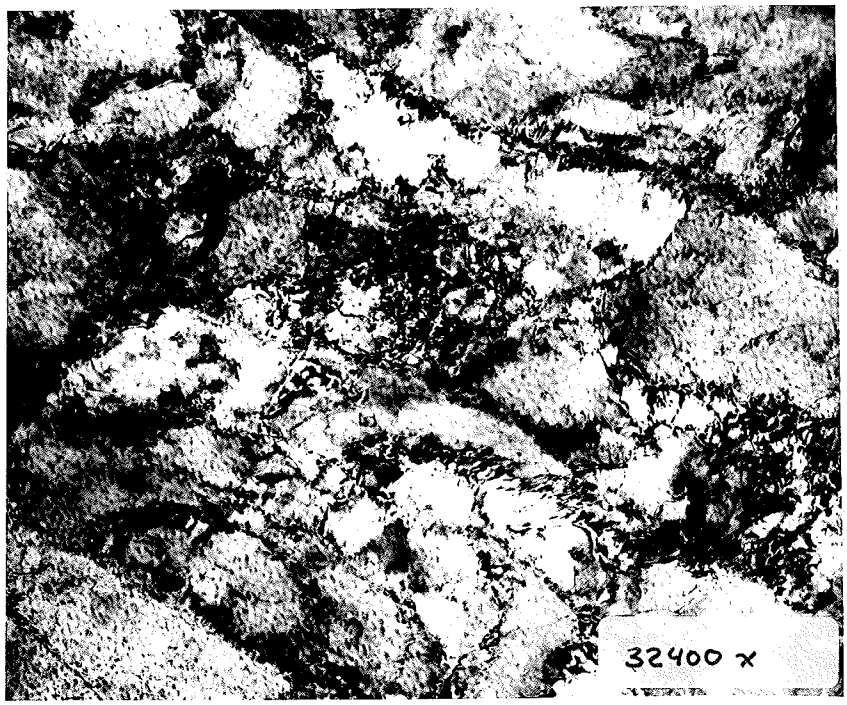

Figure 4.21(d): Dislocation Structures Resulting From a 26.1% Reduction in Area (Metal 6)

Figure 4.21(e): Dislocation Structures Resulting From a 48.3% Reduction in Area (Metal 6)

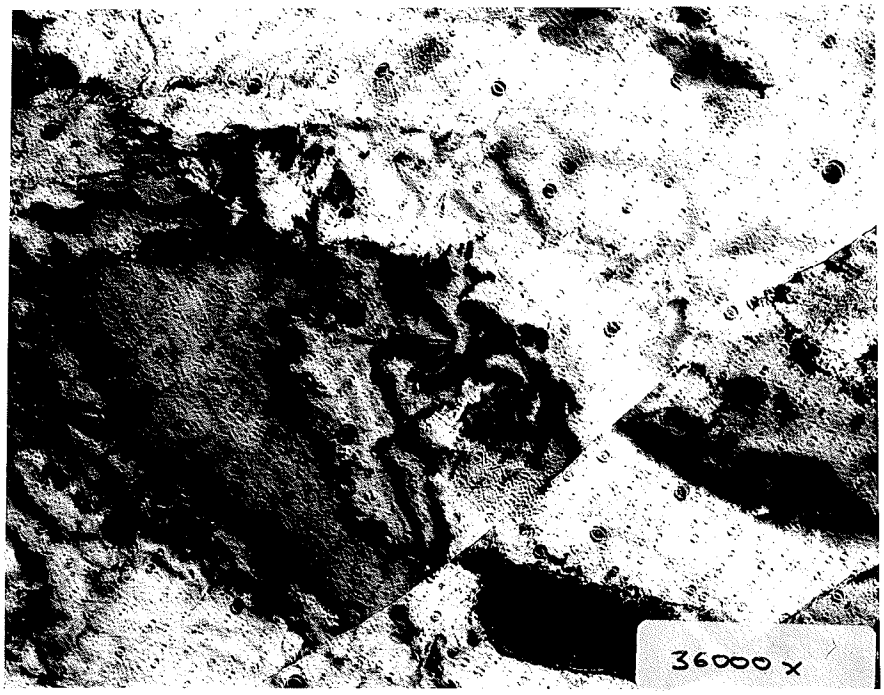

Figure 4.22(a): Dislocation Structures in Metal 1 RA=39.0%

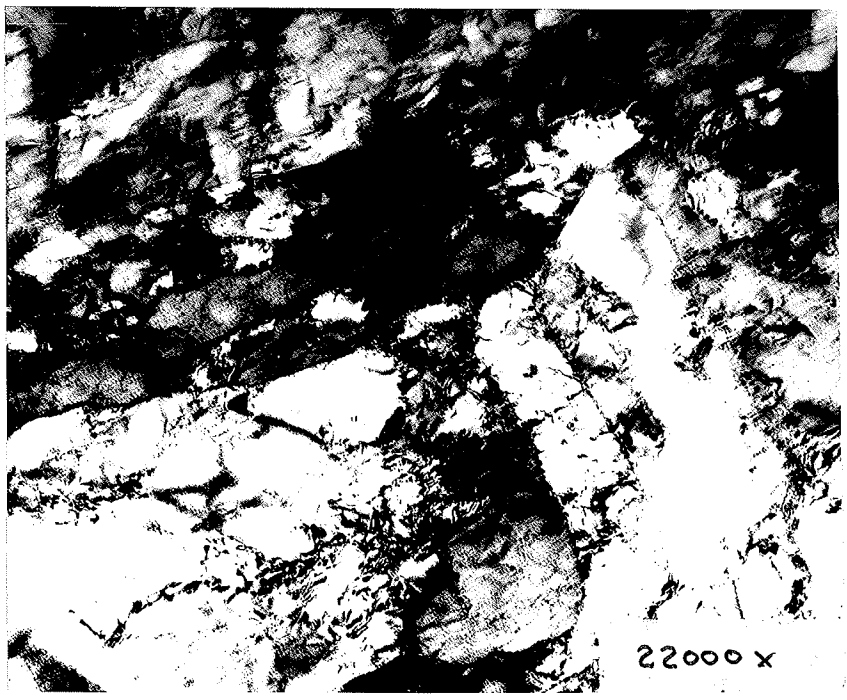

Figure 4.22(b): Dislocation Structures in Metal 2 RA=31.8%

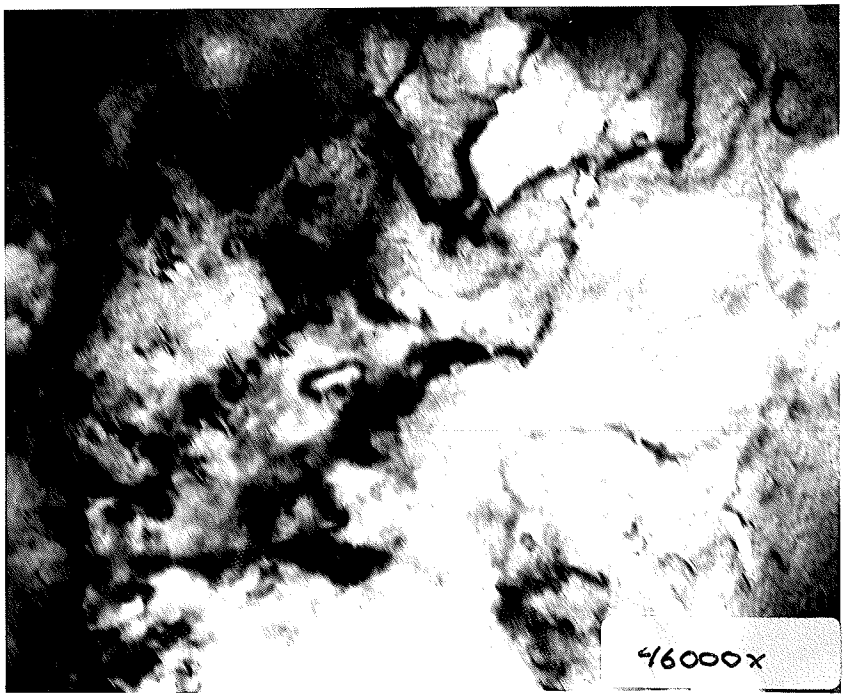

Figure 4.22(c): Dislocation Structures in Metal 3 RA=35.0%

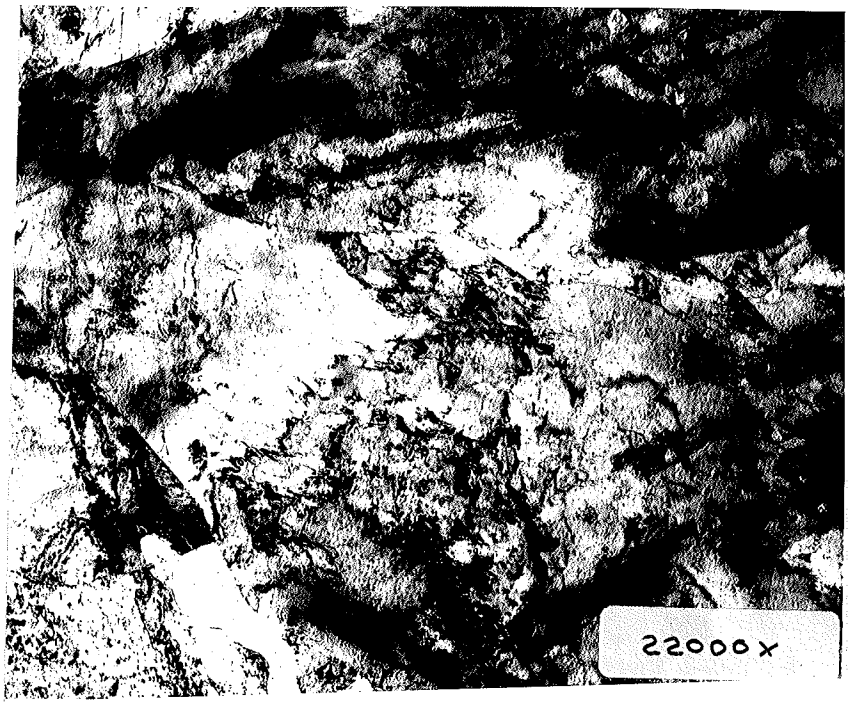

Figure 4.22(d): Dislocation Structures in Metal 4 RA=42.0%

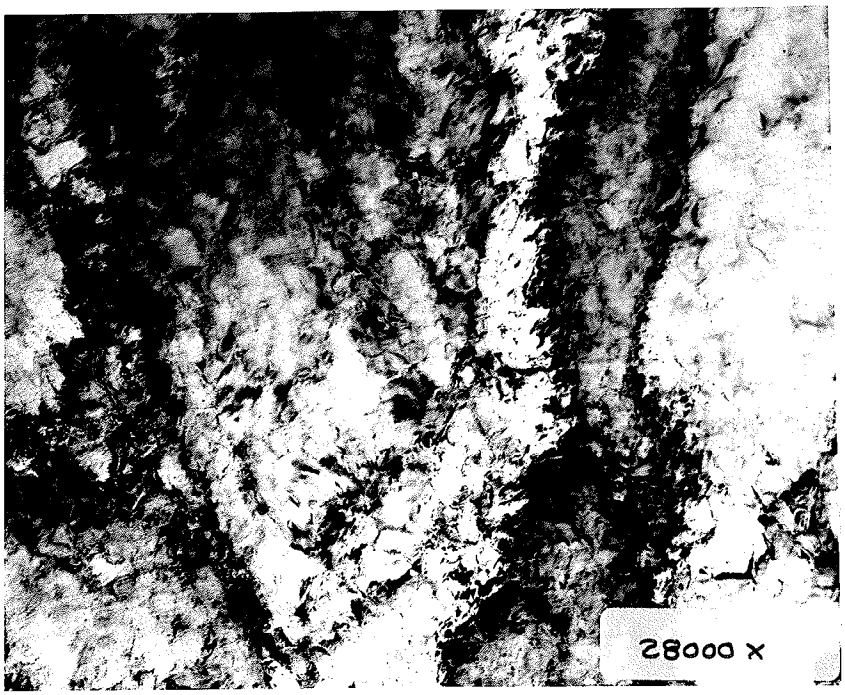

Figure 4.22(e): Dislocation Structures in Metal 5 RA=47.0%

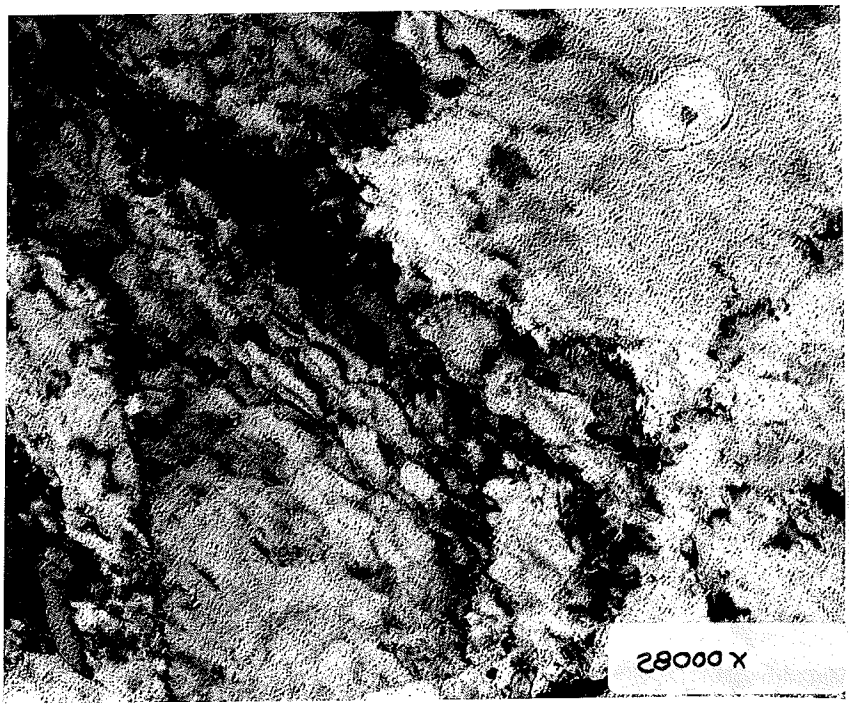

Figure 4.22(f): Dislocation Structures in Metal 6 RA=37.0%

TABLE 4.2

Dislocation Cell Size for Various Local Reductions in Area (Metal 6)

Foil Number	Local Reduction in Area (%)	Average Dislocation Cell Size (Å)
1	48.3	4211
2	26.1	3968
3	16.7	5802
4	13.5	5661
5	10.2	10185

TABLE 4.3

Dislocation Cell Size for Strained Foils from Each Metal Group

Metal Group	Local Reduction in Area (%)	Average Dislocation Cell Size (Å)
1	39.0	3361
2	31.8	3900
3	35.0	3400
4	42.0	3200
5	47.0	4100
6	37.0	4000

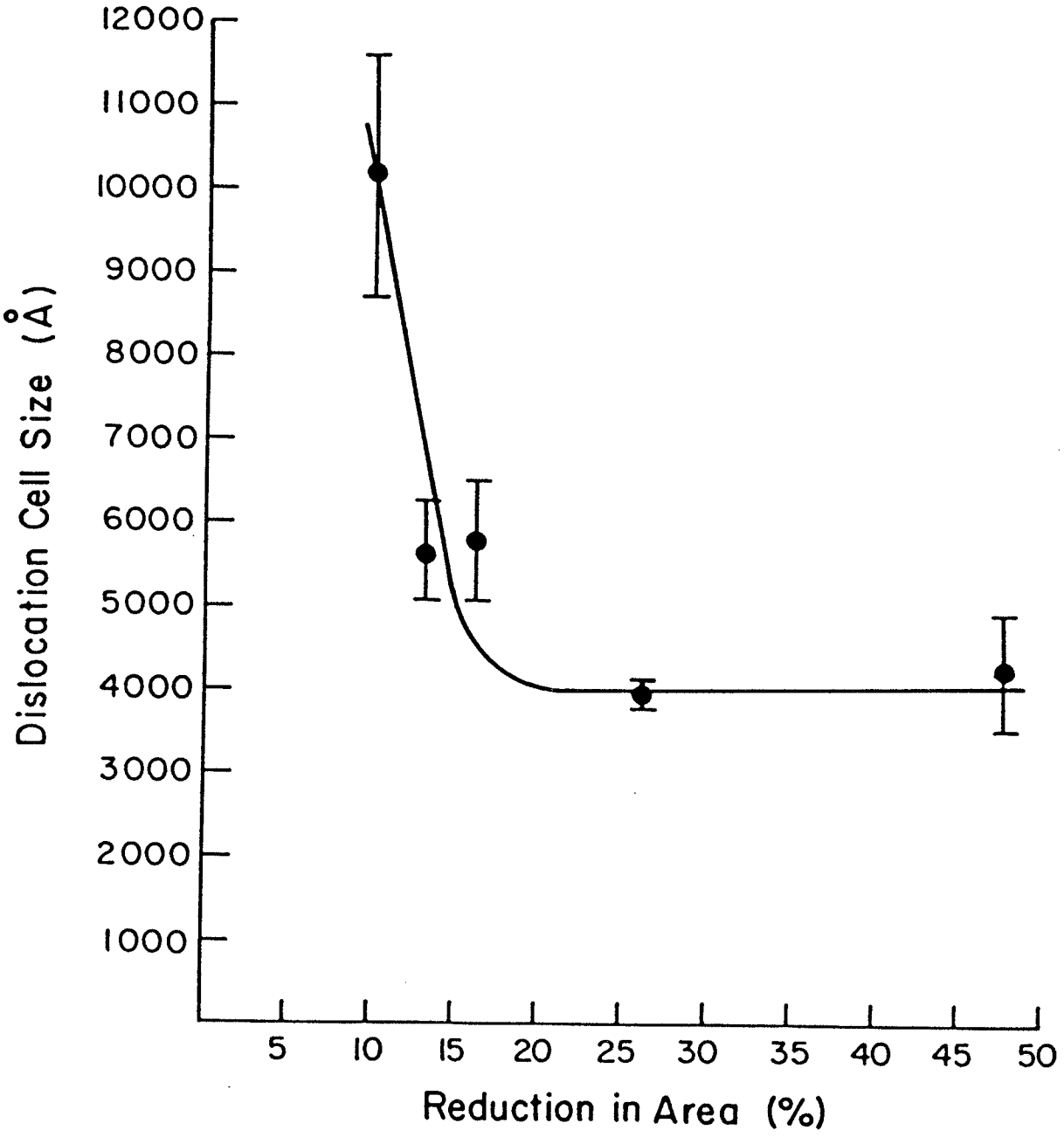

Figure 4.23: Dislocation Structure Spacing Versus Local Reduction in Area (Metal 6)

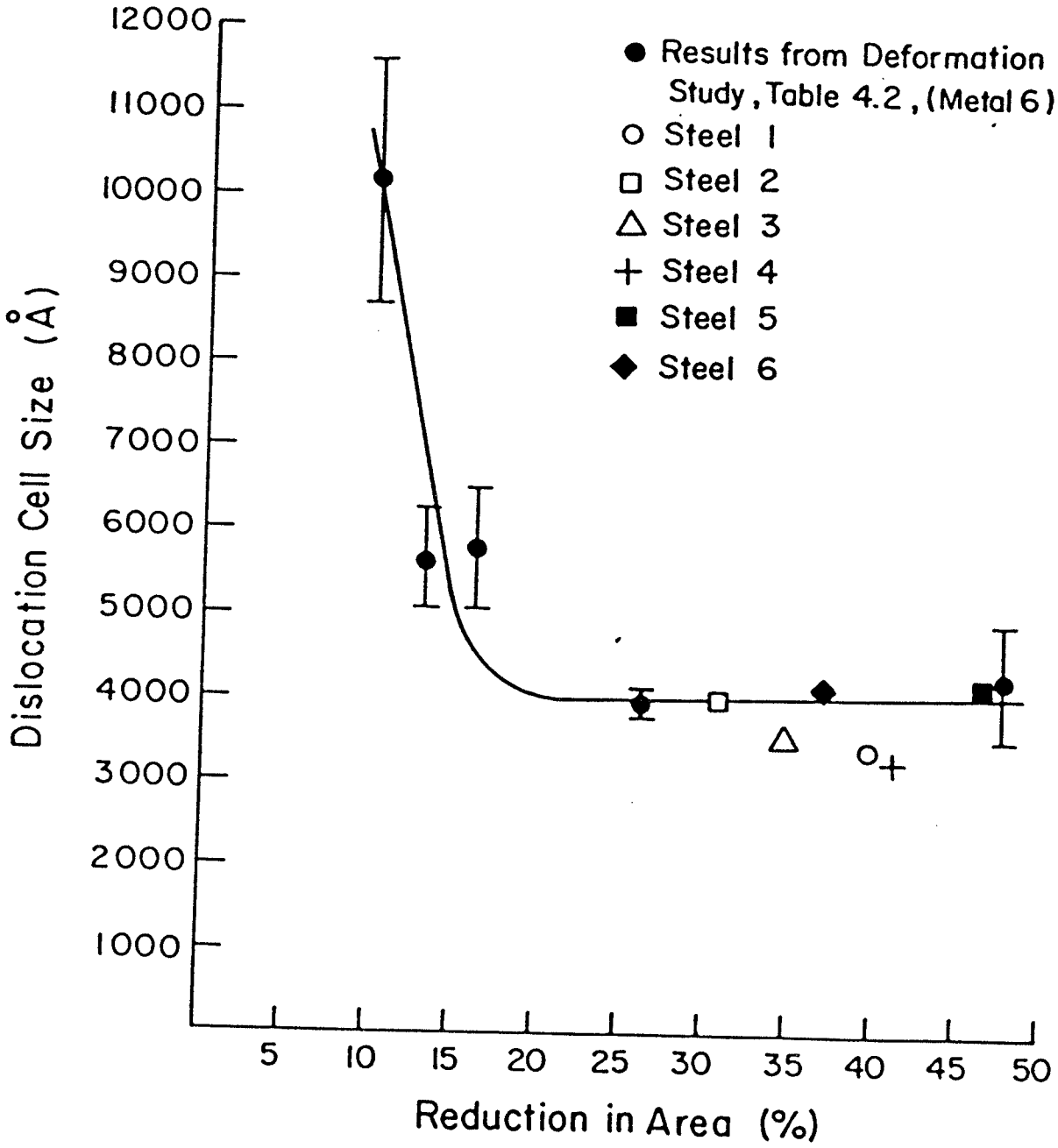

Figure 4.24: Dislocation Structure Spacing Versus Local Reduction in Area (Including All Data Points From Tables 4.2 and 4.3)

Chapter V

DISCUSSION

The experimental procedures described in chapter 3 were performed in order to characterize the ductile fracture process in ductile materials such as HSLA steels both from a macroscopic as well as a microstructural viewpoint.

The experimental results presented in chapter 4 reflect this intention and can be placed into three general categories. The first category is the results obtained from macroscopic material testing. These tests consist of standard tensile tests and J_{IC} fracture toughness tests. The results of these tests give an indication of the mechanical properties, such as tensile strength, ductility, and fracture toughness, of large specimens of these HSLA steels. The variations in these mechanical properties from one metal group to another are recorded.

The second category of experimental results focuses on characterizing the microstructure of the material. This is done by optical microscopy using computerized image analysis to determine the grain size as well as the inclusion distribution and size for all the metal groups. Combining these two categories allows correlations to be made between changes in mechanical properties (tensile strength and fracture toughness) and microstructural material changes.

The third category of experimental results deals with changes in the material microstructure resulting from plastic deformation. These are the experimental results obtained from the electron microscopy (TEM and SEM). The results from this section enable the process of plastic deformation (resulting from tensile straining) in polycrystalline steel to be discussed. The micrographs from both TEM and SEM illustrate the role that microstructural features such as grain boundaries, small precipitates and inclusions play in plastic deformation and in the fracture process in general.

By combining the results obtained regarding the effect of microstructural changes on ductile fracture toughness with results concerning the role of microstructural features on plastic deformation, a unified description of the ductile fracture process is achieved. The result is a quantitative description of the ductile fracture in HSLA steels in terms of its most fundamental constituent, the behaviour of dislocations during plastic deformation.

5.1 THE PROCESS OF DUCTILE FRACTURE IN HSLA STEELS

The following section will discuss the contributions that several macroscopic material and physical parameters, such as precipitates and local stress conditions, have on the ductile fracture process in structural steels. Also the microstructural changes occurring during tensile straining

will be discussed to evaluate the mechanisms involved in the plastic deformation of ferritic structural steels prior to fracture.

5.1.1 Role of Dislocation Cells in the Fracture Process

The ability for the material to absorb energy by plastic deformation is a primary requirement for good fracture toughness. Plastic deformation occurs throughout the fracture process and contributes to all aspects of void initiation, growth as well as coalescence. Expressions relating macroscopic fracture toughness parameters (such as J_{Ic}) to COD (equation 2.4) or to critical stretch zone widths (equation 2.5) demonstrate the effect of plastic deformation on fracture toughness.

In this present study, the microstructures of the HSLA steels under investigation contain a ferrite-pearlite combination with primarily polygonal ferrite grains (Figure 4.1(a to f)). As a result, the way that dislocations are generated, move, and ultimately accumulate within this ferrite matrix during plastic deformation will influence the ductile fracture toughness of the steels.

5.1.1.1 Dislocation Cell Development With Increasing Strain

The development of dislocations with increased tensile straining is illustrated in the TEM micrographs of Figure

4.21(a to e) where five foils were cut from a single tensile specimen (metal 6) at various distances from the fracture surface as shown in Table 3.3. From Figure 4.21(a) it can be seen that at low strains, corresponding to a local reduction in area of 10.2%, large dislocation structures are beginning to form. These structures contain a high dislocation density compared to the surrounding matrix. Also of note is that the ferrite matrix region surrounding these structures contains long bowed individual dislocations (as indicated by arrows in Figure 4.21(a)). The presence of these dislocations within the matrix indicates that dislocations appear to be generated uniformly throughout the matrix with straining. The fact that certain regions of the ferrite matrix surrounding the dislocation structures remains virtually dislocation free even after considerable tensile straining (Figure 4.21(d and e)) indicates that dislocations generated within the matrix glide into dislocation cell walls. The distance that these dislocations glide can be considerable as is witnessed by dislocation free regions between dislocation structures (dislocation cell diameter) extending for distances greater than 10000 Å as shown in Figure 4.21(a) and Table 3.3. The bowed nature of the individual dislocations within the matrix in Figure 4.21 could suggest interaction or generation of dislocations at sites of small precipitates within the matrix.

Figure 4.21(b and c) indicate the increased dislocation density with increased tensile straining corresponding to reductions in area of 13.5% and 16.7% respectively. These figures also indicate that dislocation structures form both at grain boundaries as well as within the grains. The increasing strain results in dislocation cell walls of increased thickness and dislocation density. Figure 4.21(a to e) also show that with increased strain the dislocation structures develop branches and begin to interconnect. The connecting of the dislocation structures results in decreased cell diameter with increased strain as is shown in Table 3.3.

Figure 4.21(e) shows the severe dislocation density resulting from massive plastic deformation associated with large scale reductions in area (RA=48%). A significant feature of this figure is that dislocation structures are shown beginning to extend across grain boundaries (as indicated by arrows). The strain at which these dislocations overcome the restraining influence of the grain boundaries corresponds to the initiation of general yielding in a ductile material. Dislocation structures were not observed extending across grain boundaries in foils with reductions in area less than 26.1% (Figures 4.21(a to d)). Transgranular dislocation motion is, however, observed at reductions in area of 48% (Figure 4.21(e)). This would indicate the high strength of the grain boundary in resisting dislocation

glide is an important feature when discussing the ability of a material to absorb maximum energy by plastic deformation. From a microstructural level, the strength of the particular grain boundaries can be seen by the way large dislocation structures are restrained behind them in Figure 4.21(e). The strength of grain boundaries in resisting dislocation motion can be evaluated quantitatively by an expression similar to the Petch equation [4] where the strength of the grain boundary, τ^*, is expressed as a summation of the individual stresses, τ, exerted by n dislocations piled up behind it, or

$$\tau^* = N\tau \qquad (5.1)$$

The discussion of dislocation development during tensile straining has been strictly qualitative. A more quantitative expression of the plastic deformation process can be obtained by plotting dislocation cell diameter versus local reduction in area as in Figure 4.23. Figure 4.23 indicates that the variation in dislocation cell size with strain can be divided into two distinct stages. Stage I occurs at low strain levels and represents the region where the dislocation cell diameter decreases sharply with increasing strain. In this region the material is able to absorb considerable energy by plastic deformation. This deformation occurs both by the development of dislocation structures within the matrix and at grain boundaries. With increasing strain these

dislocation cell walls become wider and branch out resulting in decreased mean dislocation cell diameter as shown in Figure 4.21(a to e) and is illustrated in Figure 4.23. Figure 4.23 indicates that when the applied strain reaches a certain value the dislocation cell size remains constant (in this material approximately 4000 Å) with increasing strain. The strain corresponding to a local reduction in area of approximately 17% indicates, for this material, the critical strain beyond which the dislocation network size no longer decreases. This critical strain delineates the onset of stage II of the deformation process.

Stage II represents the deformation of the material at high strains and correspondingly high dislocation densities. The characteristic feature of stage II deformation is that the dislocation structure size is independant of strain as shown in Figure 4.23. Figure 4.21(e) illustrates the microstructure characteristic of stage II deformation which displays considerable dislocation extension across the grain boundaries. This, combined with the fact that transgranular dislocation movement was not observed at reductions in area of less than 26.1% (Figures 4.21(a to d)), would suggest that stage II deformation is characterized by the onset of large scale dislocation movement across the grain boundaries. This suggests that the critical transition strain between stage I and stage II in Figure 4.23 is controlled, at least to a large part by the strength of the grain bound-

aries for resisting dislocation movement. Since most of the energy absorbed during plastic deformation occurs during stage I, when the grain boundaries are still blocking dislocation movement, it is advantageous to increase the critical transition strain as much as possible to maximize the energy absorbed prior to fracture. This could theoretically be accomplished by decreasing the grain size and hence increasing the grain boundary density of the material.

5.1.1.2 Dislocation Cell Sizes in Deformed HSLA Steel

Comparison between the strained microstructures of the six metal groups, Figure 4.22(a to f) , suggests that the effect of straining is similar on the microstructures in all the metal groups. Table 4.3 indicates the local reduction in area and corresponding dislocation network spacings for the foils shown in Figure 4.22(a to f). Figure 4.24 shows that the dislocation structure spacing of Table 4.3 correspond well with the trend shown in Figure 4.23. From these results it is therefore reasonable to conclude that plastic deformation has occurred by the same process in all the metal groups analyzed. That is, material properties such as precipitation density and distribution did not affect the mechanism of dislocation movement or arrangement differently in one material compared to another. This is further substantiated by the macroscopic tensile results in Table 4.1 which indicate that the ductility, as illustrated by the

percentage of elongation, fracture strain, reduction in area, and the strain hardening exponent did not vary significantly from one metal group to another.

5.1.2 The Role of Second Phase Particles on the Fracture Process

5.1.2.1 Small Precipitates

The TEM micrographs of the unstrained microstructures of the six metal groups in Figure 4.20(a to f) show that small precipitates are present in all the metal groups. These particles range in size from 100 Å to 400 Å. The role of these particles as strengthening agents is evident by the high values of ultimate tensile strength and yield strength for all the metals, as illustrated in Table 4.1. This is attributed to the impeding of dislocation movement achieved by a distribution of precipitates throughout the matrix [75].

The precipitation of these particles at elevated temperatures cause pinning of the grains and slowing of the high temperature recrystallization and grain growth during the controlled rolling This results in a refined grain structure upon cooling. The resulting improvements in grain size for metals 3 to 6 can be seen in Figure 4.2. The resulting grain refinement also produces better fracture resistance since more grain boundaries necessitate more external stress to be applied to produce large scale dislocation movement (stage II deformation).

The role of small precipitates in these HSLA steels can be summarized as a combination of precipitation strengthening and grain refinement. The precipitation strengthening results from an even distribution of precipitates across the matrix inhibiting easy dislocation glide . The grain refinement results from the distribution of precipitates along grain boundaries. The resulting grain refinement improves both the tensile and fracture properties by impeding dislocation motion across the material as has been discussed in sections 5.1.1.1 and 2.3.1.

5.1.2.2 Nonmetallic Inclusions

Figures 4.3(a to f) show the size and distribution of nonmetallic inclusions found in the various metal groups. The mean diameter of these inclusions and their volume fractions are shown in Figures 4.4 and 4.5 respectively. These inclusions have a direct influence on the fracture process by acting as sites for preferential void initiation. This is supported by the SEM analysis performed on fracture surfaces of both tensile and precracked specimens as shown in Figures 4.17 and 4.18. The position of the inclusions at the bottom of the dimples in these figures indicate that void initiation occurred at the inclusion matrix interface. The direction of loading as well as inclusion orientation have also been shown to influence void initiation [32], however, this trend was not analyzed in this study since the

inclusions in all the metal groups were primarily spherical as shown in Figures 4.3(a to f). Because of the tendency of voids to initiate at inclusions, a method of reducing the size and distribution of nonmetallic inclusions would improve the fracture toughness of a material. The results of inclusion control by alloy additions in the six metal groups tested, and the resulting increases in fracture toughness will be discussed in section 5.2.3.

5.1.3 The Effect of Stress Conditions on the Fracture Process

5.1.3.1 Uniaxial Stress Conditions

Uniaxial stress conditions were obtained, at least to the point of tensile instability, during the fracture of the tensile specimens. The analysis of the fracture surface features with SEM enabled conclusions to be made regarding the sites for void nucleation, the degree of void growth prior to coalescence and the localized stress conditions during fracture. Figures 4.13(a to f) illustrate the uniform fracture surface topography found on the tensile surfaces in all the metal groups. The dimples are of uniform size and circular shape. Also, the fracture surface appears flat, indicating that void initiation occurred on a single plane normal to the loading axis. The circular appearance of the voids verifies that uniaxial stress conditions did in fact exist, at least during void nucleation [76]. Figures 4.14(a to f) give a statistical indication of the void size

distribution calculated from numerous micrographs of each metal group. These graphs indicated that the majority of voids are approximately 1.5μm or less in size in all the metal groups. This suggests that the majority of voids nucleate at sites spaced less than 1.5μm apart.

The resolution of the SEM image at such high magnification of such irregular topography is a limiting factor when studying the mechanism of void initiation and growth during tensile deformation. The micrographs, however, illustrate that the voids are separated by very thin walls of material indicating that void growth and coalescence occurs by the excessive localized plastic deformation (rupture) of the material ligament separating two voids. Final separation occurs by the complete rupture of the remaining ligament and results in the thin, dimple free walls separating the larger dimples.

The reason that the voids on the fracture surfaces subjected to uniaxial stress conditions seem to nucleate regularly at sites spaced approximately 1.5μm apart is not clear. Microstructural features located at spacings of approximately 1.5μm intervals within this particular material are grain boundary triple points which have been attributed to void initiation sites in pure HCP titanium [29] but not in dual phase BCC steels. Also small precipitates present in all the metal groups, as shown in Figure 4.20(a to f) could act as void nucleation sites when subject to the ap-

propriate local stress conditions as has been suggested in the literature [36,39].

5.1.3.2 Triaxial Stress Conditions

The characteristic fracture surfaces resulting from void nucleation and growth during triaxial stress conditions is shown in the low magnification fractographs of precracked three point bend specimens, Figure 4.15(a to f) , of each metal group. The irregular void pattern suggests that void nucleation does not occur on a single plane but the fracture followed an irregular path. Unlike the tensile fracture surfaces, which contain primarily circular voids, the fracture surfaces resulting from triaxial stress conditions has highly elongated dimples. This suggests a diversity of localized opening modes and resulting stress states [76].

The most obvious difference between the uniaxial and the triaxial fracture surfaces are the difference in void size between the two. The triaxial stress conditions result in much larger voids than the uniaxial stress conditions. An indication of the statistical distribution of void sizes is illustrated in Figure 4.16(a to f). As is shown in these graphs, most voids are in the order of 15μm in diameter. It has been suggested in the literature [77] and the results of this study also confirm that the reason for the difference in topography between tensile and notched specimens is that void growth is strongly dependent on the local stress condi-

tions. In uniaxial tensile specimens the voids grow parallel to the tensile axis and expand laterally only after transverse stresses have been generated by necking. The triaxial stress state present in the notched specimen allows the voids to expand laterally throughout the growth process, this results in the large elongated dimples that are observed.

From this study it is apparent that the process of ductile fracture occurring, by void nucleation and growth, within a given material can be vastly different depending upon the local stress conditions present. As a result, the evaluation of fracture toughness must take into account the stress conditions present during testing. The results from this study indicate that extrapolation of fracture toughness parameters obtained from uniaxial fracture tests to predict the fracture toughness of the same material under triaxial stress conditions or vice versa may lead to erroneous results. This is confirmed by the fact that metals which have a very high tensile strength show a correspondingly low fracture toughness.

5.2 THE EFFECTS OF ALLOY ELEMENTS ON THE FRACTURE OF HSLA STEELS

Section 5.1 discussed, qualitatively, the process of ductile fracture in HSLA steels in terms of changes in material conditions at a microstructural level. The fracture process

in these multiphase commercial quality structural steels was shown to be dependent upon the effect of alloy contents for precipitation strengthening, grain refinement, and inclusion size control. The following section discusses variations in ductile fracture toughness with varying alloy additions and resulting microstructural changes. This will further lead to a quantitative correlation between the macroscopic parameter, J_{IC} , and the metallurgical factors that affect the toughness of these steels.

5.2.1 The Macroscopic Fracture Toughness of HSLA Steel

The excellent fracture toughness properties of precracked bend specimens from these HSLA steels is displayed by the high J_{IC} values ranging from 83.0 KJ/M^2 to 159.7 KJ/M^2. The fracture toughness of these steels is, therefore , superior to the toughness of annealed AISI 4340 (J_{IC} =40KJ/M^2) and comparable to slightly cold rolled (2% deformation) AISI 4340 low alloy steel which displayed a J_{IC} value of 160 KJ/M^2 [80]. J_{IC} results reported from fracture tests on AISI 310 austenitic stainless steel (J_{IC} = 80 KJ/M^2) [74] and Al-Mg-Si alloys (J_{IC} = 11.2 to 30.2 KJ/M^2) [41] indicate the excellent ductile toughness of the HSLA steels compared to other metallic materials.

5.2.2 Improved Fracture Toughness by Grain Refinement

Figure 4.2 indicates significant grain refinement in metals 3 to 6 compared to metals 1 and 2. A feature common to metal in groups 3 to 6 is that they contain Ti or Nb alloy additions alone or in combinations with each other (Table 3.1). Metal 2 containes V additions and displays no grain refinement compared to the base metal. The reason attributed to the improved grain refinement properties of Nb and Ti compared to V is that Nb and Ti are less soluble in solid solution at high temperatures than is V [43-46]. The result is that with heating and controlled rolling, Nb and Ti will precipitate in the form of Nb(C,N) and Ti(C,N) precipitates and pin the grain substructure to slow the recrystallization and growth of austenite grains. Upon cooling, this structure results in smaller grain sizes. Vanadium is more soluble at high temperature and therefore does not precipitate during austenite recrystallization in this steel composition [78,79]. The result is that recrystallization and grain growth occurs to a greater extent and larger ferrite grains are thus produced upon cooling.

A positive feature of grain refinement as a strengthening method is that it increases the yield stress and fracture strength simultaneously. Figure 4.10 supports this trend by showing an increase in fracture toughness with decreasing grain size. Empirical equations relating variations of yield stress, σ_y, and ductile brittle transition tempera-

ture, T_c, with grain diameter,2d, have been suggested by Hall [3] and Petch [4] and are reviewed in sections 2.3.1 and 2.4.2. The success of these equations in predicting the yield stress and impact transition temperatures in ferritic steels suggests that the contribution of grain size refinement to the tensile and fracture properties of a material is probably related to the increased resistance to dislocation movement produced by more grain boundaries. The accumulation of dislocations along grain boundaries of highly strained TEM foils, as illustrated in Figures 4.21(a to e) and discussed in section 5.1.1.1, supports this conclusion. In terms of ductile fracture, The trend shown in Figure 4.10 could be represented by a linear J_{Ic} vs $d^{-1/2}$ plot as in Figure 5.1 The linear relationship in Figure 5.1 suggests that an equation similar to equation 2.11 could be developed to predict J_{Ic} namely

$$J_{1C} = J_0 + Dd^{-1/2} \qquad (5.2)$$

where J_o is a material constant relating to the energy required to move a dislocation through a free lattice. D is a material constant relating to the effectiveness of the grain boundaries in locking the dislocations.

Equation 5.2 can be related to the deformation process in these HSLA steels by comparing the individual terms with the stages of deformation in Figure 4.23. In equation 5.2 the term $Dd^{-1/2}$ represents the energy absorbed by the material due

to the interaction of dislocations with grain boundaries. This term could be related to the the deformation process in stage I where plastic deformation occurs without transgranular dislocation movement. In equation 5.2 the term J_o can describe the smaller amount of energy absorbed in the material during stage II deformation when dislocation structure development is no longer impeded by grain boundaries. A schematic description summarizing the influence of the individual terms in equation 5.2 on the process of plastic deformation is shown in Figure 5.2

It is important to keep in mind,however, that unlike tensile parameters J_{ic} represents an event which is a simultaneous result of numerous factors, only one of which is the interaction of dislocations with grain boundaries. As a result, further investigations are required to establish the validity of equation 5.2 over a range of grain sizes for a given steel.

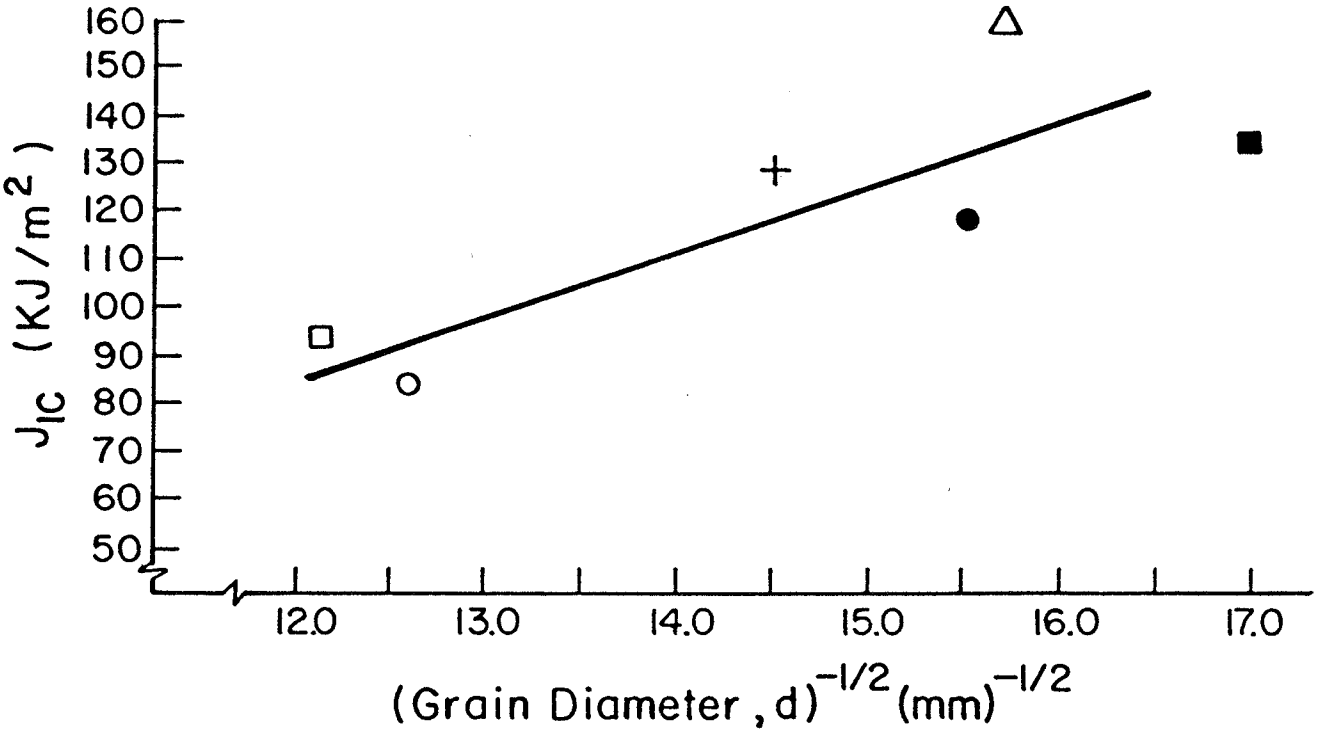

Figure 5.1: A Linear J_{Ic} Versus $d^{-1/2}$ Plot for the HSLA Steel

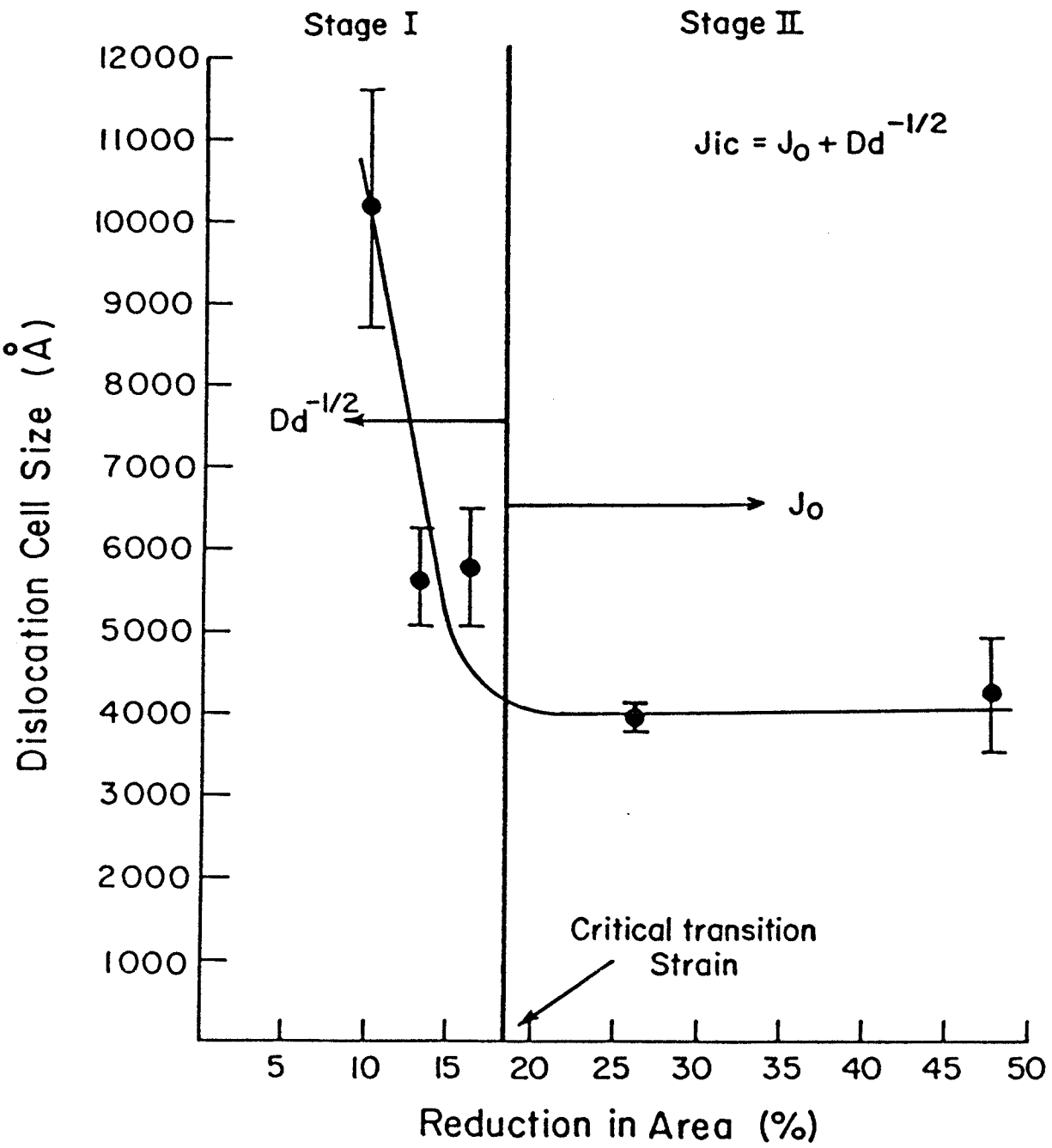

Figure 5.2: The Relationship Between Fracture Toughness, J_{IC}, and the Stages of Plastic Deformation

5.2.3 Improved Fracture Toughness by Inclusion Control

The relationships between nonmetallic inclusion diameter as well as inclusion volume fraction to fracture toughness are shown in Figures 4.11 and 4.12 respectively. It is apparent that an increase in the size and/or the volume fraction of inclusions will significantly decrease the fracture toughness. The role of nonmetallic inclusions as sites for void nucleation in the process of ductile fracture has been discussed in section 5.1.2.2 as well as in the literature [34,36,37,80]. Since J_{IC} is related to the applied energy required for the large scale growth and coalescence of voids ahead of a crack, it follows that this fracture toughness parameter would be very sensitive to factors affecting the ease of void initiation. This is supported by the fact that metals 1 and 2, each containing the highest volume fraction of inclusions and the largest mean inclusion diameters had the lowest fracture toughness (Figure 4.9)

The highest values of J_{IC} were obtained for metal groups 3 and 6. The effect of inclusion volume fraction on the fracture toughness of metal groups 3 and 6 will next be examined. Figure 4.5 indicates that metal group 3 has the lowest volume fraction of inclusions which suggests that the titanium acts as nucleation sites for smaller and more evenly dispersed sulfides which are too small to be detected by the image analyzer. This is supported by the semi-quantitative x-ray energy spectrum of Figure 4.19(c) where a high

concentration of titanium was detected in the inclusion compared to the surrounding matrix composition. The effect of niobium on the inclusion size is less clear. However, the trend in reducing both the inclusion size and volume fraction with additions of niobium remains similar to that of titanium and results in the significant increase in observed fracture toughness for metal group 6.

5.2.4 Improvements in Fracture Toughness by Alloy Additions

The results of this investigation have considered the effect of three microstructural factors on the fracture toughness parameter J_{IC} for HSLA steel. These factors are namely the grain size, the inclusion volume fraction, and the average inclusion diameter present. A possible representation of the combined effect of these factors on J_{IC} is shown in Figure 5.3 which shows J_{IC} as a function of the log[grain size x inclusion diameter x volume fraction of inclusions (%)]. This relationship is found to result in a straight line when all the points, each corresponding to one metal group, are used in Figure 5.3. While a quantitative analysis of this linear relationship appears rather complex and is beyond the scope of this discussion, Figure 4.6c shows the dependence of the macroscopic toughness parameter, J_{IC} , with microstructural factors. Figure 5.3 illustrates the complexity of the mechanism occurring at the crack tip as blunting followed by stable crack growth takes place. The

effectiveness of alloy additions to control the microstructural factors is also shown in Figure 5.3 As a result, the dual effectiveness of Nb and Ti alloy additions in grain refinement and inclusion size reduction compared to V results in an increase in J_{IC} from 83.0 KJ/M^2 for the base metal (metal 1) and 92.8 KJ/M^2 for the V alloy (metal 2) to 159.7 KJ/M^2 and and 132.1 KJ/M^2 for the Ti and Nb alloy respectively.

It is worth noting that for metal groups 4 and 5 which contain combinations of Nb, Ti, and V, intermediate values of fracture toughness, J_{IC} , and microstructural factors (grain size, inclusion size, and inclusion volume fraction) are observed. The combined effect of more than one alloying addition on these properties is not clear. However, in one instance, it was reported that addition of molybdenum to an HSLA steel already microalloyed with niobium resulted in a decrease in fracture toughness [42]. Further studies on this problem of microalloying with more than one alloying element are necessary before general conclusions can be made.

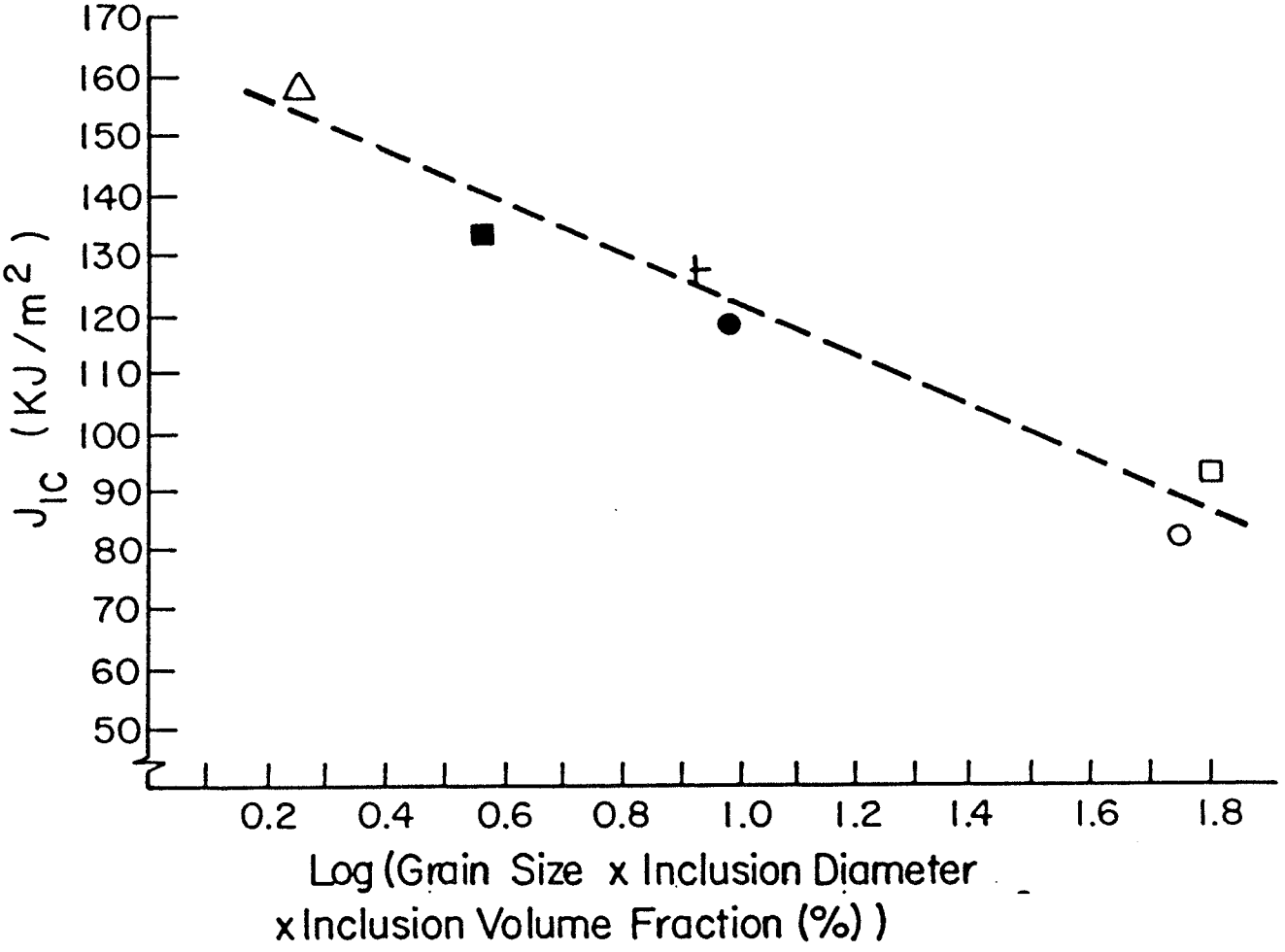

Figure 5.3: J_{IC} Versus Log[Grain Size x Mean Inclusion Diameter x Inclusion Volume Fraction (%)]

Chapter VI

CONCLUSIONS

The process of ductile fracture in HSLA steel has been studied from a macroscopic as well as a microscopic viewpoint.

Macroscopic fracture tests indicate that the ductile fracture toughness, expressed in terms of J_{IC}, was dependent upon material grain size as well as inclusion size and density. J_{IC} was found to increase with a decrease in mean inclusion diameter and/or volume fraction. J_{IC} was also found to increase with decreasing grain diameter, d, for these HSLA steels according to the equation:

$$J_{IC} = J_o + Dd^{-1/2} \qquad (5.2)$$

where J_o and D are material constants. A linear relation between J_{IC} and log[Grain Size x Mean Inclusion Diameter x Inclusion Volume Fraction (%)] for the HSLA steel tested supports the conclusion that the macroscopic fracture toughness is controlled by several microstructural variables simultaneously.

The microstructural analysis of these HSLA steels before and after fracture provided a more complete understanding of the influence of grain size and inclusions on the macroscopic fracture toughness.

The SEM analysis of the fracture surfaces of tensile and precracked three point bend specimens showed inclusions situated at the bottom of voids. This supports the theory that nonmetallic inclusions lower the fracture toughness in a metal by acting as sites for preferential void initiation.

A study of the microstructural changes occurring during tensile straining, using TEM, indicated that the plastic deformation process can be divided into two distinct stages (I and II) in this HSLA steel. Stage I of the deformation process is characterized by the development of dislocation structures, or cells, throughout the material matrix. During stage I these dislocation structures branch out and interconnect with increasing strain. The result is that the dislocation structure size decreases with increasing strain. It was found that after a critical strain had been reached (corresponding to a local reduction in area of 17% for this HSLA steel) the dislocation size no longer decreased with increases in local strain. This represented the onset of stage II of the deformation process. A characteristic feature of stage II is that the extension of dislocation structures across grain boundaries was observed on a large scale. It was concluded that the strength of grain boundaries in impeding dislocation motion controls the transition from stage I to stage II of the deformation. The terms in equation 5.2 were explained with respect to the observations made about the actual deformation process. It was suggested

that the term $D\bar{d}\dot{\bar{\epsilon}}$ in equation 5.2 corresponds to the energy absorbed by the material during stage I of the deformation process. J_0 corresponds to the smaller amount of energy absorbed by the material in stage II of deformation.

The objectives of this study were achieved by studying the relationships between macroscopic fracture toughness, J_{Ic}, grain size and inclusion distribution. These results were then compared with the effects of grain size and inclusions on the plastic deformation process at a microstructural level. The final result was a description of ductile fracture in ferritic HSLA steel in terms of its fundamental constituent, the process of plastic deformation.

REFERENCES

1. F.B.Pickering, "Physical Metallurgy and the Design of Steels", Applied Science Publishers, London, p 61 (1978)

2. W. Barr and A.J.K. Honeyman, J. Iron Steel Inst., v 157, p 239 (1947)

3. E.O. Hall, Proc. Phys. Soc. B, v 64, p 747 (1951)

4. N.J. Petch, J. Iron Steel Inst., v 25, p 1744 (1953)

5. J.R.C. Guimarnaes, K.K. Chawla, P.R. Rios, and J.M. Rigsbee, Metals Technology, v 11, p 1 (Jan. 1984)

6. W.B. Morrison, J. Iron and Steel, p 317 (April 1963)

7. E.R. Morgan et al, J. Metals, p 829 (Aug. 1965)

8. R. Phillips and J.A. Chapman, J. Iron and Steel Inst., v 204, p 615 (1966)

9. ASTM Standards,"Designation E812", The American Society for Testing and Materials, (1981)

10. A.H. Cottrell, Iron Steel Inst. Spec. Rep. No. 69, p 281 (1961)

11. A.A. Wells, "Unstable Crack Propagation in Metals: Cleavage and Fast Fracture Symp. Crack Propagation", College of Aeronautics, Cranfield, B4 (1961)

12. R.F. Smith and J.K. Knott, in Conf. Practical Applications of Fracture Mechanics to Pressure Vessel Technology, Inst. of Mechanical Engineers, p 217 (1971)

13. J.F. Knott, "Fundamentals of Fracture Mechanics", Halsted Press, New York, p 163 (1973)

14. J.R. Rice, J. App. Mech. , v 35, p 379 (1968)

15. J.A. Begley and J.D. Landes, "The J-Integral as a Fracture Criterion, in Fracture Toughness", ASTM STP 514, p 1 (1972)

16. J.R. Rice, P.C. Paris, and J.G. Merkle, "Some Further Results of J-Integral Analysis and Estimates, Progress in Flaw Growth and Fracture Toughness Testing", ASTM STP 536, p 231 (1973)

17. J.D. Landes and J.A. Begley, "Test Results From J-Integral Studies: An Attempt to Establish a J_{Ic} Testing Procedure, in Fracture Analysis", ASTM STP 560, p 170 (1974)

18. "Standard Test for J_{Ic} , A Measure of Fracture Toughness: Designation E813-81", American Society for Testing and Materials Annual Book of Standards, part 10, p 810 (1981)

19. G.A. Clarke, W.R. Andrews, P.C. Paris, and D.W. Schmidt, "Single Specimen Tests for J Determination", in Mechanics of Crack Growth, ASTM STP 590, p 27 (1976)

20. "Standard Method of Test for Elastic-Plastic Toughness, J_{Ic} ", JSME Standard, S001-1981

21. P. Nguyen-Duy and S. Bayard, J. Eng. Mater. Technol., v 103, p 55 (1981)

22. J.D. Hayes and C.E. Turner, Int. J. Fract., v 10, p 17 (1974)

23. M.G. Dawes, "Elastic-Plastic Fracture Toughness Based on the COD and J-Contour Integral Concepts, in Elastic-Plastic Fracture", ASTM STP 668, p 307 (1979)

24. K.F. Amouzouvi and M.N. Bassim, Materials Science and Engineering, v 55, p 257 (1982)

25. M.R. Bayoumi and M.N. Bassim, "Stretch Zone Ductility and Toughness Studies in the Transition Region of 1045 Steel", Proc. Int. Conf. of Materials, ICM 4, Stockholm, Sweden, v 2, p 803 (1983)

26. W.S. Owen, D.H. Whitmore, M. Cohen, and B.L. Averbach, Weld J., v 36, p 503s (1957)

27. J. Intrater and E.S. Machlin, Acta Metall., v 7, p 140 (1959)

28. R.C. Gifkins, Acta Metall., v 4, p 98 (1956)

29. M.A. Erickson, "The Ductile Fracture of C.P. Titanium", M.Sc. Thesis, University of Virginia, Charlottesville, Va. (1983)

30. H.C. Chang and N.J. Grant, J. Met., AIME, v 206, p 545 (1956)

31. I. Kozaso and J. Tanaka in J.J. deBarbadillo and E. Snape (eds.), "Sulfide Inclusions in Steel", Proc. Int. Symp., ASM, (1974)

32. W.A. Spitzig, Metall. Trans. A., v 14a, p 471 (March 1983)

33. A.A. Willoughby, P.L. Pratt, and T.J. Baker, "Advances in Fracture Research", International Conference on Fracture (ICF5), v 1, p 179 (1981)

34. A.S. Argon, J. Im, and R. Safoglu, Metall. Trans. A., v 6a, p 825 (1975)

35. J. Gurland and J. Plateau, Trans. ASM, v 56, p 442 (1963)

36. S.H. Goods and L.M. Brown, Acta Metall., v 27, p 1 (1979)

37. J.R. Fisher and J. Gurland, Met. Sci., v 15, p 193 (1981)

38. H.G.F. Wilsdorf, Materials Science and Engineering, v 59, p 1 (1983)

39. J.F. Knott, in "Effect of Second-Phase Particles on the Mechanical Properties of Steel", Proc. of the Iron and Steel Inst., 1971

40. J.R. Rice and M.A. Johnson, in "Inelastic Behaviour of Solids", M.F. Kanninen et al, eds., McGraw-Hill, New York, p 641 (1970)

41. J.A. Blind and J.W. Martin, Materials Science and Engineering, v 57, p 49 (1983)

42. M.N. Bassim, J.M. Dorlot, and A. Penelon, Canadian Metall. Quarterly, v 19, p 177 (1980)

43. J.N. Cordea and R.E. Hook, Metall. Trans. A., v 1, p 111 (Jan. 1970)

44. L.J. Cuddy, Metall. Trans. A., v 15a, p 87 (Jan. 1984)

45. M.G. Akben, T. Chandra, P. Plassiard, and J.J. Jonas, Acta Metall., v 32, p 591 (1984)

46. S.S. Hansen, J.B. Vander Sande, and M. Cohen, Metall. Trans. A., v 11a, p 387 (March 1980)

47. D. Kuhlmann-Wilsdorf, R. Maddin, and H.G.F. Wilsdorf, in J.J. Harwood (ed.), "Strengthening Mechanisms in Solids", ASM, Metals Park, OH, p 137 (1962)

48. G. Thomas, "Transmission Electron Microscopy in Metals", Wiley, New York, p 201 (1962)

49. P.B. Swann and A. Howie, from Ref. 50, p 202

50. A.S. Keh and S. Weissmann, "Electron Microscopy and Strength of Crystals", Interscience, New York, p 242 (1963)

51. W. Carrington, K. Hale, and D. McLean, Proc. Roy. Soc., v A259, p 203 (1960)

52. C.E. Feltner and C. Laird, Acta Metall., v 15, p 1633 (Oct. 1967)

53. L. Buchinger and S. Stanzil, Phil. Mag. A., v 50, p 275 (1984)

54. F.R.N. Nabarro, Z.S. Basinski and D.B. Holt, Adv. in Phys., v 13, p 193 (1963)

55. M.N. Bassim, "Dislocation Sub-boundaries, a Theoretical Study", Ph.D. Thesis, University of Virginia, (1973)

56. D. Kuhlmann-Wilsdorf and N.R. Comins, Mater. Sci. Eng., v 60, p 7 (1983)

57. D. Kuhlmann-Wilsdorf, "Work Hardening", Gordon and Breach, New York, p 97 (1968)

58. R.N. Gardner, T.C. Pollock, and H.G.F. Wilsdorf, Mat. Sci. and Engineering, v 29, p 169 (1977)

59. G. Langford and M. Cohen, Trans. ASM, v 62, p 623 (1969)

60. D. Kuhlmann-Wilsdorf, Metall. Trans. A., v 1, p 3173 (Nov 1970)

61. D. Griffiths and J.N. Riley, Acta Metall., v 14, p 755 (June 1966)

62. N.J. Petch, J. Iron Steel Inst., v 25, p 173 (1954)

63. J. Friedel, in B.L. Averbach et al (eds.), "Fracture", Wiley, New York, p 498 (1959)

64. A.S. Tetelman, in D.C. Drucker and J.J. Gilman (eds.), "Fracture of Solids", Wiley-Interscience, New York, p 461 (1963)

65. A.S. Tetelman and A.J. McEvily, "Fracture of Structural Materials", Wiley, New York, p 200 (1967)

66. J.R. Rice and R. Thomson, Phil. Mag., v 43, p 1103 (1981)

67. J. Weertman, Phil. Mag. A, v 43, p 1103 (1981)

68. K.F. Amouzouvi and M.N. Bassim, Materials Science and Engineering, v 62, p 137 (1984)

69. "Standard Methods of Tension Testing of Metallic Materials: Designation E8-82", ASTM Annual Book of Standards, Philadelphia (1983)

70. P. Albecht, W.R. Andrew, J.P. Gudas, J.A. Joyce, F.S. Loss, D.E. McCabe, D.W. Schmidt, and W.A. Slugs, "Tentative Test Procedure for Determining the Plane Strain J -R-Curve", Sixth Draft, Private Communication

71. D. Koesen and S. Kritzinger, Acta Metall., v 30, p 1219 (1982)

72. J.M. Chilton and M.J. Roberts, Metall. Trans. A., v 11A, p 1711 (1980)

73. R.L. Reuben and T.N. Baker, Metals Technology, v 11, p 6 (Jan. 1984)

74. K.F. Amouzouvi, "Effect of Prior Deformation on the Fracture Toughness in Metals", Ph.D. Dissertation, University of Manitoba, Winnipeg, Manitoba (1983)

75. Reference 1, p 20

76. C.D. Beachem, Met. Trans. A., v 6A, p 377 (1975)

77. J.F. Knott, in R.C. Gifkins (ed.), Sixth International Conference on the Strength of Metals and Alloys, Melbourne, Australia, v 2, p 799 (1982).

78. M.G. Akben, I. Weiss, and J.J. Jonas, Acta Metall., v 29, p111 (1981)

79. M.J. White and W.S. Owen, Metall. Trans. A., v 11A, p 597 (1980)

80. G. LeRoy, J.D. Embury, G. Edward, and M.F. Ashby, Acta Metall., v 29, p 1509 (1981)